THERMO-MECHANICAL INVESTIGATION OF DIE-LESS WIREDRAWING PROCESS

by

Hani Jafari

B.A., Eastern Mediterranean University, 2008

A THESIS SUBMITTED IN PARTIAL FULLFILMENT OF
THE REQUIREMENTS FOR THE DEGREE OF

MASTER OF APPLIED SCIENCE

in

The Faculty of Graduate Studies

(Mechanical Engineering)

THE UNIVERSITY OF BRITISH COLUMBIA

(Vancouver)

February 2013

ABSTRACT

Wiredrawing process as a bulk forming process is one of the oldest manufacturing processes known. The rigid "Die", which is the tool in the process, is responsible for the most of the cost of the process. In the "Die-less" wiredrawing, however, the die is replaced with a Heating-Cooling unit, which reduces the cost of the process significantly.

The die-less wiredrawing process as a thermo-mechanical process consists of mechanically loading the wire or a rod along its longitudinal axis, and locally heating it to lower its yield strength; and thus, less force needed to pull and stretch the wire. The wire is cooled subsequently in order to stabilize dimension and recover its strength.

In this study, the Mechanical Threshold Stress (MTS) model along with continuity equation and a heat transfer model are utilized to mathematically model the die-less wiredrawing process in the deformation zone. Numerical procedures are used to simulate the process in transient state and identify the main process parameters.

From the results of this study, it was shown that is possible to model the process through semi-discretization of Partial Differential Equations (PDE), which govern the dynamic of the process. It was also shown that the process is highly sensitive to temperature and that the most important parameter in controlling the process in transition from unsteady to steady state is the deformation zone length.

TABLE OF CONTENTS

LIST OF TABLES

LIST OF FIGURES

GLOSSARY

BC	Boundary Condition
BCC	Body Centered Cubic
BFD	Backward Finite Difference
CFD	Centered Finite Difference
CSA	Cross-Sectional Area
DLD	Die-less Drawing
FCC	Face Centered Cubic
FD	Finite Difference
FEA	Finite Element Analysis
FEM	Finite Element Method
FFD	Forward Finite Difference
HMC	Heating-Measuring-Cooling
IC	Initial Condition
MTR	Maximum Temperature Reached
MTS	Mechanical Threshold Stress
ODE	Ordinary Differential Equation
PDE	Partial Differential Equation
RA	Reduction in Area
SPF	Super Plastic Formation

ACKNOWLEDGEMENTS

This Research Paper is lovingly dedicated to my mother, Zahra Javidmoghaddam who is the source of greatness and love and to my father, Ali Jafari, who is my constant source of motivation and inspiration. Without their love and support this project would not have been possible.

CHAPTER 1

INTRODUCTION

1.1 Overview

Wiredrawing is the manufacturing process of making a wire, generally from a rod or a bar. Wires are used in multitude of products, from electricity transmission to suspension bridge support. The product is either used as formed or can be further processed into other shapes such as by bending or rolling.

Wires have been produced for decades by a variety of manual methods such as hammering, strip or block twisting of silver and gold wires, depending on the wire material, size and application. But, the need for larger production quantities, higher quality, and greater strength necessitated the development of mechanized and automated drawing processes.

The wiredrawing as a bulk forming process, which involves large plastic deformation is one of the oldest manufacturing processes known and the evidence of wiredrawing can be traced back to 1700 B.C [29]. The conventional technique to produce metal wires is cold drawing (See section 1.2), in which the wire diameter is reduced by pulling it through a conical aperture called "die" that has cemented carbide or diamond working surface. The wiredrawing die is an integral

and crucial component of the conventional drawing process. The drawability of the wire, and therefore, the drawing ratio decreases due to strain hardening in a multiple drawing process [38]. For a large reduction in the diameter of wire, a sequence of dies with decreasing hole diameters is typically used. Due to the frictional forces between the wire and the bearing surfaces of the die and the heating effect, considerable wear occurs at the tool workpiece interface during the forming operation and consequently the tool (die) life rapidly diminishes. Moreover, the use of fixed diameter dies results in dimensional inflexibility while the idea behind any metal forming process is to use simple tools, of which position and velocity can be controlled to yield a large variety of workpieces with different shapes and minimum expenditure of time and capital.

The earliest investigation of the possibility to eliminate the "die" from wiredrawing was the identification of hydrodynamic forces generated while drawing a wire within a specially constructed chamber [22]. The wiredrawing die was replaced with a reduction unit which consisted of two parallel stepped or tapered bores, as illustrated in Figure1.1, with the smaller bore diameter greater than the initial nominal wire diameter. However, the accuracy of the drawn diameter was dependent on the "effective die" formed inside the reduction unit.
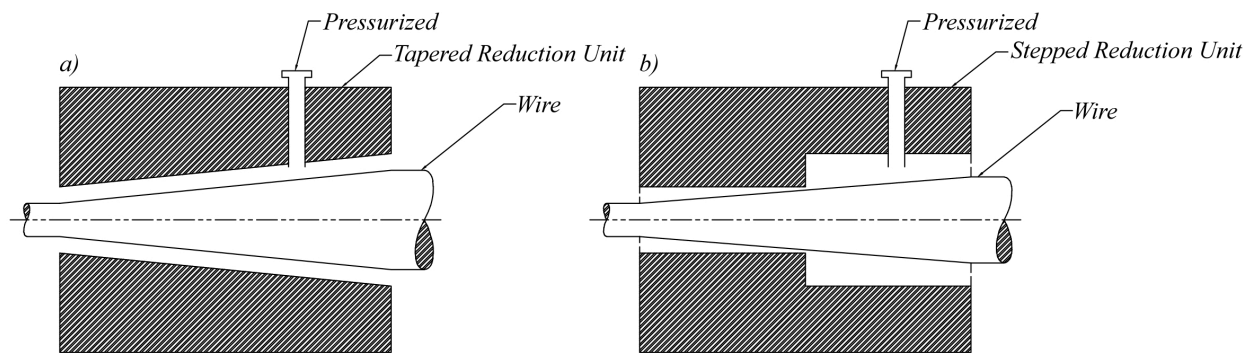
Figure 1.1: Reduction units a) Tapered and b) Stepped

1.2 A brief review of traditional bundle wiredrawing

In traditional bundle wiredrawing, a wire is manufactured by a drawing process, in which the reduction of the wire diameter is achieved by pulling the cylindrical ingot of metal through a rudimentary die, Figure 1.2. Dies must be hard and wear resistant; therefore, they are made of chilled iron, hardened alloy steel, cemented carbide and diamond. The harder materials last longer but cost more.
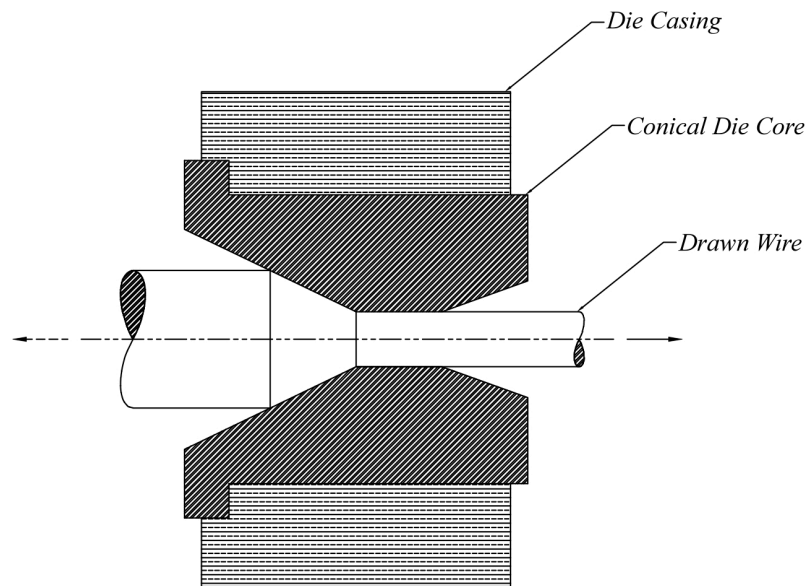
Figure 1.2: A Conical Die

The traditional wiredrawing process consists of pointing the rod, threading the pointed end through a die, and attaching the end to a cylindrical drawing block. An electric motor turns the block thus pulling out the lubricated rod through the die, reducing its diameter and increasing its length. Given constant material properties, the force needed to pull the wire through a cone-shaped die is directly related to the reduction in area, semi-die angle and the friction between the draw material and the die. As the value of these factors is increased the draw force increases. A limit is set in the drawing of the wire by the tensile failure of the drawn section. If there is no strain hardening this will occur at a stress equal to the yield stress of the material, otherwise the

wire fails at a higher "strain-hardened" value. A brief review of mathematical analysis of the wiredrawing with die can be found in Appendix A.

1.3 Super-plasticity phenomenon

For many years it has been known that unusual ductility can be obtained by mechanical deformation during a phase change or an allotropic transformation. This enhanced ductility associated with structural changes under applied stress is known as super-plasticity [49].

Studies of the torsional ductility of pure iron by Sherby et al. [41] and others [11] show that alpha iron possesses appreciably greater ductility than gamma iron, when the (extrapolated) values are compared at the same temperature.

This anomalous ductility phenomenon, which was discovered by Bochvar et al. [6] occurs under condition associated with a phase change or more generally with a temporary structural change involving breaking of atomic bonds in the crystalline lattice which results in a relative change in volume (e.g. the change in the lattice parameter).

After the publication of Underwood [49], of a detailed review of the early Russian work of Bochvor and Sviderskaya [6] in 1945 (relating to the phenomenon of super-plasticity), Backofen and his team [1] set about replicating some of the Russian work and established the importance of strain rate sensitivity to the extraordinary neck-free tensile elongation characteristic of superplastic metals, which gave birth to a novel method for drawing steel and titanium by heating and pulling. A brief review of strain-rate sensitivity index derivation is in Appendix B.

Backofen and his colleagues published their paper [1] in which they described the ''extraordinary formability'' exhibited when fine-grain zinc-aluminum eutectoid (Zn-22%Al) was subjected to bulge testing under appropriate conditions. It was for the first time that a superplastic ''bubble'' was pneumatically formed from a sheet of superplastic AlZn eutectoid

alloy [5]. This important moment signaled the emergence of a new technology: superplastic forming (SPF). They concluded their research findings with the following insightful comment ''even more appealing is the thought of applying superplastic metals forming techniques borrowed from polymer and glass processing.'' Since then their insightful thought has become a substantial reality with thousand tons of metallic materials now being super-plastically formed each year.

1.4 Die-less drawing process

This innovative method, namely die-less drawing (DLD), is a semi-hot or hot-forming manufacturing process of materials that have high strength and poor ductility and that are difficult to form and shape by the conventional wiredrawing methods with rigid dies. This contact-free process takes the advantage of the temperature dependency of the flow stress to reduce the cross-sectional area of the wire.

In the die-less wiredrawing, one form of die-less drawing process, the wire enters a Heating-Measurement-Cooling unit (HMC) instead of the drawing die, where the transformation takes place. At the beginning of the deformation zone, by heating the wire, the yield stress decreases locally, so that, due to external forces caused by the difference in the velocity of the material flow, the necessary conditions for plastic flow can be achieved. The workpiece is drawn at a speed of v_1 through the heating-cooling unit, while the non-deformed part is moved at a speed of v_0, which is less than v_1 as illustrated in Figure 1.3. By subsequent forced convection in the cooling unit the yield stress again increases so that further deformation is halted.
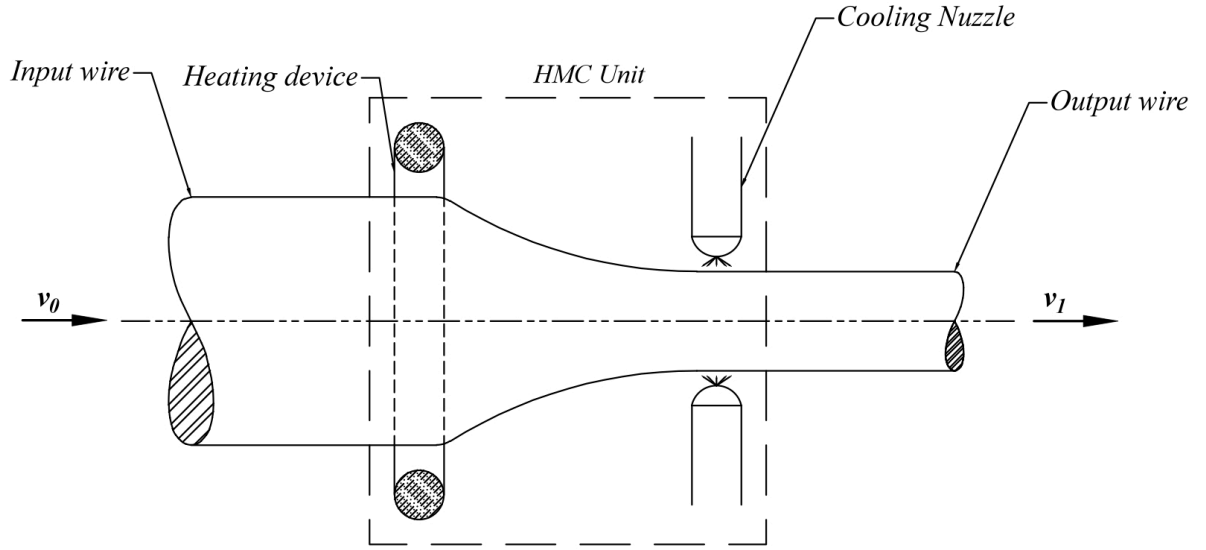
Figure 1.3: Schematic of the die-less wiredrawing

The reduction in cross-sectional area (*RA*) of wire can be expressed as:

$$RA = \frac{A_{in} - A_{out}}{A_{in}} = 1 - \frac{A_{out}}{A_{in}} \tag{1.1}$$

where A_{in} and A_{out} are representing the raw (input) and manufactured (output) material's cross-sectional area, respectively.

The die-less drawing "appears" to be a useful industrial technique, as its associated local deformation and stability can be controlled, by adjusting the velocities at the entry and exit of the deformation zone, and the heating-cooling rate. On the other hand, however, it is important to also realize that any small variation in the process parameters, e.g. temperature, drawing force and speed can adversely influence the dimensional quality and stability of the final product, and in some cases, may result in breakages.

Researchers cite the following advantages and incentives for the die-less drawing [26, 55]:

1. The absence of die makes the process less expensive as compared to conventional processes.

2. The process is suitable for a material that has a high strength and/or a high frictional resistance.

3. A large reduction of area can be achieved in a single pass.

4. The feasible reduction of area is effectively achieves through the control of drawing velocities and the rate of heat transfer.

5. The process can be applied to produce discrete tapered bars or varied cross section bars.

6. Since a thermo-mechanical cycle is applied and produces plastic deformation, grain refinement (in case of steel) or any other microstructural transformation may be coupled to area reduction, in order to give better properties to the final product.

The main objectives of this study can be summarized as follows:

➢ To conduct a coupled thermo-mechanical analysis of the "Die-less wiredrawing" process.

➢ To model the process in the deformation zone mathematically.

➢ To simulate the mathematical model numerically.

➢ To identify the main process parameters.

In the following, the literature is reviewed briefly in Chapter 2. The modeling of the die-less drawing process is presented in Chapter 3 and the numerical simulation of the process is studied in Chapter 4. The results are discussed in Chapter 5 and conclusions are gathered in Chapter 6.

CHAPTER 2

LITRATURE REVIEW

2.1 Early stage

Die-less drawing process emerged in 1969 when Weiss and Kot [52] utilized the superplastic transformation characteristics of metals in a deformation process. It was reported previously by the same authors [53] that a considerable increase in ductility with a concurrent drop in flow stress had been noted in certain metals and alloys when deformed during a phase transformation. Specifically, a material undergoing deformation under constant load, during a phase transformation, exhibits a large increase in creep rate at loads much below the normal yield strength of the material. This phenomenon, referred to as transformation plasticity, leads to an abnormally large neck-free elongation in metals. However, as Backofen et al. discussed [1], to prevent neck formation, a strain-induced hardening is required to offset the geometrical weakening caused by the reduction in cross section. In the broadest terms, the hardening to counteract necking might have its origin in such a development as metallurgical cold work, a drop in temperature, a rise in surface energy, or an increase in strain rate.

Weiss et al. [52] investigated the die-less wiredrawing process experimentally by modifying a lathe so that the spindle speed gives a draw velocity, v_1 in Figure 2.1, by means of a threaded rod. An assembly holding a heating coil, a cooling coil and stainless steel covered chromel-alumel thermocouple was mounted on the carriage of the lathe and was travelling with v_0 in the opposite direction. They conducted the experiment on cylindrical specimen of AISI 1018 steel, commercially pure titanium, and Ti-6Al-4V titanium alloy.
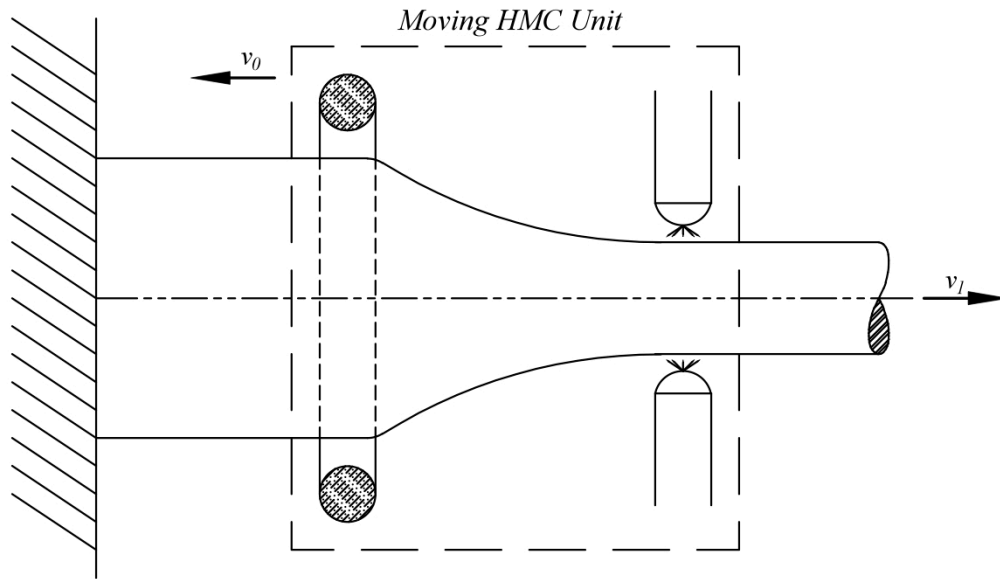
Figure 2.1: First experimental setup used by Weiss and Kot

From a practical as well as an analytical point of view it is desirable to obtain exact information on the temperature profile during the drawing process. However, a thermal lag in the temperature measurement with the thermocouple used in the experiments had prevented the measurement of the temperature profile across the deformation zone. Furthermore, since the specimen temperature during drawing did not reach the preset temperature as it was measured in the stationary setup, tests were run at slowest draw speed.

Weiss et al. [52] concluded that a considerable reduction in drawing force would result if the drawing velocities and the temperature profile permit the timely occurrence of transformation

plasticity. It is characterized by large neck-free elongation, a linear relationship between applied stress and strain, a relative insensitivity to grain size, and occurrence of plastic flow during a phase transformation even under external forces much smaller than that required for normal yield or flow in the material. They also pointed out that for the occurrence of transformation plasticity a critical strain rate range is necessary.

In 1977, Kobatake et al. [26] used the Finite Element Method (FEM) to calculate the variation of temperature in the material in both longitudinal and radial directions. Also, by constructing a continuous die-less drawing machine, Kobatake et al. investigated the effect of drawing velocity on maximum temperature, cooling rate and the heat supplied experimentally. They examined their results from FEM analysis, which were in good agreement with the experimental ones and concluded that there are little differences in the maximum temperature reached among the different drawing velocities, but the position of the peak values tends to shift from the entrance towards the exit of cooling apparatus with the increase of the drawing velocity. Moreover, they concluded that the cooling rate decreases remarkably with the increase of the drawing velocity.

Sekiguchi and kabotake [39] believed that the continuous drawing process could be carried out without a die if the development of necking could be properly controlled by strengthening of the deformed material. In other words, to cause necking, the wire should be locally heated and in order to stop further deformation, the necked part must be cooled. If the heating and cooling systems work well the system should be stable. Furthermore, the working limit of die-less wiredrawing is set by the fracture of the wire, which occurs in the deformation zone when the drawing force just exceeds the flow stress of the wire:

$$\sigma_{in} A_{in} < \sigma_{out} A_{out} \tag{2.1}$$

where σ and A are the flow stress and the cross sectional area, respectively, and indices *in* and *out* denote the entrance and the exit.

Sekiguchi et al. [39] developed a finite element model for heat transfer and used it to predict the temperature distribution in the material during the process. The fundamental differential equation used in the model includes the heat conduction, the heat input and the heat convection by material flow and coolant material.

From the results of a decoupled thermo-mechanical analysis, Sekiguchi et al. showed that at a low drawing velocity of 20 cm/min the difference between the surface temperature and the temperature at the center is about 20° C at the most. However, at a higher velocity of 95 cm/min, the temperature gradient in the radial direction in the deformed region became larger as the cooling rate was limited by heat conduction only. Hence, the experiment at the drawing velocity of 100 cm/min could not been successfully accomplished.

2.2 Advanced approach

To investigate the die-less drawing process, both thermal and mechanical properties of the materials are involved with a high interdependency among each other, which makes the investigation challenging. Scholars, however, took different approaches to analyze and model the process. The thermo-mechanical investigation can be separated into three main focuses:

1. Temperature distribution and heat transfer

2. Deformation and deformation-rate

3. Stability and feasibility of the process

However, the deformation and the thermal considerations have been handled separately, except for few researchers who studied and modeled a coupled thermo-mechanical system. On the other hand, many other academics investigated the process with a decoupled thermal and/or mechanical analysis. In the following subsections some of these studies reviewed.

11

2.2.1 Temperature and heat transfer

The investigation of the main process parameters and their interdependence is the prerequisite for the deliberate choice of input parameters to get the desired quality of the output. Among three main process parameters, i.e. drawing force, drawing velocity and temperature, only the temperature can be influenced locally whereas the force and velocity can be adjusted only globally, and therefore, temperature is the main control parameter [37]. Nevertheless, the temperature cannot be chosen arbitrarily. It results from the interaction of several modes of heat transfer like conduction, convection and radiation. Thus the intrinsic control parameter is not temperature itself, but the boundary condition determining the temperature distribution.

Pawelski et al. [37] simplified the general heat conduction equation in a cylindrical coordinate system by assuming axial symmetry; constant material properties, i.e. mass density ρ, thermal conductivity k and specific heat c; stationary temperature distribution in relation to the inductor; and constant heat power in order to transform the partial differential equation into two ordinary differential equations. By assuming an exponential distribution in x-direction and a Bessel distribution in r-direction the complete solution for the temperature distribution suggested by Pawelski is:

$$T_j(x,r) = \exp\left(\frac{V_H}{2\lambda}x\right)\sum_{i=0}^{n}J_0(\beta_{ji}r)\left\{G_{ji}\exp\left(x\sqrt{\frac{V_H^2}{4\lambda^2}+\beta_{ji}^2}\right)+H_{ji}\exp\left(-x\sqrt{\frac{V_H^2}{4\lambda^2}+\beta_{ji}^2}\right)\right\} \quad (2.2)$$

where x and r represent coordinates along longitudinal and radial direction respectively, λ is the thermal diffusivity ($\lambda = \dfrac{k}{\rho c}$), V_H is the velocity of the heating unit (inductor in this case) and J_0 is the Bessel function of first kind and zero order; the unknown eigenvalues β and the constants G and H can be determined from the boundary conditions of the integration zone. Index j is the number of the integration zone under consideration and n is the number of integration points used in the solution at the boundaries.

This complex analytical model (See section 3.3.1) can be effectively used to study the qualitative influence of the input parameters (like material, geometric and kinematic parameters), however, its use is restricted to steady state conditions and that the effect of plastic deformation should be neglected.

Although the deformation temperature arises as a function of different modes of heat transfer, i.e. radiation, convection and conduction, Naughton et al. [35] considered only the dominant conduction mode of heat transfer in their analysis. They set up a system of two differential equations for heat conduction in longitudinal and radial direction that could be solved simultaneously for temperature profiles. By employing induction heating, Naughton and Tiernan stated that the best method of obtaining even heating with the highest temperature occurring at the point of exit is to apply a gradual even taper heating along the longitudinal axis of the induction coil.

Yonggang et al. [30] studied the feasibility of die-less drawing process using laser as a heat source. In laser wiredrawing, a laser beam is used to heat the precursor wire to a critical temperature range corresponding to its plastic state, which is generally above the recrystallization temperature of the wire. This process is generally good for small diameter wire (ultra fine wires of diameter in order of 100 μm) due to the high precision heating capability of lasers; the temperature of wire can be maintained at a desired level to achieve maximum ductility accordingly. Furthermore, since the induction or resistance heating process is difficult to control for fine wires, and much of the heat energy is lost to the surroundings, laser Drawing can be utilized with the minimal energy loss. Another advantage of using laser technology is that it allows in situ oxidation protection, which is critical for very fine wires.

2.2.2 Deformation and deformation-rate

According to Naughton et al. [33] the prerequisites for a successful superplastic deformation include:

- Low strain-rate in the order of 10^{-5} to 10^{-3} s^{-1}.

- Working temperature of greater than half of melting temperature of the material.

- A small but stable grain size.

Tiernan and Hillery [47] carried out a Finite Element Analysis (FEA) of the die-less wiredrawing. Similar to Sekiguchi's work [39], Tiernan neglected the direction of principle stresses and assumed a stable condition for die-less drawing when the drawing stress is not greater than flow stress of the wire (Equation 2.1).

In order to predict the theoretical stress within the deformation zone during the die-less drawing process, Tiernan used the general Zener-Hollomon [56] stress relation given as:

$$\sigma = f(Z) = f(\dot{\varepsilon}e^{\Delta H/RT})\tag{2.3}$$

where Z is the Zener-Hollomon parameter; ΔH is an activation energy; R is the universal gas constant and T denotes the temperature. As Zener and Hollomon suggested, the isothermal stress-strain relation $\sigma(\varepsilon)$ in steels depends upon strain rate $\dot{\varepsilon}$ and temperature T, only through a single parameter and the parameter has the form:

$$Z = \dot{\varepsilon}e^{\Delta H/RT}\tag{2.4}$$

This relation was based upon the consideration that the mechanical properties must depend only upon a dimensionless quantity, and therefore, upon the ratio of strain rate and some rate characteristics of the material itself.

Roger Wright and Evan Wright [55] provided a practical mathematical framework, which includes the basic theory and a practical modeling of die-less drawing. The principal objective of

Wrights modeling was to calculate the parameter L_D, the deformation zone length. Assuming a constant strain rate, Equation 2.5, which is frequently used in simplified characterization of deformation zone behavior, and a widely used power law for stress relation, equation 2.6, which considers the dependence of flow stress σ on temperature and strain-rate, Wrights were able to calculate the deformation zone length, L_D in an iterative manner.

$$\dot{\varepsilon} = \frac{\varepsilon}{t_{total}} = \frac{\varepsilon(V_{in} + V_{out})}{2L_D} \tag{2.5}$$

$$\sigma = K(\dot{\varepsilon})^m e^{(m\Delta H/RT)} \tag{2.6}$$

here K is the strength constant; m is the strain-rate sensitivity exponent; t_{total} is the total time spent moving from the entrance to the exit of the deformation zone; V_{in} and V_{out} are the ingoing and outgoing velocities of the moving material.

Naughton and Tiernan [34] determined the leading processing parameters for die-less wiredrawing experimentally. They successfully designed, constructed, instrumented and commissioned die-less drawing machine in 2009. The experimentally obtained results were compared with a deformation model proposed by Gue and Ridley [21] as:

$$\dot{\varepsilon} = C\sigma^n e^{(-\Delta H/RT)} \tag{2.7}$$

where n is the stress component constant; T is the working temperature; C is an scaling constant, which is temperature dependent.

The deformation model of Guo and Ridley [21] showed good agreement with the experimentally obtained results but failed to predict the behavior accurately at higher strain-rates, which is academic in any case since super-plasticity is characterized by low strain-rate.

Since the reduction of area only depends on the ratio of outgoing and ingoing axial speed [26], Wang et al. [51] suggested that it is possible to vary the diameter of the drawn workpiece

along its longitudinal axis simply by adjusting the velocity ratio in an appropriate way [51] and based on this dependency, Wang et al. established a mathematical model to determine the velocity in the deformation zone as a function of time in order to control the output diameter of the wire.

Similarly, Wengenroth et al. [54] demonstrated that by controlling the drawing velocity, variable cross sections could be produced. They have developed a one-dimensional thermo-mechanical model for the theoretical description of the process, which allows the final contour and temperature distribution to be calculated. However, only in a simple case of cone-contour an analytical solution could be derived and generally, the contours should be investigated by a numerical solution. Remarkably, in the case of linear drawing contour function the exit diameter shows a nonlinear increase with time.

In a different approach Manjoine and Nadai [32] completed an examination on the resistance to plastic deformation, on a selected choice of metals over a wide range of rates of deformation, at various temperatures. These researchers found that with the pure iron and iron alloys that were tested, at a set speed of straining, the resistance to deformation exhibits a minimum and maximum (blue brittleness) at certain temperatures. The blue brittleness moves to higher temperature with increasing speeds of straining. Thus, it is greatly advantageous to carry out die-less drawing at low strain/deformation rates and at elevated temperatures.

2.2.3 Stability

In order to analyze the stability of the process, one must identifies the key control variables. Naughton et al. [35] classified the process by five distinctive parameters as follows:

- Control: temperature, velocity and force.
- Material: density and inherent thermal properties.
- Mechanical: flow stress and longitudinal stress.

- Kinematic: strain and strain rate.

- Distribution and disturbance: inhomogeneity of material properties, radial heat distributions, and drawing velocities.

Naughton and Tiernan believed that stability is the key to a successful superplastic die-less wiredrawing, which is intrinsically linked to temperature. Von Eynatten [10] and other researchers [13] have reported that temperature needs to be controlled to within $\pm 1°C$ to ensure stability.

Regarding the stability of the process, many of the researchers consider deformation at steady state. However, if the necking occurs, the deformation will result in an unsteady state being reached. This plastic instability is more significantly noticeable at the early drawing stage, as the drawing speed increased from zero, which leads to occurrence of localized thinning [40]. This localized thinning causes low dimensional accuracy of the final product. In order to improve the low dimensional accuracy of the drawn material, which is due to the unsteady deformation in plastic instability, Furushima et al. [16] applied a strain hardening effect by gradually increasing the tensile speed from low speed to the target speed since the unsteady state hardly appears at low speeds. They have also investigated the effect of the strain-rate sensitivity index, m, and the strain-hardening coefficient, n, on the deformation profile. From the results, it was confirmed that high strain-rate-sensitive materials exhibit greater formability in the die-less drawing process.

Regarding the stability of the die-less drawing, He et al. [23] believed that geometric parameters at free boundary conditions exhibit uncertainty and have a strong coupling effect on the strain field and temperature fields. Therefore, the geometric parameters cannot be neglected if the instability criterion is considered; thus, the conventional instability criterion cannot be used in the die-less drawing process.

Based on the processing parameters of stable deformation, including the feeding speed, the distance between heater and cooler as well as the heating power He et al. [23] established a processing limit map. They carried out trials by changing individual processing parameter with pre-defined intervals until the deformation process became unstable, and thereby the upper and lower limit of the process parameters were defined.

The results indicated that each processing parameter exhibited both lower and upper limits of stable deformation based on the criterion of stable deformation with a diameter fluctuation of ±0.05mm in the desired output diameter. Moreover, both the temperature and its gradient, in the deformation region, increased with increasing heating power under stable deformation, but decreased with an increasing feeding speed. Furthermore, as the distance between cooling nuzzles and heater increased, the temperature of the deformation region increased, and the slope of the deformation region profile curves decreased.

In an attempt to assess the suitability of low carbon steel to the die-less drawing process Tiernan and Comerford [43] performed an experimental elevated temperature tensile test on a modified tensile testing machine. They have come to a conclusion from elevated tensile test results, that low rates of deformation and temperature in the range 600°C to 700°C would provide greater elongations in low carbon steel. Additionally, it was confirmed that carrying the test in a selected atmosphere would prevent the formation of an oxide layer on the surface of the deformed wire. The significance of scale formation, temperature, and grain structure to the die-less drawing process has been established.

2.3 Thermo-mechanical investigations

In the following subsections coupled and decoupled thermo-mechanical investigation of the die-less drawing process by different researchers have been reviewed.

2.3.1 Decoupled thermo-mechanical investigation by Fortunier

In order to analyze the die-less drawing process in detail, Fortunier et al. [13] applied a simple slicing method, where they considered each slice as a specimen to be subjected to a non-isothermal tensile test. However, the temperature in the slice was assumed to be homogeneous (gradients are neglected). Moreover, the maximum temperature reached by the wire during the process was shown to be the most important control parameter for a given area reduction, while the variations of this temperature had to remain within a very small interval to ensure stability and acceptably constant area reduction along the final product [13]. Furthermore, since the temperature gradient along r was neglected, the thermal balance between time t and $t+dt$ only involved diffusion along the wire axis and heating or cooling enforced by the device. Also, heating due to deformation as well as natural cooling by radiation and convection were assumed to be negligible. Taking into account all these assumption, the following relation was expressed:

$$\lambda \frac{d^2 T}{dx^2} - v \frac{dT}{dx} + \frac{\dot{q}}{\rho c} = 0 \qquad (2.8)$$

where $v = v(x)$ is the wire velocity in the slice under consideration; $\dot{q}$ denotes the thermal power per unit volume supplied by the heating $(\dot{q}_h > 0)$ or cooling $(\dot{q}_c < 0)$ system. The heating power obviously depends on the section of the slice under consideration; however, it was regarded as constant in each of the three heating, stretching and cooling zones in order to estimate the temperature distribution along the x-axis by a simple analytical derivation. Accordingly, the increase of velocity associated with the reduction of cross section was ignored in this thermal analysis and the velocity was considered to be constant.

The results obtained by this thermal analysis, however, could only be considered as qualitative since the temperature profiles were derived without taking into account the area reduction and thus the change in the wire velocity during the process.

Following their thermal analysis, Fortunier et al. [13] proposed a simple one-dimensional model to determine the mechanical parameters involved in die-less drawing process, which have a significant influence on plastic deformation. Considering a stationary material flow and load equilibrium along the wire, and by knowing the constitutive behavior of the material, Fortunier et al. were able to calculate the velocity $v = v(x)$ of the wire along the *x*-axis, which lead to an equation expressing F as a function of the area reduction ratio A_1/A_2.

The influence of material parameters, radial temperature gradient and various processing parameters on the process was also investigated. It turns out that when relatively large area reductions are to be achieved (e.g. $A_1/A_2 = 2$), a small change in load F -for example due to material or geometrical imperfections- results in a very large variation of the area reduction, especially when the strain-rate sensitivity parameter *m* is low. However, this effect is lower when the strain hardening coefficient *n* is large. Additionally, the radial temperature gradient induces a larger strain-rate in the wire, to the extent where the process stability may be affected. Furthermore, investigating the effect of Maximum Temperature Reached (MTR) in the wire shows, that for a relatively low MTR, large area reductions cannot be achieved, since the ductility of the material remains low, even though the process is stable (i.e. the slope of the curve in load vs. area reduction graph is strongly positive). However, when higher values of MTR are used, the process becomes rapidly unstable, but large reductions are possible. Therefore, MTR is the process parameter that has a major influence on stability and area reduction.

2.3.2 Decoupled thermo-mechanical investigation by Tiernan

Tiernan and Hillery [47] examined the capability of a continuous die-less drawing, whereas previous researcher of this process had confined their experimentation to a finite wire length. They designed and fabricated a machine to produce infinitely variable reductions in the cross-sectional areas of mild steel wires. Two mathematical models were developed separately to

describe the deformation and temperature profiles for mild steel. More importantly, a finite element analysis (FEA) of die-less drawing process was carried out using the FE software Forge2®. The model involved both mechanical and thermal loadings to simulate the drawing conditions on the die-less wiredrawing machine. The results obtained from the FE analysis were in accordance with those obtained experimentally and from the numerical analysis.

Tiernan and et al. [47] found a relationship between the variation in wire diameter along longitudinal axis and the percentage reduction in the range of 10 to 60 percent area reductions and the acquired data were successfully fitted to a power law. The utilization of an ironing die as an intermediate drawing step between die-less draws, considerably improved the wire profile in terms of roundness and concentricity. Moreover, the increase in strength and ductility shown by the die-less drawn wire was attributed to an improved residual pattern due to the absence of large thermal gradients in the wire during the process.

Tiernan and Hillery extended their work [46] by adding an automated data acquisition and machine control to the process. The data acquired was primarily to record the test parameter of the wire as it was formed, and secondly, to record data from the machine transducers to allow the control of the machine and monitoring it to be achieved. The enhanced temperature control system ensures isothermal condition, and thereby, minimizes the number of cold spots throughout of the wire in the deformation region.

In order to obtain knowledge of the geometry, stress distribution and metal flow in the deformation region, Tiernan and Hillery [45] further investigated the process. They used electrical resistances as a heating method in the process since it could be precisely controlled to allow uniformity of the temperature within narrow limits, which is vital for a neck free product. They believed that the resistance heating technology competes with both gas-fired and induction heaters, as it is cleaner and more efficient compared to gas heaters, and its equipment is less expensive than its induction counterpart.

2.3.3 Coupled thermo-mechanical investigation by Pawelski

Pawelski et al. [36] studied the influence of various process parameters in the die-less drawing process theoretically by applying a disk method, which resulted in a simplified system of thermal and mechanical equations. They assumed constant ingoing and outgoing velocities as well as a constant drawing force, in order to model the process at steady state. Using the volume constancy equation, they suggested the unknown shape function $r = r(x)$, which describe the change in the radius of wire as a function of x in the deformation zone, as:

$$\frac{dr}{dx} = -\frac{r^3}{2V_{in}r_0^2} \left\{ \frac{\sigma \exp(m_1 \cdot T)}{C(\varepsilon + \varepsilon_0)^{m_2} \exp\left[\frac{m_4}{(\varepsilon + \varepsilon_0)}\right]} \right\} \tag{2.9}$$

where V_{in} and r_0 are the ingoing velocity and radius of the wire respectively, and C, m_1, m_2, m_3 and m_4 are constants. The offset strain $\varepsilon_0 \approx 0.01$ is chosen to avoid zero stress for zero strain.

Regarding the temperature distribution, Pawelski et al. [36] assumed that temperature is only a function of the longitudinal coordinate x, and thus, the temperature gradient in the radial direction was neglected. Furthermore, it was found that the convective part of the heat transfer in the wire given by the drawing speed v, surpasses the diffusive (conduction) part nearly completely, when the appropriate data for die-less drawing are used, and therefore it can be excluded from the energy equation. Then, the simple thermal balance differential equation for the temperature distribution expressed as:

$$\frac{dT}{dx} + \frac{2\alpha \cdot r}{c\rho V_{in}r_0^2} \cdot T - \frac{2P \cdot r}{c\rho V_{in}r_0^2} = 0 \tag{2.10}$$

where α is the heat transfer coefficient and P is the inductive heating power per unit surface area of the wire.

The shape function *r(x)* and the temperature distribution *T(x)* were obtained numerically by solving a coupled system of ordinary differential equations of the first order consisting of the two Equations 2.9 and 2.10.

Finally, Pawelski et al. [36] investigated the process control for producing variable cross sections by utilizing the volume constancy principle and the fact that the exit radius in the process can be simply controlled by the ratio of ingoing and outgoing speeds V_{in}/V_{out}. Therefore by calculating the control parameter *v(t)*, two different contours, namely a cone-contour and a sinus-contour, have been produced.

2.3.4 Coupled thermo-mechanical investigation by Li

Since fine wires of diameter less than 1 mm were to be considered in Li's work, the radial and circumferential temperature variation was neglected and a one-dimensional thermo-mechanical analysis was carried out.

To model the deformation and describe the flow behavior of the wire, Li et al. [31] used a constitutive law based on the Voce's empirical relation, which accounts for the variation of stress with the strain, strain-rate and temperature as given below:

$$\sigma = \left[\sigma_i - (\sigma_i - \sigma_0) \cdot \exp(-n\varepsilon) \right] \left[\exp\left(\frac{-\eta \cdot T}{T_M} \right) \right] \left(\frac{\dot{\varepsilon}}{\dot{\varepsilon}_0} \right)^m \qquad (2.11)$$

where *n* is the strain-hardening factor; *m* is the strain-rate sensitivity index; η is temperature coefficient of the stress; T_M is the melting temperature of the wire; and $\dot{\varepsilon}_0$ is a scaling factor, which is generally taken as $1s^{-1}$; σ_i, σ_0, *m, n*, and η are material constant which were assumed to be temperature independent for simplicity.

Substituting radial strain and strain-rate equations into the Equation 2.11, and by noting that the drawing force along the wire axis is constant, i.e. $F = \pi r^2 \sigma$, Equation 2.11 can be rewritten as [31]:

$$\frac{dr}{dx} = -\frac{\dot{\varepsilon}_0 r^3}{2V_{in} r_0^2} \left\{ \frac{F}{\pi r^2(x)\left[\sigma_i - (\sigma_i - \sigma_0)\left(\dfrac{r}{r_0}\right)^{2n}\right]\exp\left(\dfrac{-\eta \cdot T}{T_M}\right)} \right\}$$ (2.12)

which is the governing equation for radius profile along longitudinal axis of the wire. Here, v is the velocity of the wire, which varies with x in the deformation region; r is the radius of the wire as a function of x; the subscript i denote the initial values of velocity and radius.

By considering heat conduction, heat convection and radiation in the energy balance of a disk element of the wire, the following differential equation was suggested by Li et al. [31] as heat equation:

$$\frac{d^2T}{dx^2} + \left(\frac{2}{r}\frac{dr}{dx} - \frac{v}{\lambda}\right) \cdot \frac{dT}{dx} - \frac{2\alpha}{k \cdot r}(T - T_0) + \frac{2A \cdot P}{\pi^2 ab \cdot k \cdot r^2} \cdot \exp\left(-\frac{2x^2}{a^2}\right) \cdot \int_{-r}^{r} \exp\left(-\frac{2y^2}{b^2}\right) dy = 0$$ (2.13)

here A is the absorptivity of the wire at the incident laser wavelength; T and T_0 denote the temperature of the wire and the ambient temperature respectively; P is the incident laser power; and k, λ and α are respectively, the thermal conductivity, the thermal diffusivity and the heat transfer coefficient of the wire; a and b are the major axis lengths of the laser beam. Equations 2.12 and 2.13 form a system of two ordinary differential equations that can be solved numerically to obtain a temperature distribution and radius profile as a function of longitudinal axis, x.

Li et al. [31] concluded that the temperature field in the wire depends on many factors such as the incident laser power, position of the wire relative to the laser beam center and drawing velocity. Likewise, it is affected by the absorptivity, which depends on surface quality and temperature of the wire. These variabilities make the control and "stability" difficult.

2.3.5 Coupled thermo-mechanical investigation by Huh

Based on a hot-working principle, Huh et al. [24] employed microwaves as heating source for the die-less drawing process. An ultrahigh frequency wave of 2.45 GHz known as microwave along with a susceptor (SiC), which enhances the thermal coupling effect between the steel and microwave, were used.

Huh et al. [24] modeled the wire deformation in the deformation zone theoretically by considering the cooling effect and the Bingham model with the power law and Zener-Hollomon parameter [56] for the constitutive equation. Introducing state variables such as the wire velocity, the cross sectional area and the wire temperature, Huh et al. [24] employed the governing equations suggested by Kim et al. [25] in order to describe the dynamic of the wiredrawing process. The governing system of equations consists of equations for the mass, momentum, and the energy balance, given as:

$$\frac{\partial\{\rho \cdot A(t,x)\}}{\partial t} = -\frac{\partial\{\rho \cdot A(t,x) \cdot v(t,x)\}}{\partial x} \tag{2.14}$$

$$\frac{\partial\{\rho \cdot A(t,x) \cdot v(t,x)\}}{\partial t} = -\frac{\partial\{\rho \cdot A(t,x) \cdot v(t,x)^2\}}{\partial x} + \frac{\partial f(t,x)}{\partial x} \tag{2.15}$$

$$q_0 = c \cdot \left[\frac{\partial T(t,x)}{\partial t} + v(t,x) \cdot \frac{\partial T(t,x)}{\partial x} \right] \tag{2.16}$$

where ρ and $A(t,x)$ denote the wire density and the wire cross-sectional area at time t and position x, respectively; $v(t,x)$ stands for velocity of the wire at (t,x), and $T(t,x)$ represents the temperature of the wire at (t,x); $f(t,x)$ is the force acting on the wire cross section at (t,x) and q_0 is the heat generation rate per mass of the wire and it is derived via convective (material) derivative of temperature with respect to time for a given energy source; c stands for the specific heat of the wire material. Due to the shape feature of the wire that has a very small radius, a uniform

temperature distribution in the radial direction was assumed. Also, a constant wire density with negligible air drag effect, were considered in the calculations. The heat loss in the deformation zone was calculated via the difference in the temperature of the wire with a fixed temperature (softening temperature of the material) through introduction of a heat loss coefficient h, which was measured experimentally.

In this study however, the cooling effect due to heat transfer between the wire and the surroundings environment was considered to be the main cooling mechanism and the heat loss in the deformation zone was calculated via the difference in the temperature of the wire and its surrounding environment temperature (298 K); thus, the cooling transfer coefficient h is the heat transfer coefficient between steel and air in the derivation of energy equation (Equation 3.8).

As generally dictated by the power law, stress depends on temperature and strain-rate, which are interrelated to Zener-Hollomon parameter [56], for large deformations, Huh et al. [24] employed the widely used simple form of constitutive law suggested by Tiernan and Hillery [46] to describe the deformation behavior of the material as:

$$\sigma = \gamma \cdot Z^{1/n} = \gamma \cdot e^{\Delta H / (n \cdot R \cdot T(t,x))} \cdot \left[\frac{\partial v(t,x)}{\partial x} \right]^{1/n} \tag{2.17}$$

where σ is the stress, n is the stress exponent, ΔH is the activation energy for state transition or plastic flow deformation of the wire and γ is a proportionality constant.

To confirm the model describing the die-less drawing dynamics, Huh et al. [24] considered the steady state, where any change of velocity with respect to time does not occur, i.e. $\frac{\partial v(t,x)}{\partial t} = 0$. This reduces the problem to a one-dimensional deformation model.

Experimental results [24] at steady state conditions demonstrated that the new method was effectively applicable to draw a stainless steel wire with a high reduction ratio. Furthermore,

the experimental results corresponded well with the simulated results, which indicate that the derived mathematical model for wiredrawing can well describe the real drawing process.

2.4 Die-less tube drawing

Furushima et al. [14,15,16,17,18] investigated the effectiveness of the die-less drawing process for fabricating micro-scale tubes. Studying the effect of various factors independently, such as process condition and material properties, by means of experiments, was however, limited. Because, it is very difficult to experimentally observe in detail the deformation behavior of tubes during die-less drawing at micro-scale. Consequently, no detailed experimental studies were reported, indicating the necessity of a more accurate numerical investigation.

Furushima et al. [18] utilized the die-less drawing process to draw micro-tubes for the first time. They performed a coupled thermo-mechanical analysis for die-less tube drawing using the finite element method (FEM), and from the results, they suggested that the die-less tube drawing is essential to produce extra fine micro-tubes by reason of keeping the cylindrical tube diameter ratio constant with extremely high reduction.

Furushima et al. [14] further developed the process by verifying the effectiveness of die-less drawing as a method for fabricating micro-tubes numerically, as it was demonstrated experimentally only in their previous work [15]. In addition, since unstable deformations occurred for very fine tubes by single pass drawing, multi-pass die-less drawing seemed essential for fabricating finer micro-tubes and therefore, the effect of the number of drawing passes on the surface roughness of superplastic micro-tubes fabricated by multi-pass die-less drawing was investigated, and an increase in roughness on the inside and outside surfaces of the tube was observed after the one-pass drawing. On the other hand the roughness decreased gradually and converged to a value after the two-pass drawing, which implied that the roughening phenomenon on the free surface is restrained in a multi-pass die-less drawing.

Furushima et al. [14] analyzed the deformation behavior of superplastic Zn-22%Al and AZ31 magnesium alloy tubes using FEM with a coupled thermo-mechanical model. Although the FEM results were in good agreement with the experimental ones, there was an unstable deformation behavior of the Zn-22%Al at early stage of drawing and at lower temperature. Furushima et al. believed that the difference in deformation behavior at different temperatures comes from the difference between the strain-rate sensitivity m values at different test temperatures, because a higher m value restrains the local unstable deformation. For instance, although the strain-hardening coefficient, n is sufficiently large for AZ31 magnesium alloy, its m value at high temperature is considerably lower than that of Zn-22%Al alloys and for this reason, the instable deformation behavior occurred notably at early drawing stage.

According to the Furushima et al. new heat transfer model [16], the temperature distribution of the tubes during die-less drawing is changing in accordance with the heat supplied from the heating coil, the heat conduction inside the tube, and the heat transfer from the tube to the cooling air from the cooling coil and that from the tube to the atmosphere. The material modeled as a tube, is considered to be strain-rate sensitive and strain hardening dependent, where both strain-rate sensitivity index and strain hardening coefficient are temperature dependent. Furushima et al. used the heat conduction equation of axisymmetric model in an unsteady state and by considering the factors mentioned above that can be expressed as:

$$k\left\{\frac{1}{r}\frac{\partial}{\partial r}\left(r\frac{\partial T}{\partial r}\right)+\frac{\partial^2 T}{\partial z^2}\right\}-c\rho\frac{dT}{dt}+\dot{q}=0 \qquad (2.18)$$

where k is the thermal conductivity; c is the specific heat; ρ is the mass density; and $\dot{q}$ is the heat generated per unit time and unit volume.

With increasing tensile speed (i.e. pulling speed) the reduction in area, RA increases and the outer diameter of the tube D decreases. Furushima et al. [16] defined the degree of unstable deformation of tubes as:

$$\frac{\Delta D}{D_{ave}} = \frac{D_{ave} - D_{min}}{D_{ave}} \qquad (2.19)$$

where D_{ave} is the outer diameter in the steady state and D_{min} is the minimum outer diameter of unstably deformed part. The unstable deformation rate $\frac{\Delta D}{D_{ave}}$ can be used as an index for evaluating the risk of fracture, since $\frac{\Delta D}{D_{ave}}$ increases with increasing RA. A higher unstable deformation rate results in a higher risk of fracture at non-steady state in the initial stages of drawing. Approximating the relationship between the material characteristics and temperature to be linear in the working temperature range, Furushima et al. [16] concluded that generally, unstable deformation rates are suppressed with high m value regardless of the n value, suggesting a low probability of breakage in the unsteady state. On the other hand, the n value affects the unstable deformation rate greatly in the case of low m values, but negligibly in the case of high m values.

2.5   Recent works

Wire fracture during processing can be prevented by a load-control algorithm that allows the wire and bars to be drawn to a close dimensional tolerance in the steady state region of the test specimen. The load-control approach has improved the process in terms of the quality of finished product and percentage reduction achievable per pass. Carolin et al. [7] could maintain tolerances between 0.01 mm to 0.1 mm when drawing a bar of 5 mm in diameter to reduction in area of up to 35.5% by utilizing load-control procedure. However, the maximum velocity achieved was 5 mm/min at a testing temperature of 750°C, which is low for commercial production purposes.

Tiernan et al. [44] initiated an experimental research program to further investigate and improve the die-less drawing process. They developed a novel approach for controlling the deformation load to ensure that large uniform reductions in the rod's cross-sectional area can be achieved. The novel aspect, i.e. load-control, where the onset of yield is identified, permits the production of a uniform-cross-section wire over its length. Additionally, even though the load-control concept reduces the amount of achievable deformation, it still allows the invaluable bonus of preventing tensile failure in the rods at high process ratios.

Tiernan et al. [44] concluded that the die-less drawing process is feasible by precisely controlling the following parameters: velocity, temperature, and heating and cooling rates. On the other hand, the variation of cross-sectional area along the wire length caused plastic deformation to be concentrated at a narrow zone, which caused wire breaks.

Furushima et al. [17] suggested a new effective method, i.e. path control method, for controlling the drawing speed in the early drawing stage to restrain the unstable deformation that usually leads to fracture. Previous reports on die-less drawing stability did not differentiate between the fracture caused by unstable deformation in the early drawing stage and fracture caused by the forming limit based on the difference in the flow stress of material between the heated and cooled zone.

From the experimental results, Furushima et al. [17] concluded that an effective drawing speed control enhances the forming limit in a die-less drawing. It was also found that the forming limit slightly improves with increasing heating along the length. Moreover, using the path control method, the forming limit of the metal can be evaluated appropriately under unaffected condition of the unstable deformation that occurred in the early drawing stage. Also, it was found that the unstable deformation could be restrained with decreasing drawing acceleration.

Finally, Furushima et al. [17] proposed the interesting idea that if the deformation behavior in the die-less drawing moves to a steady state, the forming limit depends only on the difference in the flow stress based on the difference in temperature, and hence, the local heating in the die-less drawing is unnecessary.

Twohig et al. [48] experimentally studied the die-less drawing of Nickel-Titanium by varying the established critical process parameters of temperature, heating and cooling rates, and drawing velocity. By superimposing the radial profile along the length of the wire onto the loading profile obtained from the trail results, a clear correlation between the applied load and the cross-sectional reductions during the process was observed. It was concluded that for a successful draw, it is extremely important to keep the values of stress, strain and strain-rate constant to prevent an unsteady necking of the rod and a high radial dimensional variance along the rod or wire length.

CHAPTER 3

DIE-LESS DRAWING PROCESS MODELING

3.1 Overview

The literature review revealed that varying levels of success have been achieved with die-less drawing. However, it is apparent that producing repeatable and uniform reductions with a difficult-to-process material still remains a challenge. This study aims at characterizing and improving of the die-less drawing process by introducing, investigating and developing a mathematical model of die-less drawing.

The process consists of a fixed heat source, with the stock material being fed into the deformation zone at a velocity V_{in}, and pulled out with a velocity V_{out} greater than V_{in}. Because of the differential speed in the material flow, the stock material will be subjected to a state of tensile force along its longitudinal axis. Consequently, when the stress that has been induced in the material exceeds the lowered tensile strength of the material at the drawing temperature, the stock material yields. The mechanical loading causes a local deformation to be initiated in the heated area and as the deformed increment leaves the heated area, its temperature begins to drop.

The deformation process is halted as soon as the material enters the cooling unit, where the material recovers its strength.

The heat source should have the ability to heat up the moving material very quickly, and precisely at the same time. The different types of heating methods used in previous studies include: induction, laser, resistive, and radiative heating sources. Many researchers, including Pawelski et al. [37], Naughton et al. [33], Kobatake et al. [26] believed that induction heating is superior to any other heat source in view of the requirement for local heating, the ability to produce high heating rates with a uniform heating of the material and by controlling temperature. Laser die-less drawing has been used for heating fine Nickel wires [30]. A radiative heating method, using microwave [23], and a resistive heating method, using the wire heat flux resistance [47], have also been successful.

Employing an induction-heating method, the temperature of the material depends on factors such as the power of the induction-heating source, the heating time, the shape of the induction coil, the distance between the induction coil and the material and the material physical parameters (specific heat, density, thermal conductivity, permeability). Despite the precise heating control ability of the induction coil, marking the exact location of the desired temperature on the moving material is almost impossible. Undoubtedly, the novel load-control approach taken by Tiernan et al. [44] and Twohig et al. [48], to some extent, enhanced the accuracy in detecting the location of the yielding onset. In order to avoid tensile failure (rupture) of the workpiece, they used a load-control function in the die-less drawing experiments, which stopped the machine draw-head motion when the drawing load had reached a pre-determined value. However, to date, it has been assumed in the analysis that the temperature reaches its maximum precisely at the exit of the induction coil in order to define the contour of the deformation zone. For instance, Wright et al. [55] assumed that a desired average radial

temperature occurs exactly at the beginning of the set deformation region, while the exact location of yielding could only be approximated.

Nevertheless if the heating unit could provide a variable heating power along the heating zone during the process and by positioning a thermocouple in the heating unit, it would be possible to measure and adjust the temperature profile experienced by the surface of the material. This allows the temperature of the material in the deformation region to be monitored while it is being heated, and thereby, by employing a closed loop real-time feedback control system, the desired maximum temperature can be maintained at the exit of the heating unit. This heating unit would have the particularity to deliver heat to the wire with varying power along the heating zone in order to maintain the desired maximum temperature at the beginning of the deformation region. For instance, in mathematical modeling of the process, with the zero set at the exit of induction coil where material reaches its maximum temperature in the process, a modified heating source can ensure that the material at the exit of the induction coil experiences the same process conditions such as the temperature and the tensile stress, and therefore a uniform deformation will result.

3.2 Deformation models

Researchers have utilized a variety of plastic flow stress models in order to simulate large deformations of metal at elevated temperatures and high strain-rates. Several of such models exist and it is difficult to determine the applicability of any single model to a particular problem at hand. Regarding die-less drawing however, the temperature and strain-rate dependence of the stress is fundamental. In essence, material and process parameters (e.g. specific heat, shear modulus, etc.) are temperature and strain-rate dependent especially at a working temperature range of the die-less drawing; thus, one can analyze the process more accurately by including the parameters as temperature-dependent variables in the deformation model and not as constants.

Plastic flow stress models and the associated specific heat, shear modulus, melting temperature, and equation of state models are sub-grid scale models of a complex deformation phenomenon. It is unreasonable to expect that any one model will be able to capture all sub-grid scale physics under all possible conditions. However, utilizing the model that is best suited to the regime of interest (die-less drawing) is vital for the analysis.

Although in most computations involving plastic deformations the shear modulus, the specific heat, and the melting temperature are assumed to be constant, the shear modulus is known to vary with temperature and pressure (stress). Also, most of the materials have specific heat coefficient that can change significantly with changes in temperature. Additionally, the temperature increase due to the dissipation of plastic work can be added by using a variable specific heat model.

Melting temperature can increase dramatically at high pressure. In large deformation, a melting temperature model can be used to determine if the material has melted locally. However, in die-less drawing with a constant material density in the working temperature range, the compression ratio is equal to 1, i.e. $\eta=1$, and consequently different models predict a constant melt temperature. For instance, the Steinberg-Cochran-Guinan (SCG) melt model [40] with $\eta=1$ will result in melting temperature of material at working temperature to be approximately equal to the material melt temperature at room temperature, and therefore, it was assumed to be constant in this study.

3.2.1 Shear modulus model

The shear modulus value of metals usually decreases with increasing temperature. The value of shear modulus at room temperature is around 150% of the value when near melting temperature, and thus, using the room temperature value of shear modulus in modeling high temperature deformation processes will overestimate the shear stiffness of the material.

35

Several models exist that attempt to predict the shear modulus of metals. Among various shear modulus models that have been used in plastic flow computations, the Mechanical Threshold Stress (MTS) shear modulus model [50,8] is of special interest to the author since it has been used in conjunction with the MTS flow stress model [9,12,20]. Varshni [50] developed the MTS shear modulus model in 1970 and it has the form:

$$\mu(T) = \mu_0 - \frac{D}{\exp(T_0/T) - 1} \tag{3.1}$$

where μ_0 is the shear modulus at 0K, and D, T_0 are empirical parameter. It can be understood from Equation 3.1 that this MTS model does not include any pressure-dependency of the shear modulus and is not applicable for high-pressure applications. However, it can be applied to die-less wiredrawing, as the process is dominantly temperature sensitive. The parameters used in the MTS shear modulus model for HY-100 steel [20] are shown in Table 1.

Table 1: Parameters used in the MTS shear modulus model for HY-100 steel. (Source: The mechanical threshold stress constitutive-strength model description of HY-100 steel by Goto [20])

Parameter	μ_0 (MPa)	D (MPa)	T_0 (K)
Value	71460	2910	204

3.2.2 Specific heat model

If the working temperature range and strain-rate range are small, the variation of the specific heat capacity with temperature can be ignored. Nevertheless, a change in temperature from ambient values to one that are close to melt temperature requires that temperature-dependency of this physical property to be considered in the modeling of the die-less drawing process. Essentially, the effect of higher specific heat at high temperature is to reduce the rate of increase of temperature with plastic strain.

There is a limited test data on the specific heat of steel. Kodur et al. [27] reviewed the high-temperature constitutive relationships for steel currently available in American and European standards, and highlighted the variation between these relationships through comparison with published experimental results.

The published specific heat model results vary considerably above 700°C. In general, the specific heat of steel increases with an increase in temperature with a large spike occurring around 750°C. The increase in specific heat with temperature is due to individual atoms in steel moving farther apart, thus achieving a higher energy state. The spike in the specific heat at around 750°C is due to the phase change that occurs in steel in which the atoms transition from a face centered cubic (F.C.C.) α phase structure to a body centered cubic (B.C.C.) γ phase structure. This process absorbs considerable energy (heat), thus accounting for the spike around 750°C. Furthermore, if we assume a constant (at room temperature) specific heat, there will be an unrealistic increase in temperature close to the phase transition that can cause premature melting in numerical simulations and associated numerical problems.

Goto et al. [20] developed an empirical relation for the temperature-dependent specific heat of HY-100 steel, which was hired in this study to account for a temperature dependent specific heat, given as:

$$c = 0.09278 + 7.454 \times 10^{-4} \cdot T + \frac{12404}{T^2} \qquad (3.2)$$

3.2.3 Flow stress model

The MTS model is a complex model that is based on ideas from dislocation dynamics, which belong to the realm of physics. This model has been used to describe the plastic deformation of numerous metals and their alloys such as copper, tantalum [12], HY-100 steel [20], and alloys of steel [2,3,4]. This study focuses only on HY-100 steel and uses the data

provided by Goto [20], since calculating the MTS model parameters, is a lengthy task that is beyond the scope of this research study.

The MTS model [3] has the following relation for the flow stress:

$$\sigma(\varepsilon_p, \dot{\varepsilon}_p, T) = \sigma_a + (S_i \sigma_i + S_e \sigma_e) \frac{\mu(p, T)}{\mu_0} \qquad (3.3)$$

where $\sigma(\varepsilon_p, \dot{\varepsilon}_p, T)$ is the strain, strain-rate and temperature dependent flow stress, ε_p is the plastic strain, $\dot{\varepsilon}_p$ is the strain-rate, T is the temperature, σ_a is the athermal component of the flow stress, μ_0 is the shear modulus at 0K and ambient pressure, σ_i is the intrinsic component of the flow stress due to barriers to thermally activated dislocation motion, and σ_e is the strain hardening component of the flow stress.

The athermal component of mechanical threshold stress, σ_a, is a function of grain size, dislocation density, distribution of solute atoms, and other long-range barriers to dislocation motion [4]. This parameter is dependent on the Hall-Petch effect[1] (grain-boundary strengthening) and hence characteristic martensitic packet size. However, since we do not have unambiguous grain sizes and other information needed to determine σ_a, based on value used by Goto et al. [20] for HY-100 steel, we have assumed that σ_a is constant and it equal to 40 MPa.

The scaling factors S_i and S_e are temperature and strain rate dependent and take the Arrhenius form as:

$$S_i = \left[1 - \left(\frac{k_b T}{g_{0i} b^3 \mu(T)} \ln \frac{\dot{\varepsilon}_{0i}}{\dot{\varepsilon}} \right)^{1/q_i} \right]^{1/p_i} \qquad (3.4)$$

---

[1] Hall-Petch effect (grain-boundary strengthening) is the relation between yield point and grain size of the material. It gives a quantitative description of an increase in the yield stress of a polycrystalline material as its grain size decreases.

$$S_e = \left[1 - \left(\frac{k_b T}{g_{0e} b^3 \mu(T)} \ln \frac{\dot{\varepsilon}_{0e}}{\dot{\varepsilon}}\right)^{1/q_e}\right]^{1/p_e}$$ (3.5)

where k_b is the Boltzmann constant[2], b is the magnitude of the Burgers[3] vector, (g_{0i}, g_{0e}) are normalized activation energies, $(\dot{\varepsilon}_{0i}, \dot{\varepsilon}_{0e})$ are constant reference strain-rates, and (q_i, p_i, q_e, p_e) are constants. These parameters and constants used in the flow stress model of HY-100 steel [20] are shown in Table 2.

Table 2: Constants and parameters used in MTS model for HY-100 steel. (Source: The mechanical threshold stress constitutive-strength model description of HY-100 steel by Goto [20])

Parameter	Value	Parameter	Value
σ_a (MPa)	40	g_{0i}	1.161
σ_i (MPa)	1341	q_i	1.5
k_b (J/K)	1.38E-23	p_i	0.5
b (m)	2.48E-10	g_{0e}	1.6
ρ (kg/m^3)	7860	q_e	1
$\dot{\varepsilon}_{0i}$ (s^{-1})	10E-13	p_e	0.75
$\dot{\varepsilon}_{0g}$ (s^{-1})	10E-7		

A detailed determination of flow stress model parameters for some steel alloys can be found elsewhere [18,7,3].

3.3 Thermal Analysis

The idea of die-less drawing of a wire or bar is to replace the mechanical drawing die by a local heating unit with a following cooling device. The local temperature increase lowers the yield stress of the workpiece (wire) material and causes a local plastic deformation. If the applied drawing stress is high enough, the wire begins to neck. The subsequent cooling of the deformed

---

[2] Boltzmann constant is a physical constant relating energy at individual particle level with temperature.
[3] Burgers vector is a vector that represents the magnitude and direction of lattice distortion of dislocation in a crystal lattice.

part controls this local necking. Two approaches among different others related to the thermal analysis, were investigated here.

3.3.1 Approach 1: Heat conduction

Pawelski et al. [37] and Wengenroth et al. [54] considered only the heat conduction in the thermal analysis and suggested a solution to the heat conduction equation for the die-less drawing process. By assuming axial symmetry, constant thermal conductivity (k) and constant density (ρ), and by considering a constant temperature distribution in relation to the heating unit (inductor) steady state deformation will result. By employing the above-mentioned assumptions, the general cylindrical heat conduction equation can be rearranged to [54]:

$$\frac{\partial T}{\partial t} + v_x \frac{\partial T}{\partial x} + v_r \frac{\partial T}{\partial r} = \lambda \left(\frac{\partial^2 T}{\partial x^2} + \frac{\partial^2 T}{\partial r^2} + \frac{1}{r} \frac{\partial T}{\partial r} \right) + \frac{P}{\rho c} \qquad (3.6)$$

where $\lambda = \dfrac{k}{\rho c}$ is the thermal diffusivity; T and P are temperature and heating/cooling power as a function of radius r, longitudinal axis x, and time t; v_x and v_r are the velocities in the longitudinal and radial directions respectively. Additionally, the heat induction power, physically a volumetric power, can be treated as an area-related surface power, if the skin depth of the induction heating is small compared to the radius so the heating power can be considered as a boundary condition [37].

By assuming an exponential distribution along the longitudinal direction x and a Bessel distribution along the radial direction r, Pawelski et al. [37] obtained a complete analytical solution (Equation 2.2) to the general cylindrical heat conduction equation for die-less drawing.

Despite of the analytical solution, Pawelski could not entirely describe the dynamics of the die-less drawing process, since continuity and momentum equations were not included in the modeling.

3.3.2 Approach 2: Heat convection

As mentioned before (See section 2.3.5), Kim et al. [25] suggested a system of governing equation in order to describe the dynamics of the die-less drawing process. The system consists of the equations of conservation of mass, momentum and energy balance.

The energy balance can be described in reference to Figure 3.1, which is the dynamic model of the drawn wire in the deformation zone.
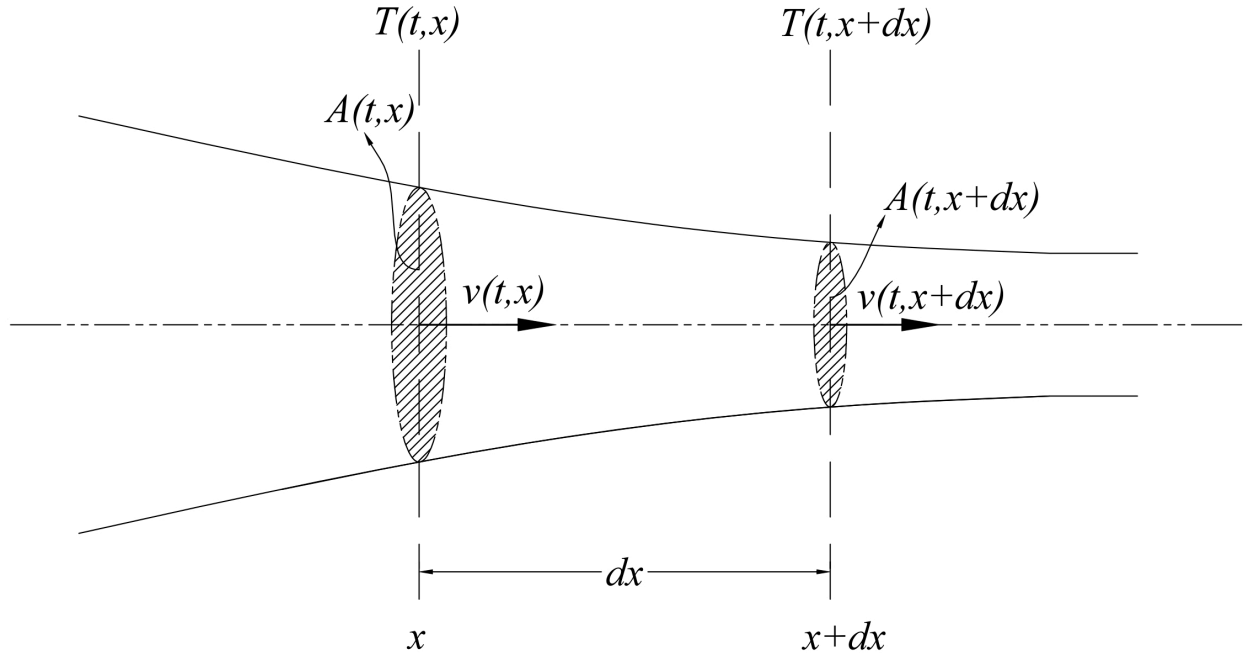

Figure 3.1: Dynamic model of the drawn wire in the deformation zone

During the die-less wiredrawing, energy exchange occurs between the neighboring surfaces by conduction due to an existing temperature gradient and by convection due to the motion of the wire. The heat flow through the cross section $Q(t,x)$, that takes into account the

heat conduction and heat convection of the wire moving with a velocity *v(t,x)* can be expressed

as :

$$Q(t,x) = -A(t,x) \cdot k \cdot \frac{\partial T(t,x)}{\partial x} + c \cdot \rho \cdot v(t,x) \cdot A(t,x) \cdot T(t,x) \qquad (3.7)$$

However, since the effect of the heat conduction along the wire axis was very small in

comparison to the heat convection by wire movement and to the heat generation by microwaves,

Kim et al. [25] and Pawelski et al. [36] neglected the heat conduction in their derivations.

By introducing the cooling transfer co-efficient *h* (See section 2.3.5) for the cooling

effect of the wire, and by including the heat generated in the wire in the energy balance equation,

the total energy accumulation rate of the control volume consisting of the wire section between *x*

and *x+dx* for a constant volume deformation is given by Equation 3.8 [25] as:

$$\frac{\partial T(t,x)}{\partial t} = \frac{k}{c\rho \cdot A(t,x)} \cdot \frac{\partial}{\partial x}\left[A(t,x) \cdot \frac{\partial T(t,x)}{\partial x}\right] - v(t,x) \cdot \frac{\partial T(t,x)}{\partial x} + \frac{q_0}{c} - \frac{2h\sqrt{\pi}}{c\rho} \cdot \frac{T(t,x) - T_0}{\sqrt{A(t,x)}} \quad (3.8)$$

It should be noted that the wire is assumed to deform at a higher temperature than its

softening temperature T_0, and also, its viscous strain energy is small enough to be neglected in

comparison to the heat generation and the heat convection due to the wire movement.

This study utilizes the second approach by investigating the thermal process as well as

the mechanical characteristics. Since the temperature in the deformation zone is one of the main

control parameters of the process and has to remain within a very small range (typically $\pm 1°C$

[10]), the heat conduction in the wire is included in the energy equation and also, the heat loss

mechanism has been modified (See section 2.3.5). However, the third term ($\frac{q_0}{c}$) in the right hand

side of Equation 3.8 is neglected in this study, since it represent the heat generated in the

deformation zone by the dielectric energy dissipation.

3.4 Governing system of equations

A dynamic process can be expressed in the form of a continuity equation and an equation of motion. However, since the energy exchange occurs in the die-less wiredrawing process, which is temperature sensitive, an energy equation has to be included and solved simultaneously along with the continuity equation and the equation of motion.

In order to analyze the complex dynamic thermo-mechanical process in time and space it is first essential to define the state variables required to describe the process at any time and at any location in the deformation zone under consideration. According to Kim et al. [25], the governing system of equations consists of the equations of mass, momentum and energy balance, where state variables such as temperature, cross-sectional area and drawing velocity have been employed. However, in order to describe the deformation in the heated zone using the MTS constitutive model, the rate of change of a reference stress with respect to strain (structure evolution) has to be considered in the analysis. The problem has been taken care of by introducing a new state variable representing the structure evolution, the mechanical threshold stress $\sigma_e(t,x)$, which is the strain hardening component of flow stress, and by adding its rate of change with respect to strain to the governing system of equations.

The mass density of the wire was assumed to be constant (incompressible flow) and the air drag effect negligible. Also, since the deformations are large the elastic deformation has been excluded in this analysis. The governing system of equations applied in this study, consists of four Partial Differential Equations (PDE) for mass and momentum conservation, the energy balance and the equation for mechanical threshold stress, given as:

$$\frac{\partial}{\partial t}\{A(t,x)\} = -\left\{v(t,x)\cdot\frac{\partial A(t,x)}{\partial x} + A(t,x)\cdot\frac{\partial v(t,x)}{\partial x}\right\} \tag{3.9}$$

$$\frac{\partial}{\partial t}\{v(t,x)\} = -v(t,x)\cdot\frac{\partial v(t,x)}{\partial x} + \frac{\sigma(T,\sigma_e;t,x)}{\rho\cdot A(t,x)}\cdot\frac{\partial A(t,x)}{\partial x} + \frac{1}{\rho}\cdot\frac{\partial\sigma(T,\sigma_e;t,x)}{\partial x} \tag{3.10}$$

$$\frac{\partial}{\partial t}\{T(t,x)\} = \frac{k}{\rho \cdot c(T;t,x) \cdot A(t,x)} \cdot \frac{\partial A(t,x)}{\partial x} \cdot \frac{\partial T(t,x)}{\partial x} + \frac{k}{\rho \cdot c(T;t,x)} \cdot \frac{\partial^2 T(t,x)}{\partial x^2} - v(t,x) \cdot \frac{\partial T(t,x)}{\partial x} - \frac{2h\sqrt{\pi}}{\rho \cdot c(T;t,x)} \cdot \frac{T(t,x) - T_0}{\sqrt{A(t,x)}} \qquad (3.11)$$

$$\frac{\partial}{\partial t}\{\sigma_e(t,x)\} = \theta(T;t,x) \cdot \frac{\partial v(t,x)}{\partial x} \cdot \left[1 - \frac{\tanh\left(\kappa \frac{\sigma_e(t,x)}{\sigma_{eS}(v,T;t,x)}\right)}{\tanh(\kappa)} \right] \qquad (3.12)$$

where $A(t,x)$, $v(t,x)$, $T(t,x)$, and $\sigma_e(t,x)$ represent the state variables cross-sectional area, drawing velocity, temperature and mechanical threshold stress at (t,x), correspondingly; $c(T;t,x)$ and $\theta(T;t,x)$ are temperature dependent specific heat and strain hardening coefficient, respectively; and $\sigma_{eS}(v,T;t,x)$ is a temperature and velocity dependent reference stress; k is the thermal conductivity of the wire; and ρ denotes the mass density and κ is an empirical best-fit constant that dictates the rate at which saturation is achieved and was taken as 2 [20].

Figure 3.2 shows a volume element along the longitudinal axis of moving material chosen between x and $x+dx$ that is used in the derivation of Equation 3.9. According to the law of conservation of mass (i.e. mass continuity equation), the rate of the change of the mass defined over a control volume (Figure 3.2) must be equal to the amount of matter crossing the boundaries of the control volume plus what is created (or consumed) by sources (or sinks) inside the control volume.

In order to include the effect of the changes in the cross-sectional area in the derivations, it was kept together with the mass density ρ in the derivation of Equations 3.9 and 3.10.
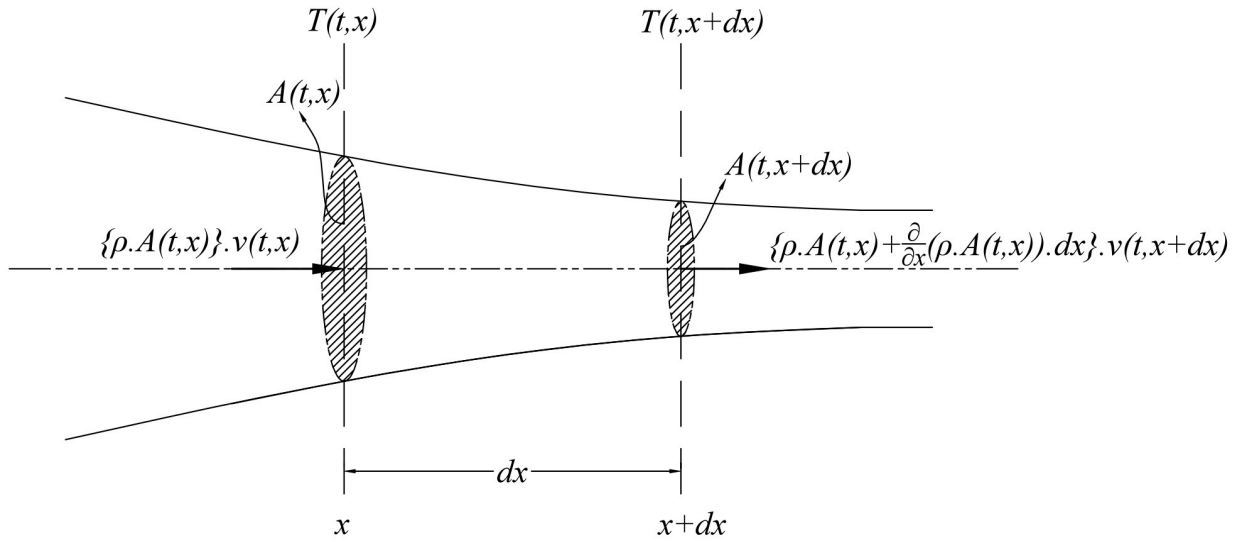
Figure 3.2: Material flow through the boundaries of control volume between x and x+dx

Equation 3.10 was derived from the law of conservation of momentum in the longitudinal direction while employing the MTS model to describe the load-deformation behavior of the process. Referring to Figure 3.3, the change of momentum of the control volume between x and $x+dx$ have two parts, momentum due to the material crossing through the cross-sectional area $A(t,x)$, and the force applied to the moving material $f(t,x) = A(t,x) \cdot \sigma(v,T;t,x)$.
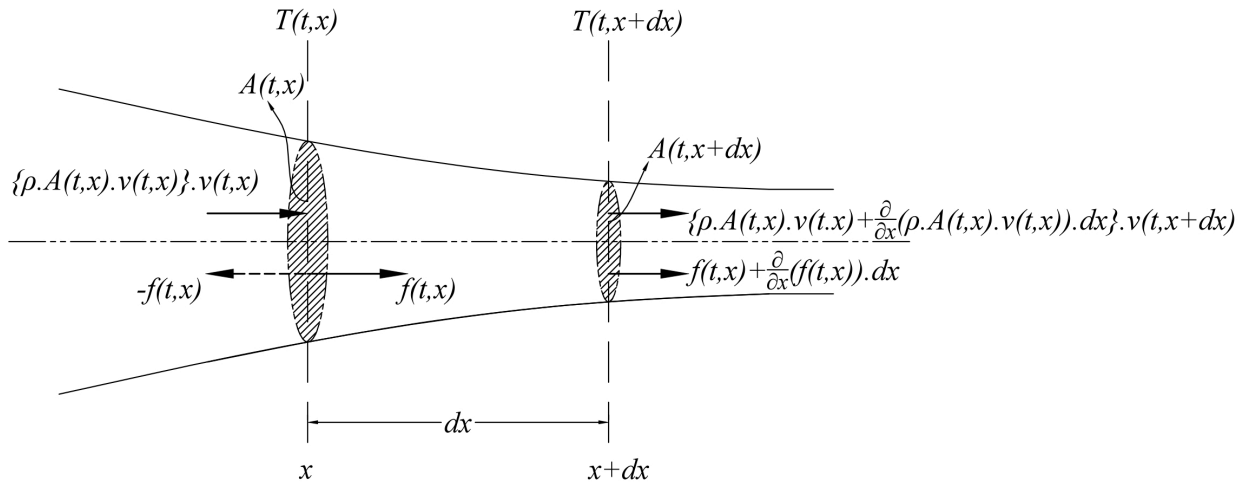
Figure 3.3: Change of the momentum of the control volume between x and x+dx

The heat flow through the cross-sectional area at *(t,x)* by conduction and advection[4] is represented in Figure 3.4 and by the energy balance, Equation 3.11; and it was obtained under the assumption of constant volume deformation and no radial temperature gradient, due to the shape feature of the wire. The heat loss Q_L through the wire surface to the surrounding environment is also shown in Figure 3.4 and it is given as:

$$Q_L(t,x) = 2 \cdot \sqrt{\pi \cdot A(t,x)} \cdot h \cdot (T(t,x) - T_0) \cdot dx \qquad (3.13)$$

Assuming no deformation occurs below softening temperature of the material, cooling transfer coefficient *h* was obtained from the open literature, which is the measured heat transfer coefficient between steel and air at higher temperatures.
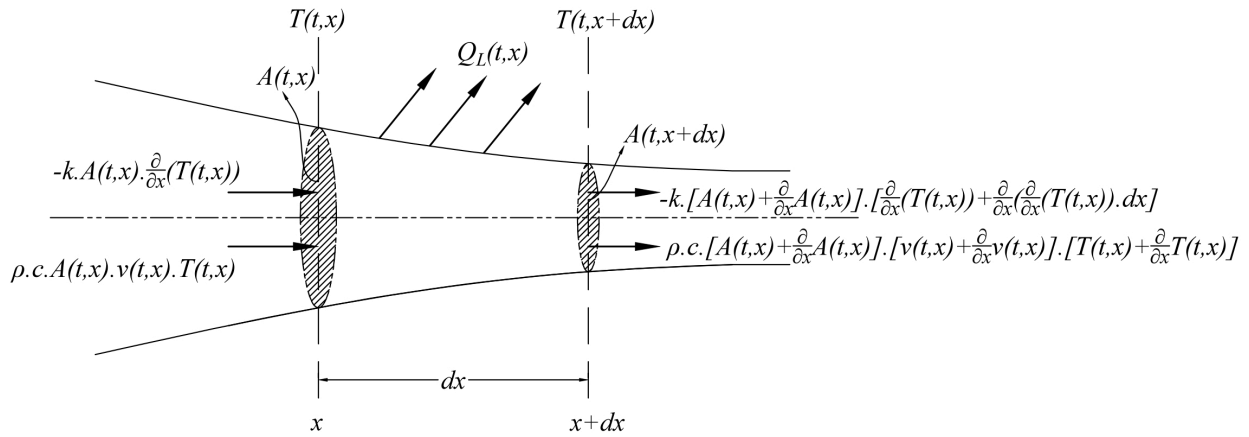
Figure 3.4: Energy balance in the control volume between x and x+dx

It should be noted that investigation of the behavior of the fourth state variable, which is an implicit state variable used in the calculation of the constitutive mode, is beyond the scoop of this study.

---

[4] Advection is a transport mechanism of a substance or conserved property by a fluid due the fluid's bulk motion.

CHAPTER 4

NUMERICAL ANALYSIS

4.1 Chapter overview

The partial differential equations are mathematical descriptions of how the state variables and their derivatives (rates of change) affect each other in a dynamical way. After applying all the assumptions and simplifications mentioned in the previous section (section 3.4), the initial boundary value problem could be outlined by a system of four nonlinear coupled partial differential equations (Equations 3.9-3.12). These PDEs govern the dynamic behavior of the state variables over the space and time domains. Due to complex nature of these equations there is no analytical method to solve them. Thus, numerical methods are utilized to analyze the system behavior. There is a vast variety of numerical analysis methods in literature to solve nonlinear PDEs: FEM, Finite Difference and Finite Volume etc. Due to relative simplicity of the finite difference method and formation of the equations, it has been used in this work.

The idea is to semi-discretize the PDEs using finite difference method and transform them to Ordinary Differential Equations (ODE). Then, the ODEs over the discretized domain are solved simultaneously to obtain the solution for state variables.

In this work, the PDEs are discretized over space domain. After discretization, ODEs in time domain are formed which can be solved more readily than PDEs. A detailed description of the methodology has been discussed in the following section.

4.2 Discretization in space and time

Figure 4.1 shows the schematic of a discretized time and space model that was used in this study. The grid spacing was denoted by Δx and Δt for space and time steps respectively.
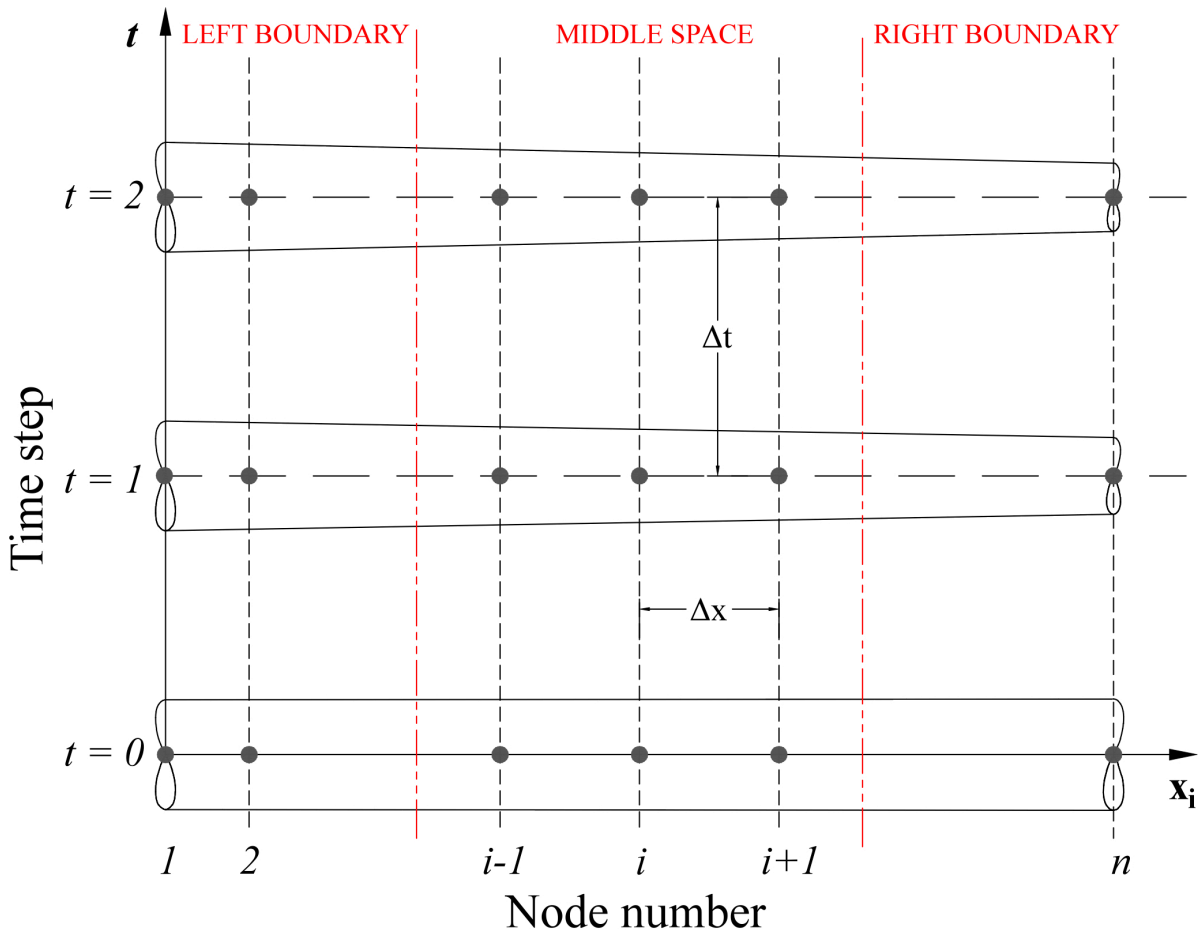

Figure 4.1: Schematic for discretization model (space and time grid)

A discrete analogue of the continuous space has been adopted (Eulerian approach). In a discretization step, there is a finite set of points on which the functions are defined, and the functions value are available on a discrete set of points. The space has been discretized into *n*

points (nodes) along the longitudinal axis while the time axis was divided into 10^5 and 10^6 points (intervals) along the ordinate in order to evaluate the state variables rate of change with respect to time at nodes numerically.

In order to calculate the evolution of the state variables in time, a system of four PDEs has to be solved for each node. Discretizing the space into nodes reduces the PDEs to a set of four ODEs for each node and that can be solved for the state variables. However, the discretized space should be studied under three separate sets of Boundary Conditions (BC); namely left, middle space and right boundaries. The space containing the first and the second nodes form the first region (left boundary) whereas the last node forms the third region (right boundary). All nodes in between are included in the second region (middle space boundary).

Discretization is done using different finite difference methods; namely forward, centered and backward methods. The type of method used depends on the order of derivatives, error order and the region we are discretizing.

4.2.1 Left boundary

The ODEs for the first two nodes have been treated separately. Since there is no node to the left of the first node, Forward Finite Difference (FFD) formula, Equation 4.1, was used to approximate the ODEs.

$$\varphi'(x_i) \approx \frac{-\varphi_{i+2} + 4\varphi_{i+1} - 3\varphi_i}{2\Delta x} \qquad\qquad (4.1)$$

where $\varphi_i = \varphi(x_i)$; φ represent any of the state variables and x_i is the location of *ith* node on the space grid. Furthermore, because of the physics of the drawing process as well as the stability concerns, FFD equations were utilized in order to describe the behavior of process parameter at the second node.

On the other hand, in the die-less drawing the process parameters at the beginning of the deformation zone (first node) are constant and pre-defined for a specific draw practice. Therefore, their rate of change with respect to time is zero, i.e. $\dfrac{d\varphi(x)}{dt} = 0$. Hence, the boundary conditions for the first node at all time remain the same as represented in Equation 4.2.

$$\frac{\Delta A(t,0)}{\Delta t} = \frac{\Delta v(t,0)}{\Delta t} = \frac{\Delta T(t,0)}{\Delta t} = \frac{\Delta \sigma_e(t,0)}{\Delta t} = 0 \tag{4.2}$$

4.2.2 Middle space boundary

The centered finite difference (CFD) approximation, Equation 4.3 was employed to calculate system of equations for the middle space boundary numerically.

$$\varphi'(x_i) \approx \frac{\varphi_{i+1} - \varphi_{i-1}}{2\Delta x} \tag{4.3}$$

The values of the state variables at any node in the middle space are evaluated with respect to their next and previous nodes state. In order to determine the profiles for state variables along time, Equations 4.4-4.7 have been solved simultaneously for time step sizes as fine as 0.000001.

$$\frac{\Delta A}{\Delta t} = -\left(A_i \cdot \frac{v_{i+1} - v_{i-1}}{2\Delta x} + v_i \cdot \frac{A_{i+1} - A_{i-1}}{2\Delta x} \right) \tag{4.4}$$

$$\frac{\Delta v}{\Delta t} = -v_i \cdot \left(\frac{v_{i+1} - v_{i-1}}{2\Delta x} \right) + \frac{\sigma_i}{\rho \cdot A_i} \cdot \left(\frac{A_{i+1} - A_{i-1}}{2\Delta x} \right) + \frac{1}{\rho} \cdot \left(\frac{\sigma_{i+1} - \sigma_{i-1}}{2\Delta x} \right) \tag{4.5}$$

$$\frac{\Delta T}{\Delta t} = \frac{k}{\rho \cdot c_i} \cdot \left(\frac{(T_{i+1} - T_{i-1}) \cdot (A_{i+1} - A_{i-1})}{4\Delta x^2 \cdot A_i} + \frac{T_{i+1} - 2T_i + T_{i-1}}{\Delta x^2} \right) - v_i \cdot \left(\frac{T_{i+1} - T_{i-1}}{2\Delta x} \right) - \frac{2h\sqrt{\pi}}{\rho \cdot c_i} \cdot \frac{T_i - T_0}{\sqrt{A_i}} \tag{4.6}$$

$$\frac{\Delta \sigma_e}{\Delta t} = \theta_i \cdot \left(\frac{v_{i+1} - v_{i-1}}{2\Delta x} \right) \cdot \left[1 - \frac{\tanh\left(\kappa \frac{(\sigma_e)_i}{(\sigma_{eS})_i} \right)}{\tanh(\kappa)} \right] \tag{4.7}$$

where A, v, T and σ_e are cross-sectional area, drawing velocity, temperature of the wire and mechanical threshold stress respectively. ρ, c and k are representing density, specific heat coefficient and thermal conductivity of the wire respectively. θ is a temperature dependent stage II hardening rate, κ is a "best-fit" constant and index i denotes the node number.

4.2.3 Right boundary

The last node forms the right boundary and since there is no node to its right, the backward finite difference (BFD) formula, Equation 4.8 has been employed in order to approximate the ODEs of the third region.

$$\varphi'(x_i) \approx \frac{3\varphi_i - 4\varphi_{i-1} + \varphi_{i-2}}{2\Delta x} \tag{4.8}$$

The velocity at the right boundary is held fix in order to achieve the desired cross-sectional area, while cross-sectional area, temperature and mechanical threshold stress at the last node (right boundary) is yet to be determined from the simulation results. The discretized equations used for the last node are as follows:

$$\frac{\Delta A}{\Delta t} = -\left(A_n \cdot \frac{3v_n - 4v_{n-1} + v_{n-2}}{2\Delta x} + v_n \cdot \frac{3A_n - 4A_{n-1} + A_{n-2}}{2\Delta x} \right) \tag{4.9}$$

$$\frac{\Delta v}{\Delta t} = 0 \tag{4.10}$$

$$\frac{\Delta T}{\Delta t} = \frac{k}{\rho \cdot c_n} \cdot \left(\frac{(T_n - T_{n-1}) \cdot (A_n - A_{n-1})}{\Delta x^2 \cdot A_n} + \frac{T_n - 2T_{n-1} + T_{n-2}}{\Delta x^2} \right) - v_n \cdot \left(\frac{3T_n - 4T_{n-1} + T_{n-2}}{2\Delta x} \right) - \frac{2h\sqrt{\pi}}{\rho \cdot c_n} \cdot \frac{T_n - T_0}{\sqrt{A_n}} \tag{4.11}$$

$$\frac{\Delta\sigma_e}{\Delta t} = \theta_n \cdot \left(\frac{3v_n - 4v_{n-1} + v_{n-2}}{2\Delta x} \right) \cdot \left[1 - \frac{\tanh\left(\kappa \frac{(\sigma_e)_n}{(\sigma_{eS})_n} \right)}{\tanh(\kappa)} \right]$$

(4.12)

4.3 Solution of the ordinary differential equations

The ODEs obtained after discretization governs the behavior of the state variables along time and the solution of ODEs shows how the state variables change with the time. There are four ODEs for each node in the space that has to be solved concurrently, in order to obtain state variable's profiles. Thus, there is a system of *4n* ODEs that should be solved to provide the dynamic behavior of the whole system. However, the solution of ODEs, regardless of the finite difference method employed, requires initial conditions (IC) for each node to be specified. It was assumed that all the state variables are constant at *t =0* except for the velocity, which increases linearly through the space.

The followed system of ODEs are solved by employing MATLAB® solver ode45, ode23, and ode15s. However, since the governing system of equations consisted of stiff differential equations, the solution of the ode45 solver did not converge or took a very long time to solve the system. Hence, ode15s solver was employed to solve the governing system of equations and describe the process in its stable mode. Once the solution for the system of ODEs is obtained, the resulting data can be post processed to analyze the behavior of the corresponding state variables.

4.4 General discussion

The problem has been solved for different deformation zone lengths and number of the nodes to compare the results theoretically. It should be noted that the highest error order in approximating differential terms occurs where heat conduction in the energy equation is computed with second order truncation error *(O(h²))* and thus, for consistency, except for the

equations of the second node, all the finite difference approximation formulas employed in this analysis approximated having the same order of truncation error (2nd order).

From the approximated solutions of the ODEs, the change of each state variable in a pre-defined time span can be plotted for any node by using MATLAB®. In addition, the data obtained from ODE's solutions has been retrieved in order to plot the state variables profiles for different time steps along the longitudinal space. The step-by-step numerical analysis using MATLAB® is shown in a chart format in Figure 4.2.
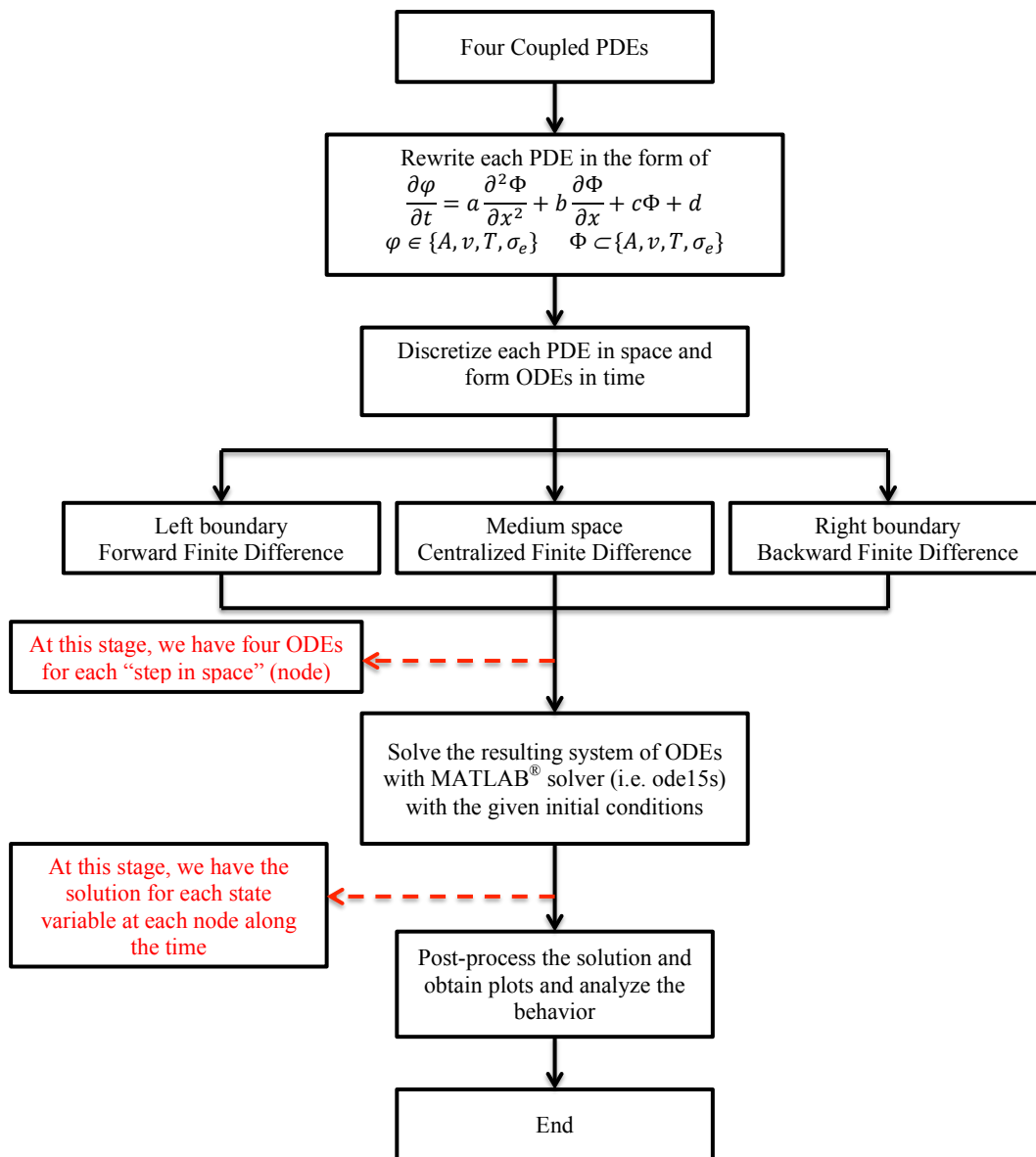

Figure 4.2: The s tep-by-step numerical analysis chart

CHAPTER 5

RESULTS AND DISSCUSIONS

5.1 Chapter overview

The mathematical model presented in the Chapter 3 was used to perform a detailed study on the die-less drawing process. In the previous Chapter, the mathematical model consisted in a numerical analysis involving finite difference approximation methods. In order to examine the validity of the numerical model, the physical properties used in the numerical computation are based on thermo-mechanical properties of HY-100 Steel (Refer to Tables 1 and 2). HY-100 has low carbon contents while its tensile strength (yield strength) is greater than 689 MPa at room temperature. Furthermore, the mechanical threshold stress model was employed to describe the plastic behavior of HY-100. As addressed in section 3.2, the MTS constitutive model requires a temperature dependent shear modulus (Equation 3.1).

In the following sections results of the numerical model simulations are presented for the three main state variables. The parameter configurations used in the simulations are gathered in a table provided in Appendix C.

5.2 Process parameters behavior in the deformation zone

In order to investigate the behavior of the process parameters in the deformation zone, suitable initial conditions for an operational configuration of parameters was employed. For the following analysis a timespan of 0.8 sec with a step size of 10^{-6} was used and a 100 mm deformation zone was divided into 800 equally spaced intervals. The wire was drawn at 200 mm/s and had an initial drawing velocity and an initial cross-sectional area of 40 mm/s and 4 mm^2 respectively. The initial temperature in the analysis was 1195K, which is the softening temperature of HY-100 steel. Figure 5.1 shows the change of the cross-sectional area, the temperature and the velocity with time measured at the last node.[5]
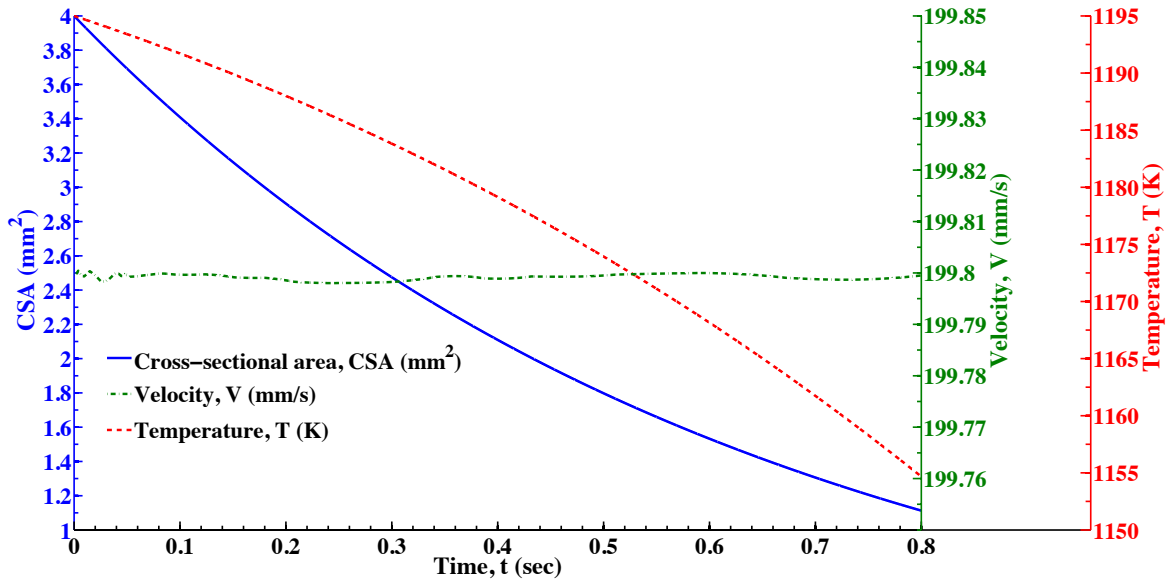
Figure 5.1: Process parameters vs. Time (at the last node)

It is clear that the Cross-Sectional Area (CSA) and temperature are decreasing with increasing time, however as it is shown in Figure 5.1, the CSA tends to decrease exponentially in the nodes while the temperature decrease shows an increasing rate of losing heat to the

---

[5] The velocity is the only state variable that has a pre-defined output value, and thus, it was measured at the node before last node.

55

surrounding. The velocity, as expected, shows a rapid but small fluctuation at the beginning of the process, which is about 0.02 mm/s change in the drawing velocity, and it remains almost steady for the rest of the process.

In order to be able to study the parameters profile in the deformation zone, their change along the longitudinal deformation axis has been provided in the Figure 5.2. However, it should be noted that, since the CSA decreases early and rapidly, the deformation axis of which units have been scaled down and shown at the top of the figure to capture all the process parameters profiles in the Figure 5.2.
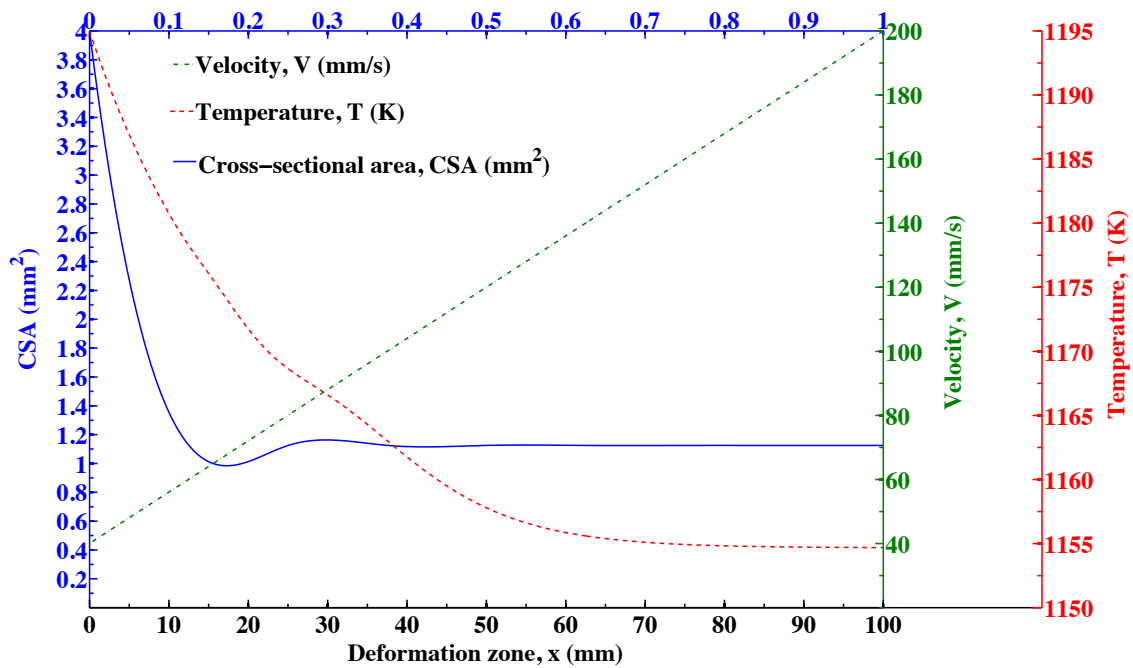
Figure 5.2: Process parameters vs. Deformation zone length (at the last time step)

Figure 5.2 shows that more than 90% of the reduction in the cross-sectional area occurred in less than 1% of the deformation zone, at the beginning of the process that can be explained by the onset of the necking phenomenon.

The slope of the temperature curve decreases continuously, and at about 70% of the deformation zone, reaches a steady value of 1154.7K. The velocity on the other hand, shows a

56

linear relation with the deformation zone length. In the following sections each state variable is investigated separately.

5.2.1 Cross-sectional area

The cross-sectional area profile in the deformation zone shows that the reduction in area mostly occurs at the beginning of the deformation zone. In the Figure 5.3 the change of cross-sectional area of all nodes has been plotted against the deformation zone length for 20 equally spaced time steps. However, since the main reduction occurs at the beginning of the deformation zone, the plot has been magnified.
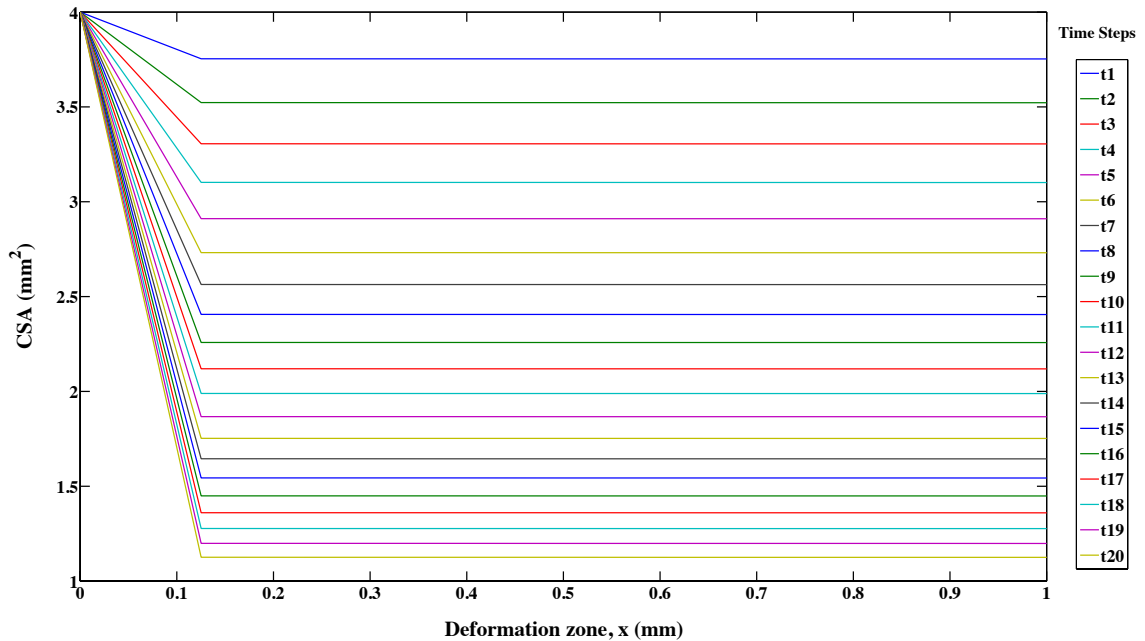
Figure 5.3: Change of cross-sectional area along the space for different time steps

Although most of the reduction in cross-sectional area occurs at the beginning of the deformation zone, it is happening gradually throughout the time of the deformation, which is evident by comparing the cross section profile of different time steps in Figure 5.3. Above all, it shows that the necking phenomena are occurring along the wire length at the same time and not at a single location. Figure 5.4 is a simple schematic of the deformed wire in the deformation

57

zone, which illustrates the sudden reduction in area of all nodes along wire longitudinal axis at the same time.
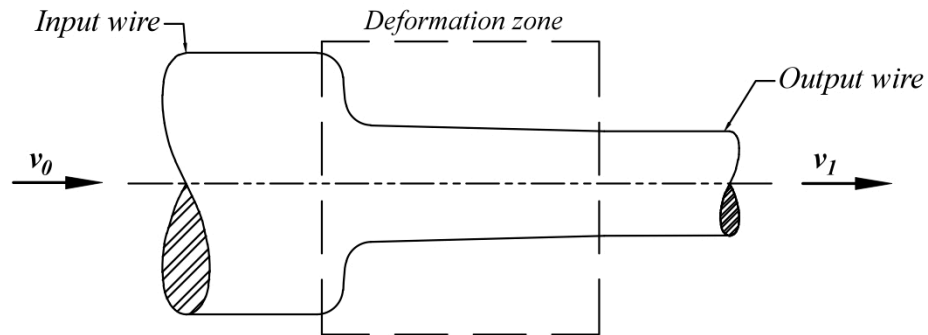
Figure 5.4: Schematic of the deformed wire in the deformation zone

The curve-fitting tool of the MATLAB® software has been utilized to find and analyze the curve that best models the cross-sectional area deformation profile. The cross-sectional area data points have been fitted into various fitting curves that were compared at the level of the adequacy of their fit. Among all of them, the exponential fit and the smoothing spline fit were better at describing the cross-sectional area reduction along space. In the Figure 5.5 the data from the 10th time step has been fitted into an exponential curve as well as a smoothing spline curve with smoothing parameter *p =0.9994*[6].

---

[6] As the smoothing parameter *p* changes from 0 to 1, the smoothing spline changes, correspondingly, from one extreme, the least squares straight-line approximation to the data, to the other extreme, the "natural" cubic spline interpolant to the data.
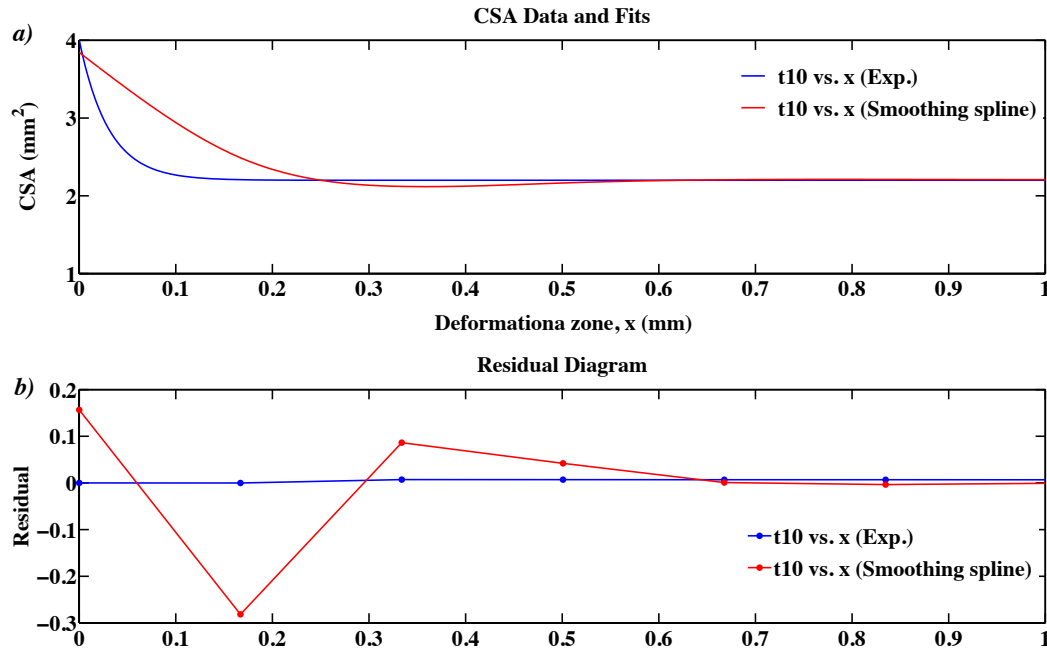
Figure 5.5: a) Fitted curves into CSA data points for the 10th time step. b) Residual plot of the fitted curves

The smoothing spline and the exponential fitted-curves are shown in Figure 5.5 diagram (*a*). They could model the reduction in area similarly after the main reduction in cross-sectional area occurred. Although the exponential fit had a coefficient of determination R^2 closer to one in comparison to the smoothed spline[7], by visually comparing the adequacy of the fits from their residuals in Figure 5.5 diagram (*b*), it can be realized that the smoothing spline fit could describe the reduction in cross-sectional area better than the exponential fit since its residuals appeared to behave more randomly.

In order to help in clearly noticing the changes in CSA with time, only a few of the node reduction profiles are shown in the Figure 5.6. It is obvious that the CSA of the first node remains unchanged during the process. Also, since most of the deformation occurs at the very

---

[7] The coefficients of determination R^2 of the smoothed spline fit and the exponential fit are 0.9993 and 0.9652 respectively.

beginning of the deformation zone, there is a huge difference between the reduction profiles of the first several nodes and the rest of them.

a)

b)

Enlarged section
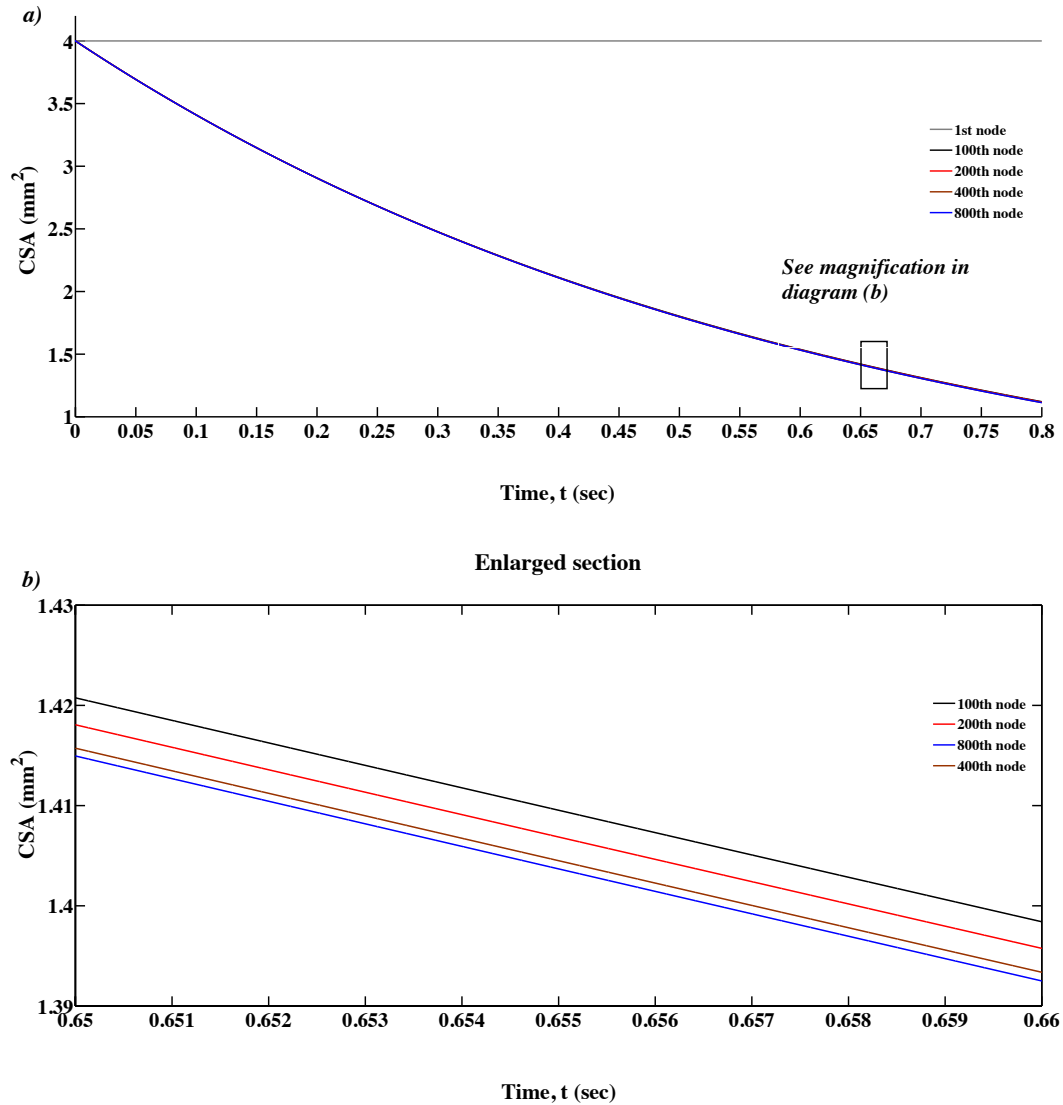
Figure 5.6 a) Change of CSA in nodes along time b) Magnified section of diagram a

The part of the curve delimited by a rectangle in part (*a*) of Figure 5.6, is presented at higher resolution in Figure 5.6 part (*b*). The reductions in the cross-sectional area with time for four nodes are shown. The reduction in area increases by little from one node to the following one. For instance, the difference in the reduction of cross-sectional area between the 100th and the 200th node curves in the Figure 5.6 part (*b*) is less than 0.001 mm^2. This difference is even

lower between the nodes close to the end of the deformation zone since less deformation occurs there.

5.2.2 Temperature

The heat loss by the natural convection in the deformation zone is responsible for most of the temperature drop during the deformation. Figure 5.7 illustrates the temperature decrease along the longitudinal axis of deformation for the same time steps chosen in the previous section (5.2.1).

Figure 5.7: Change of temperature along the space in different time steps

Since the time steps are equally spaced, Figure 5.7 indicates that the temperature drop in the wire is increases as the process reaches its end, i.e. the heat loss increases with time along the space. Moreover, the temperature drop curves for all time steps are showing that the temperature decreases faster as the process continues.
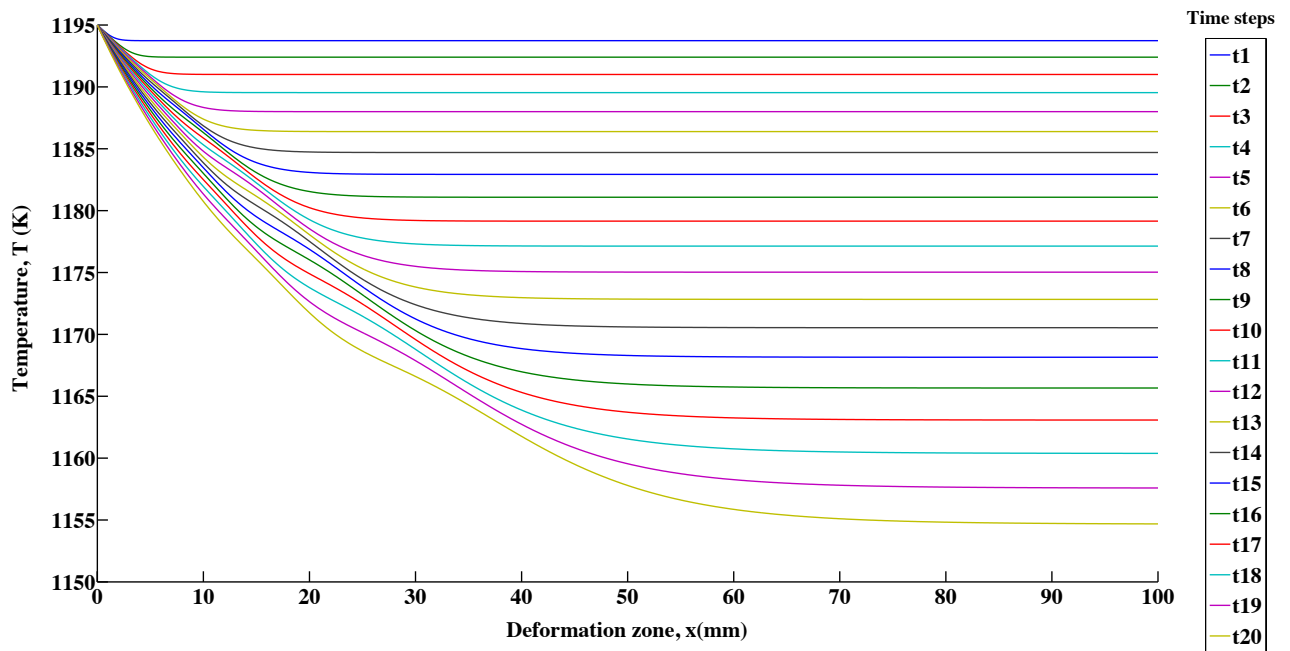
The temperature data points were used to compare the best curve fits that could model the temperature behavior in the deformation zone. Figure 5.8 demonstrates an exponential as well as a smoothing spline fits to temperature data point of the 10th time step in diagram (*a*).
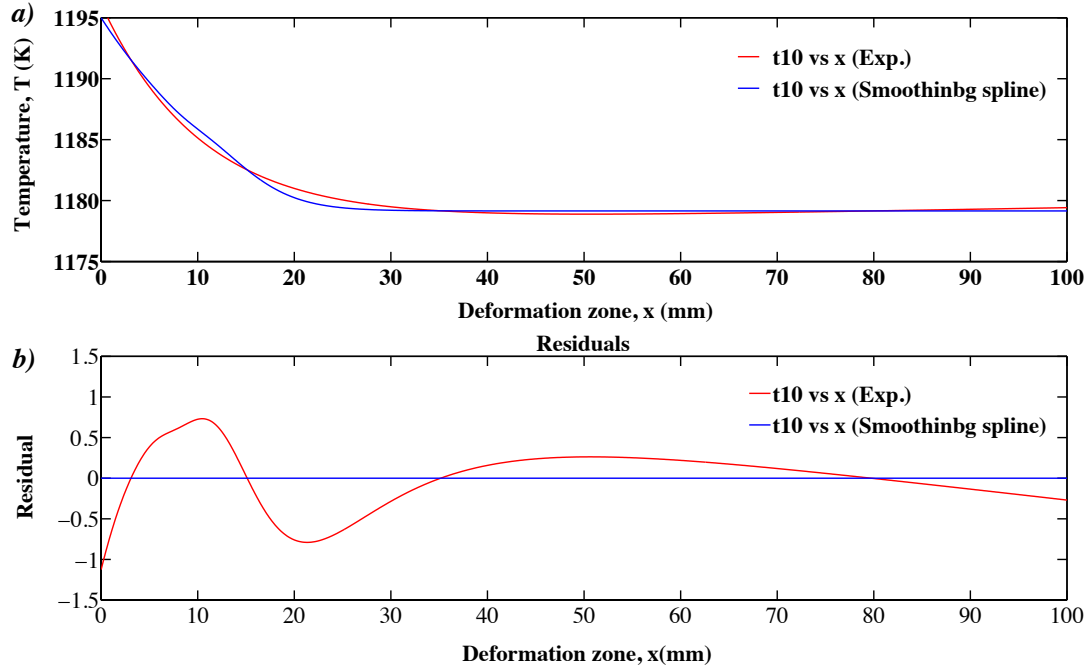
Figure 5.8: a) Fitted curves into temperature data points of the 10th time step b) Residual plot of fitted curves

The plots of the Figure 5.8 suggest that both fits describe the temperature behavior similarly. Although the smoothing spline fits the data points almost exactly with a smoothing parameter *p = 0.9997*, but comparing the adequacy of the fits reveals that the smoothing spline fit's residual clearly follows some patterns (oscillate about zero axis), which makes it not a good model for the temperature. The exponential fit residual, on the other hand, shows more random behavior as it can be seen in diagram (*b*) of Figure 5.7.

The temperature profiles of several nodes are plotted along time in the Figure 5.9. It is evident from the following figure that temperature drops faster at the end of the deformation zone. For example, the temperature of the 300th node drops to 1174K in 62.5% of the total time, while it takes 85% of total time for 200th node to reaches the same temperature.
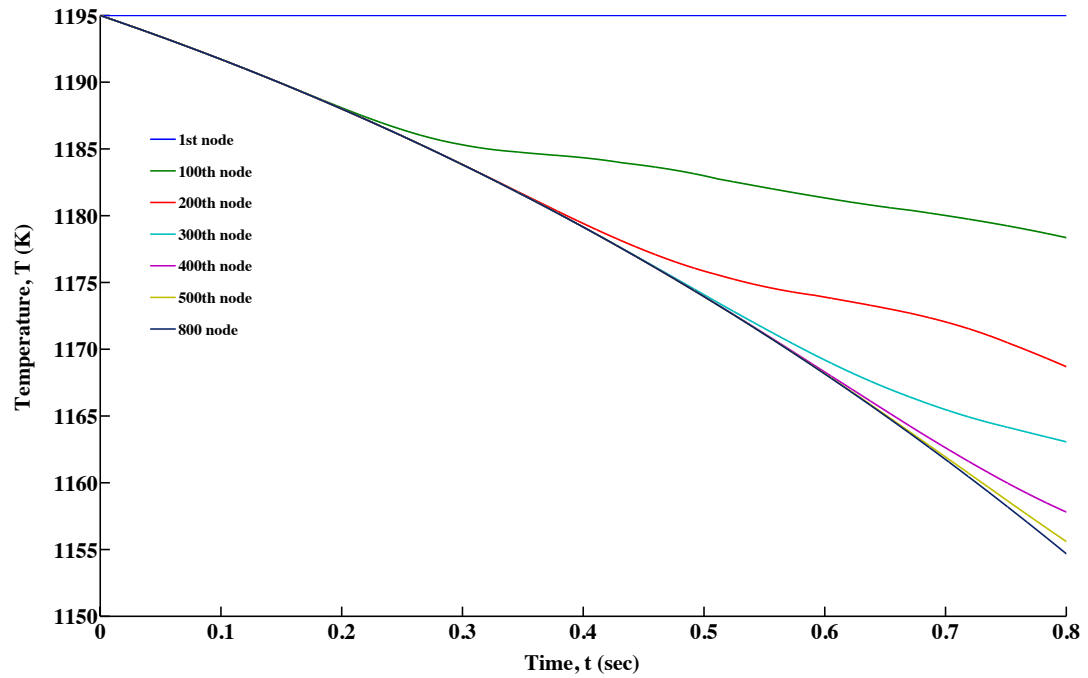
Figure 5.9: Change of temperature in nodes along time

5.2.3 Drawing velocity

Drawing velocity is the only state variable in the simulation of the process that has a pre-defined initial profile, by which the final CSA is to be controlled. It is clear from Figure 5.10 that the velocity maintains its initial profile in the deformation zone throughout the process.
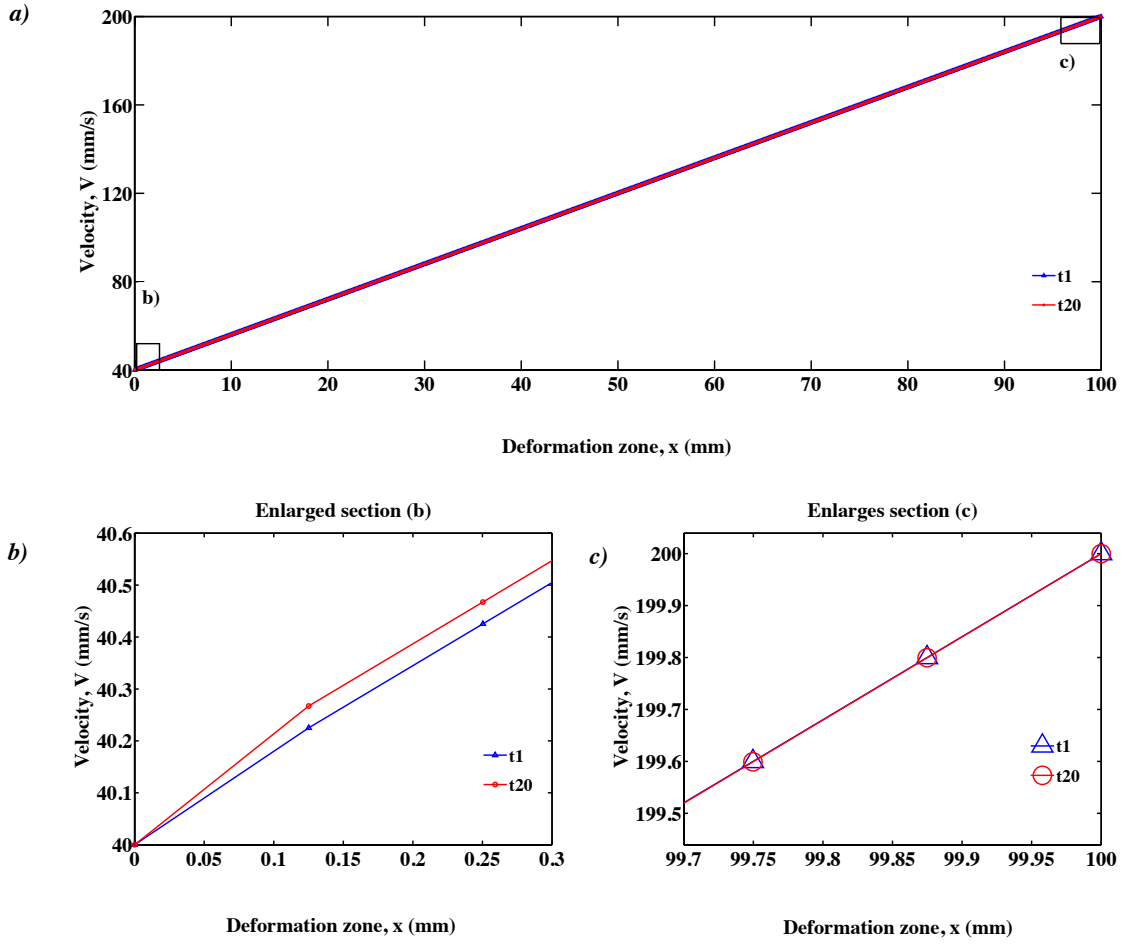
Figure 5.10: a) Change of drawing velocity along the space in the first and last time steps b) Enlarged section (b) in diagram (a) c) Enlarged section (c) in diagram (a)

Diagram (*a*) in Figure 5.10 shows the velocity profile for the first (*t1*) and the last (*t20*) time steps, which are almost identical. Diagram (*b*) and (*c*) are the enlarged sections of the diagram (*a*), and they are marked by (b) and (c) in the diagram (*a*), respectively. The diagrams of the Figure 5.10 suggest that the velocity in the deformation area is only increasing at the very beginning of the deformation zone (diagram *b*); this is in accordance with the necking phenomenon at the beginning of the process. However, the velocity is decaying gradually and is almost identical to its initial velocity profile at the end of the deformation zone (diagram *c*).

5.3 Effect of process parameters on the reduction in cross-sectional area

In order to analyze the behavior of the main process parameters and to study how they affect each other, the MATLAB® code has been executed many times for various parameter configurations (Appendix C). Their results were recorded in excel and are compared here. This section focuses on the influence of the deformation length and the total time on the reduction in area.

5.3.1 Reduction in area vs. Drawing Velocity

As it is understood from the conservation of mass principal, the reduction in area increases as the drawing velocity increases. The plots in Figure 5.11 part (*a*) illustrate the increase in the percentage Reduction in Area (%RA) with respect to the drawing velocity for two pre-defined deformation lengths, namely 100 mm and 200 mm. It was calculated from Figure 5.11 part (*a*) that doubling the deformation zone length would reduce the %RA up to 55.02 percent (compared at 120 mm/s) and 46.36 percent in average.

The relation between the change in the %RA and the drawing velocity can be modeled with an exponential function. Figure 5.11 diagram (*b*) is the residual plot of the exponential fittings. The randomly distributed data in the residual plot explains that the exponential curves could model the relation between the %RA and the drawing velocity reasonably accurate.
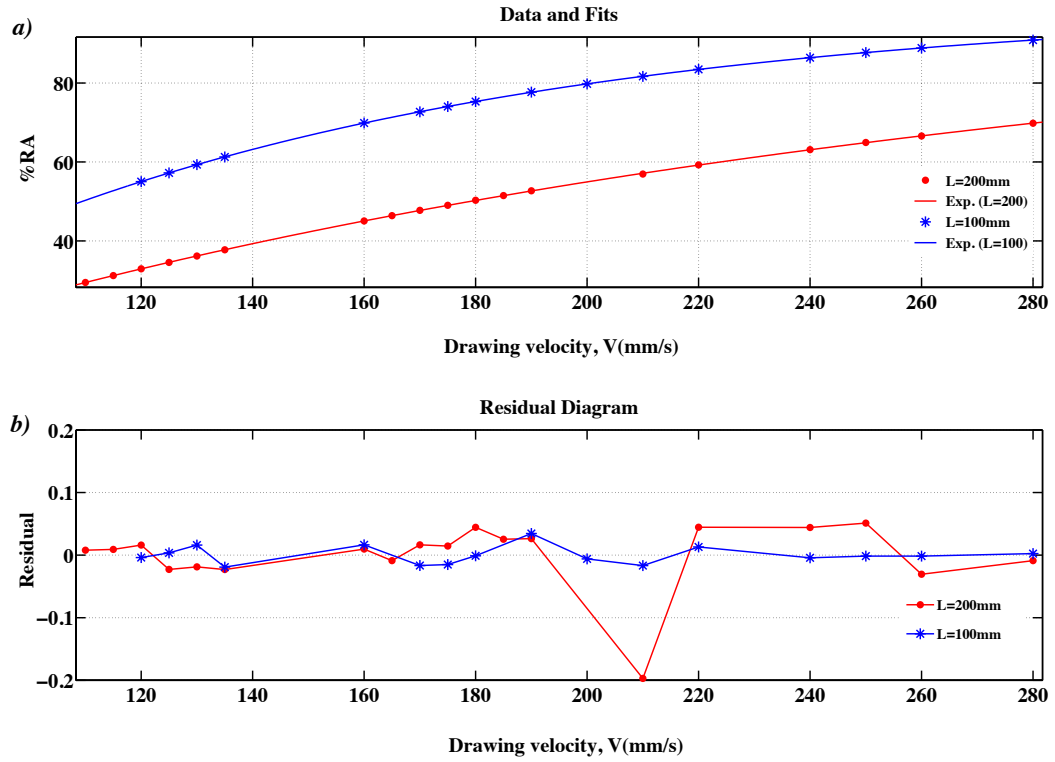
Figure 5.11: a) %RA vs. drawing velocity for different deformation lengths (400 nodes, dt=10^{5}s, t=1s) b) Residual of fits

Considering the division length *dx* instead of the deformation length, similar results can be concluded: reducing the step size increases the %RA. For instance, decreasing *dx* by half (from 0.5 mm to 0.25 mm) increases the %RA by 32.44 percent on average.

Not only does increasing the total time of the process increases the percentage reduction in area, but also it stretches the range of velocities, where the process is executable, by 25 percent. Figure 5.12 shows the change in %RA with respect to the drawing velocity for two different total times of 0.5 sec and 1 sec.
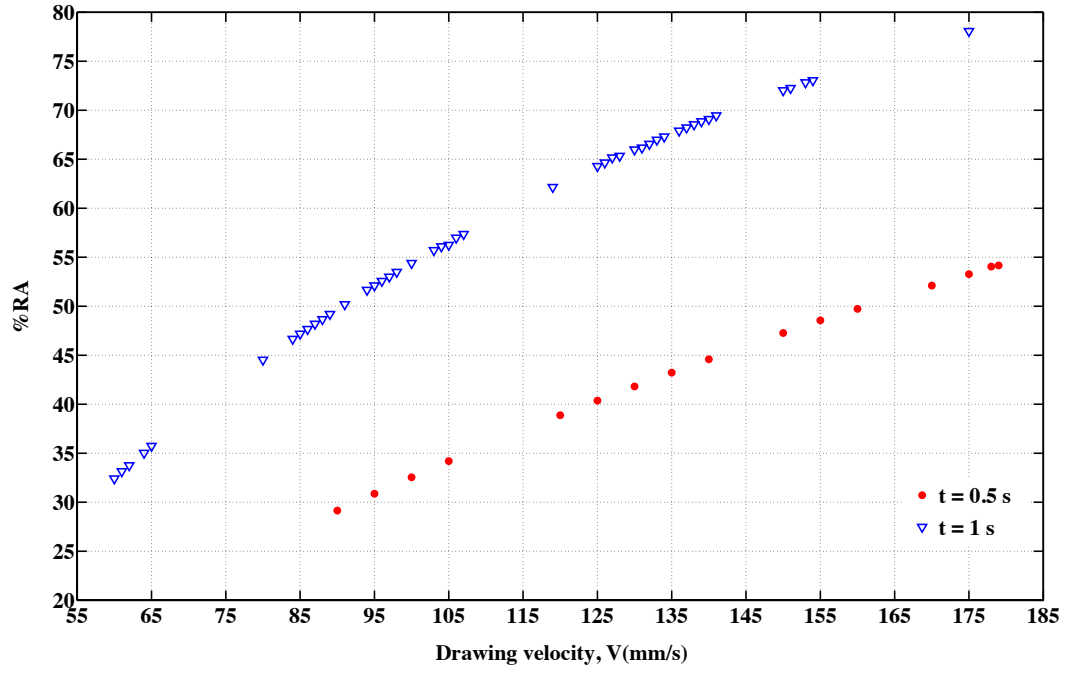
Figure 5.12: %RA vs. drawing velocity for t=0.5s and t=1s(L=100mm, 200 nodes, dt=10⁵s, Vᵢₙ=20mm/s)

It is evident from Figure 5.12 that increasing the total time will increase the %RA for a specific configuration of parameters. For instance, the results from a smaller *dx* (Figure 5.12) shows that by increasing the total time from 0.5 sec to 1 sec, the average increase in the reduction in area is 53.40 percent.
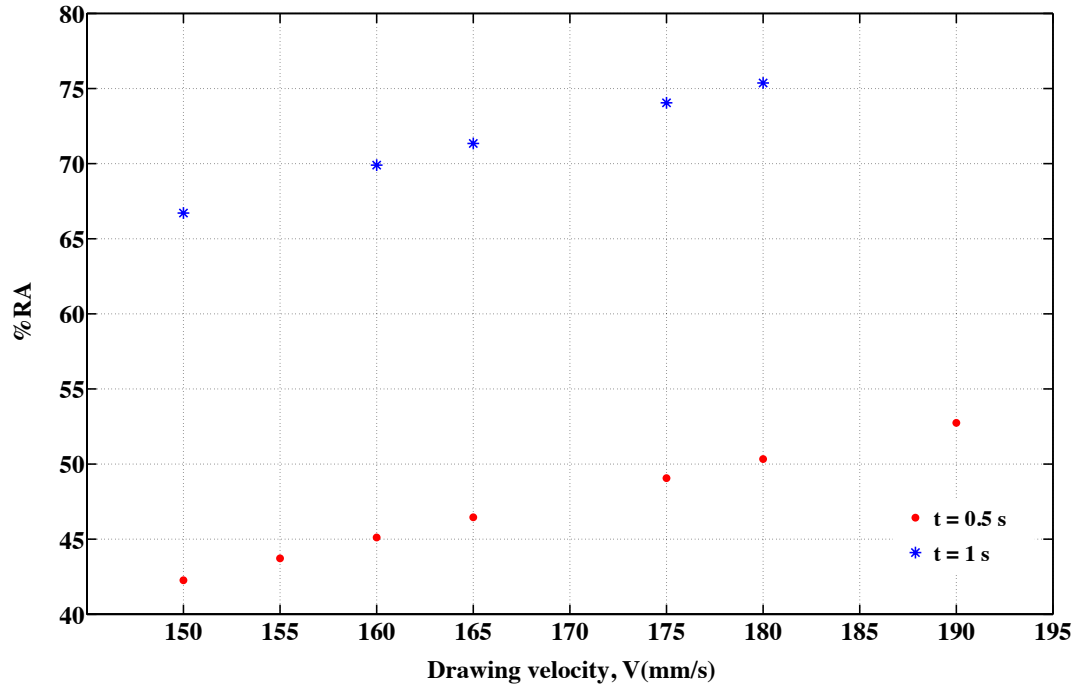
Figure 5.13: %RA vs. drawing velocity for t=0.5s and t=1s (L=100mm, 600nodes, dt=10⁵s, V_{in}=40mm/s)

The exponential curve could model the relation between the %RA and the drawing velocity fairly accurate at *t = 1s* as is shown is Figure 5.14 part (*a*). The residual plot in the diagram (*b*) of Figure 5.14 confirms that the exponential fit is a good choice to describe the %RA and drawing velocity relation.
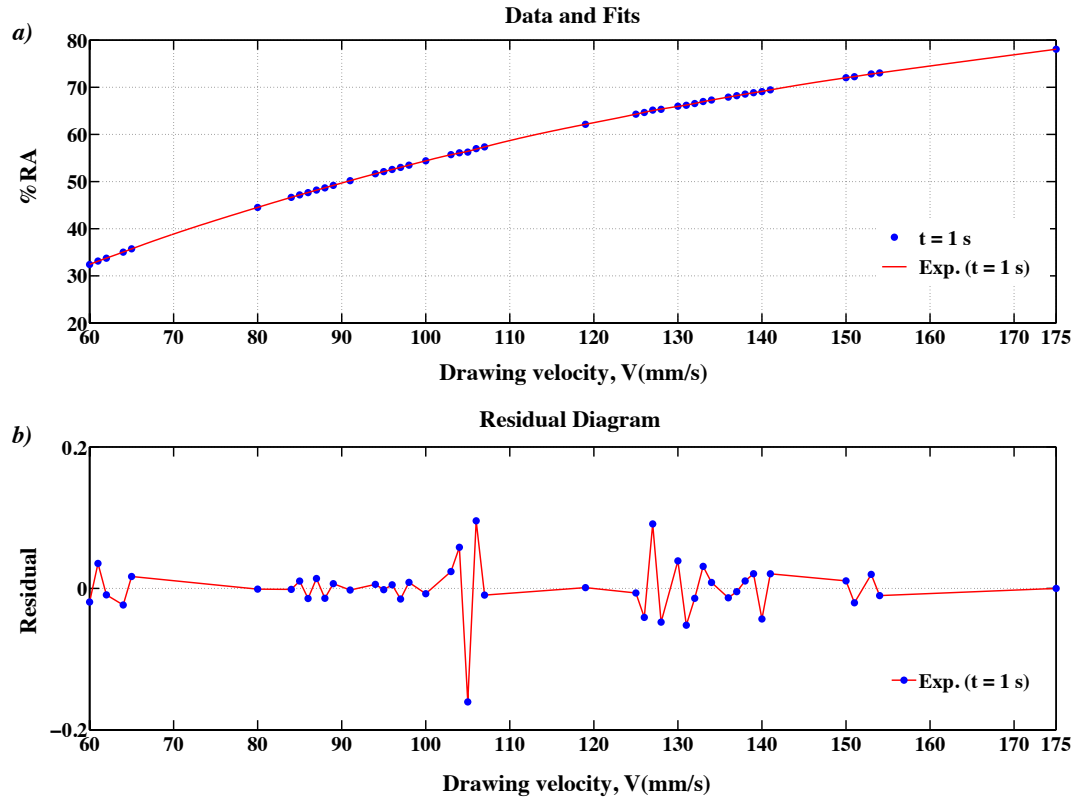
Figure 5.14: %RA vs. drawing velocity at t=1s (L=100mm, 200 nodes, dt=10^{-5}s, V$_{in}$=20mm/s)

5.3.2 Reduction in area vs. Deformation length

In order to understand the influence of the deformation length on the maximum achievable reduction in area, the %RA was plotted against the deformation zone length for various drawing velocities. The percentage reduction in area decreases with increasing deformation length as illustrated in Figure 5.15 for several drawing velocities.
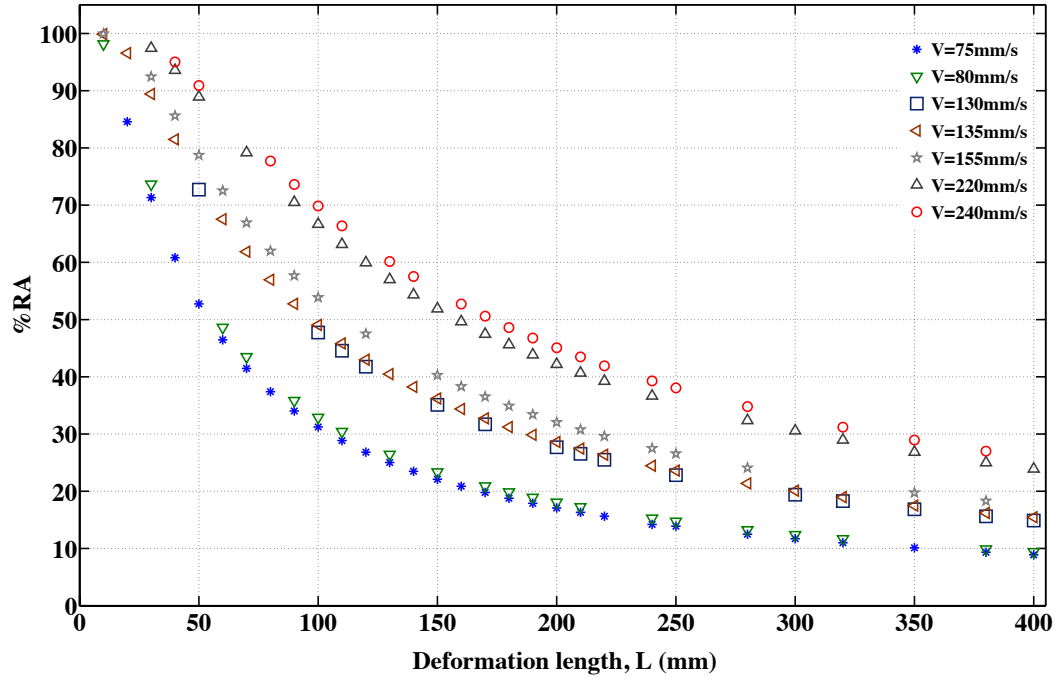
Figure 5.15: %RA vs. deformation length at different drawing velocities (400 nodes, t= 0.5s)

It should be also noted that higher drawing velocities have yielded in greater reductions in area. The relation between the %RA and the deformation length were modeled in Figure 5.16 diagram (*a*) by exponential regression trendlines and their residuals are plotted in diagram (*b*).
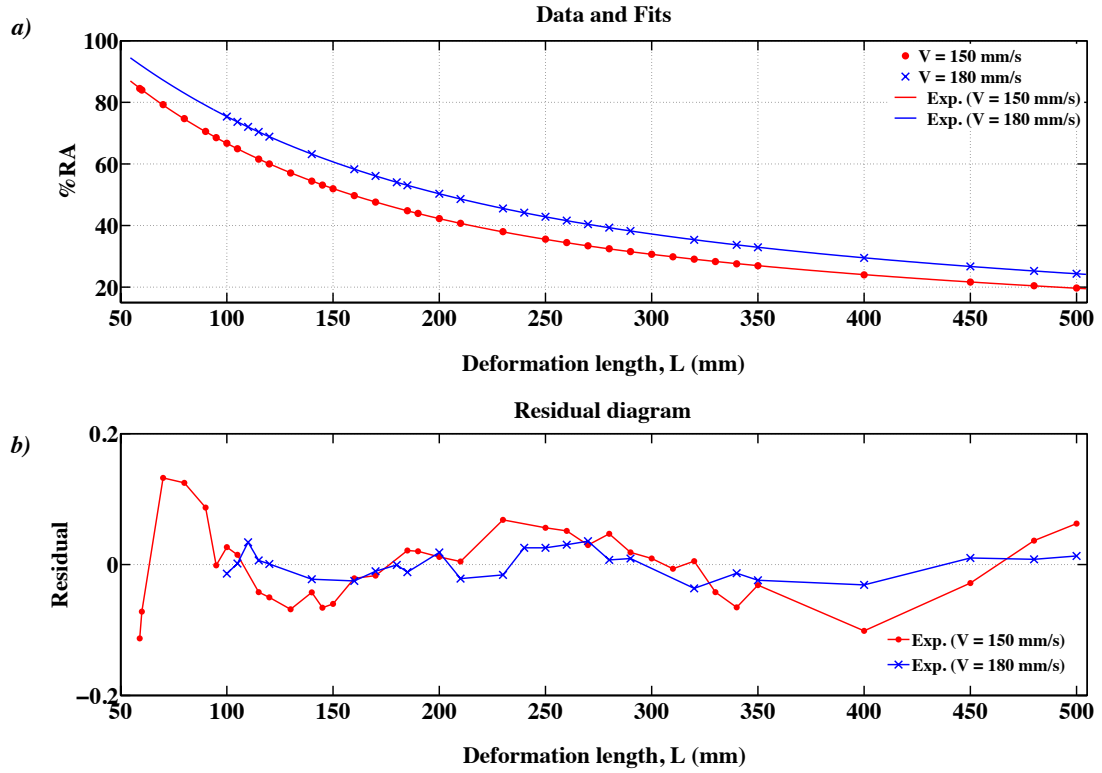
Figure 5.16: a) %RA vs. deformation length at V_{out}=150mm/s and V_{out}=180mm/s (600 nodes, t=1s) b) Residual plots of fitted curves

From Figure 5.16, a 10 mm/s increase in the drawing velocity will increase the %RA by 4.84% approximately. For instance, increasing the drawing velocity from 150 mm/s to 190 mm/s will increase the %RA achievable up to 27.60% (measured at L=280 mm) and 23.77% on average.

Increasing the total time from 0.5s to 1s, increases the *%RA* for a particular deformation length, and also extends the range of deformation lengths that the process is practical by 42.85% as it can be seen in the Figure 5.17 diagram (*a*).

a)

b)
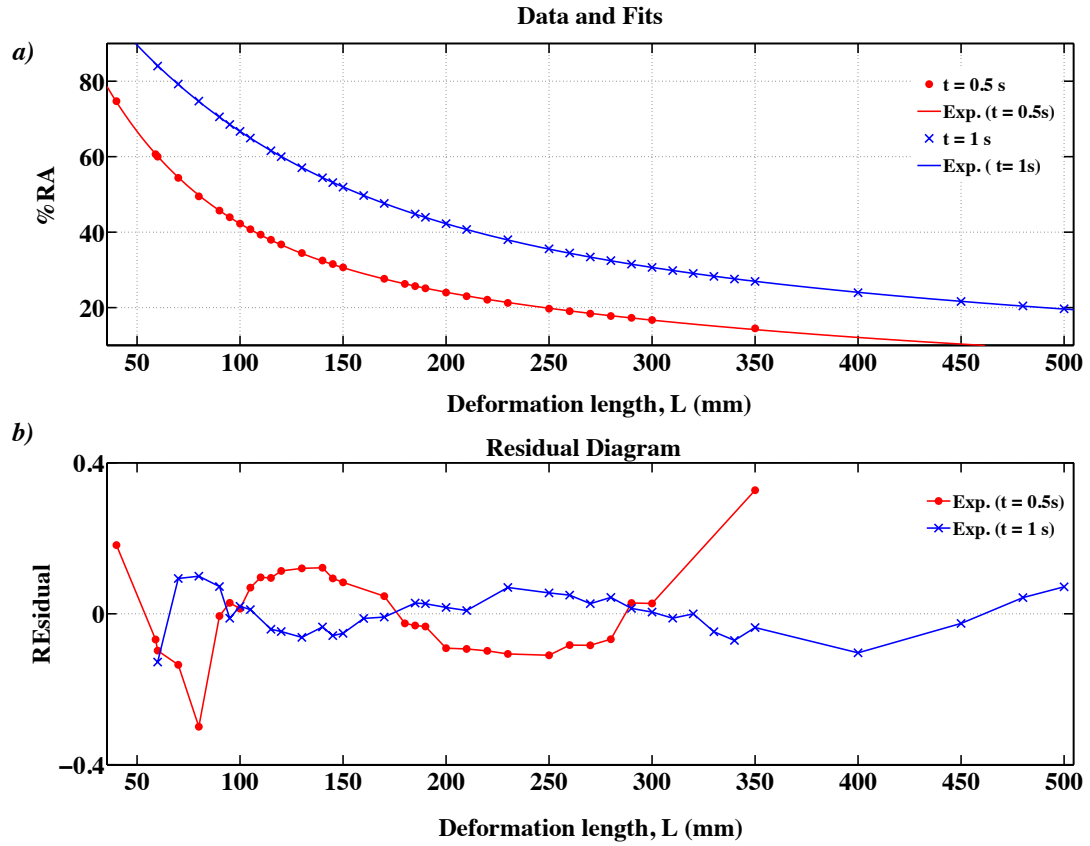
Figure 5.17 a) %RA vs. deformation length at t=0.5s and t=1s (600 nodes, V$_{out}$=150mm/s) b) Residual plots of exponential fitted curves in the diagram a

The residuals of the exponential fitted curves in the diagram (*b*) of Figure 5.17 appear to be randomly scattered, and thus, they can model the relation between %RA and the deformation length to an acceptable extent.

The overlapping data of Figure 5.18 show that initial velocity does not affect the %RA very much. However, the higher the initial velocity the higher final drawing velocity will be achieved.
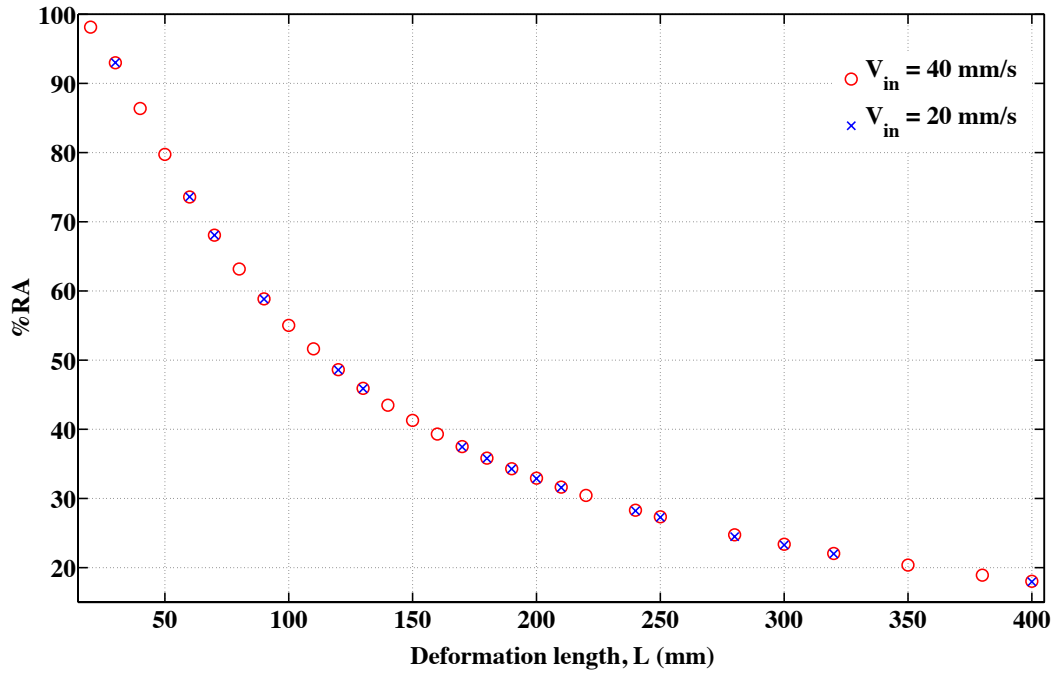
Figure 5.18: %RA vs. dx at V_{in}=40mnm/s and V_{in}=20mm/s (400 nodes, t =1s, V =80mm/s)

Finally, a chart of *%RA* versus *dx* for various velocities and parameter configuration can be found elsewhere in Appendix D.

5.4 Effect of the mathematical modeling on the process parameters

In the simulation of the die-less drawing process different technics of discretization and semi discretization have been tried and the most stable one was employed. This section investigates and compares the order of the finite difference equation used in the discretization of the governing equations, the time and the space step size effects on the process.

Following figures indicate that both the 1st and 2nd order forward finite difference methods produce similar curves. Figure 5.19 illustrates the increase in %RA with increasing drawing velocity for the 1st and 2nd FD methods.
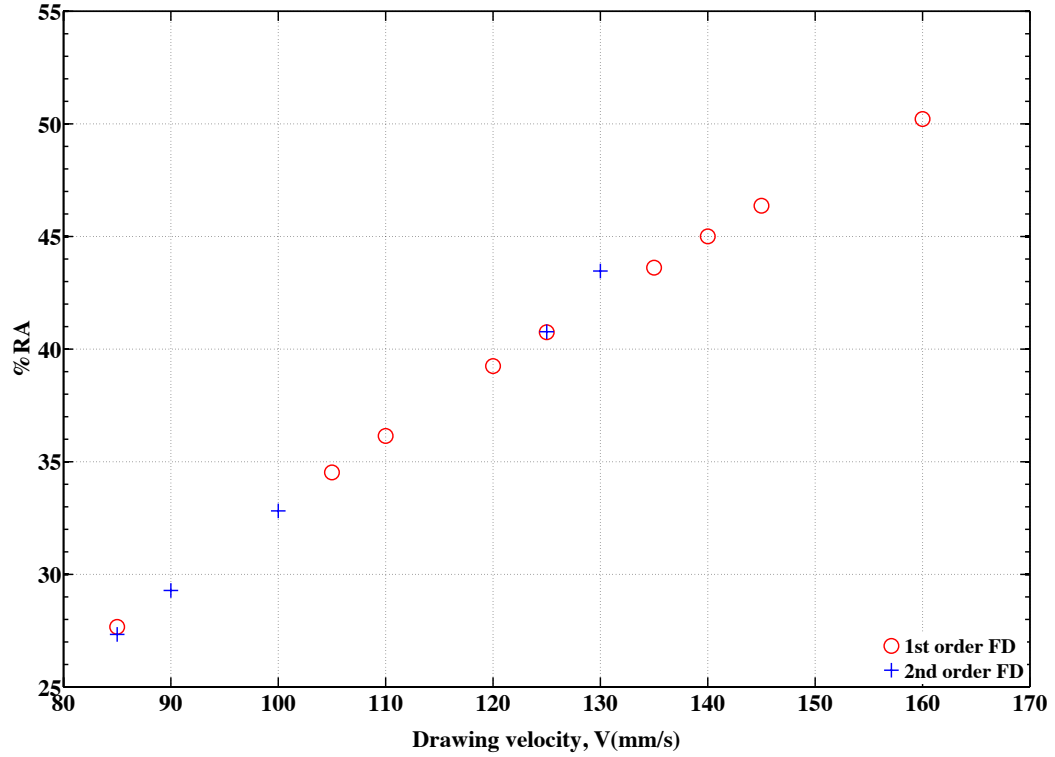
Figure 5.19: %RA vs. drawing velocity for 1st and 2nd order FD (L=200mm, #400 nodes, dt=10^{-6}s, t=1s)

As it can be seen from Figure 5.19 simulations with the 1st order FD could be accomplished upon a wider range of velocities. However, both of the 1st and 2nd order FD approximate the %RA and velocity relation alike. Furthermore, by comparing the percentage reduction in area (%RA) versus the deformation length, L (Figure 5.20) provided by the 1st and the 2nd order FD, it can be concluded that both of the 1st and the 2nd order finite difference approximation method outcomes are similar and very close to each other. However, since simulation involving the 2nd order approximation require significantly more computing power and thus take much longer to yield results, mostly the 1st ordr FD equations have been utilized in order to analyse the effect of deformation length and velocity on the reduction in area for different parameter configurations.

74
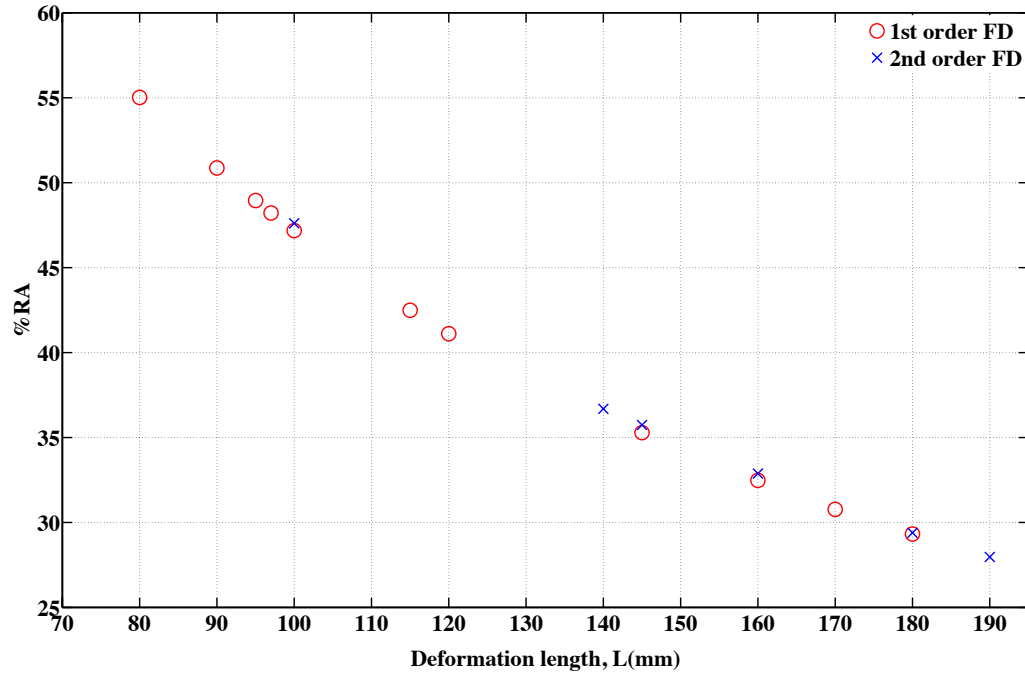
Figure 5.20: %RA vs. deformation length for the I^{st} order and 2nd order FD (V=85mm/s, #200 nodes, dt =10^{-5}s, t=1s)

There are small discrepancies between the 1st and 2nd order FD data points at smaller deformation zone, but as the deformation zone length increases the data from 1st and the 2nd order FD overlap each other as it is shown in figure above.

The governing system of equations have been solved numerically for various configurations of the parameters, but, in the process of collecting data it was realized that using the time step size of 10^{-6} in the simulation, not only extremely slows the simulation process down, but it is also almost as accurate as using the step size of 10^{-5}, which can be simulated much more faster. Figure 5.21 is a plot of percentage reduction in area versus velocity for two time step sizes mentioned above.
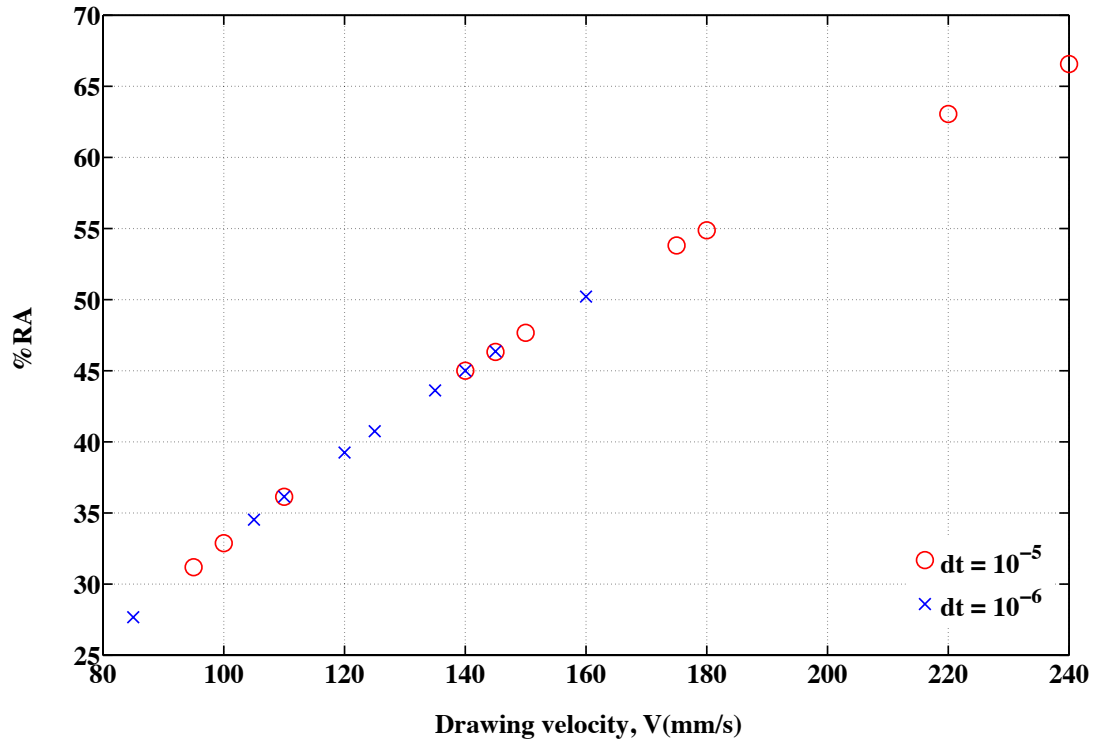
Figure 5.21: The time step size comparison diagram (L=200mm, #400 nodes, dt=1s)

On the other hand, comparing the %RA along velocity for 400 and 600 nodes shows that increasing the number of the nodes by 50% does not affect the outputs by more than 0.01%. However, as it can be seen in the Figure 5.22, increasing the number of the nodes will shrink the range of velocities with which the process was successfully completed. For instance, the configuration of parameters with 400 nodes could be completed in a range between 160 mm/s and 240 mm/s, while the same configuration with 600 nodes could be only executed (replicated) in a smaller range between 150 mm/s and 195 mm/s.
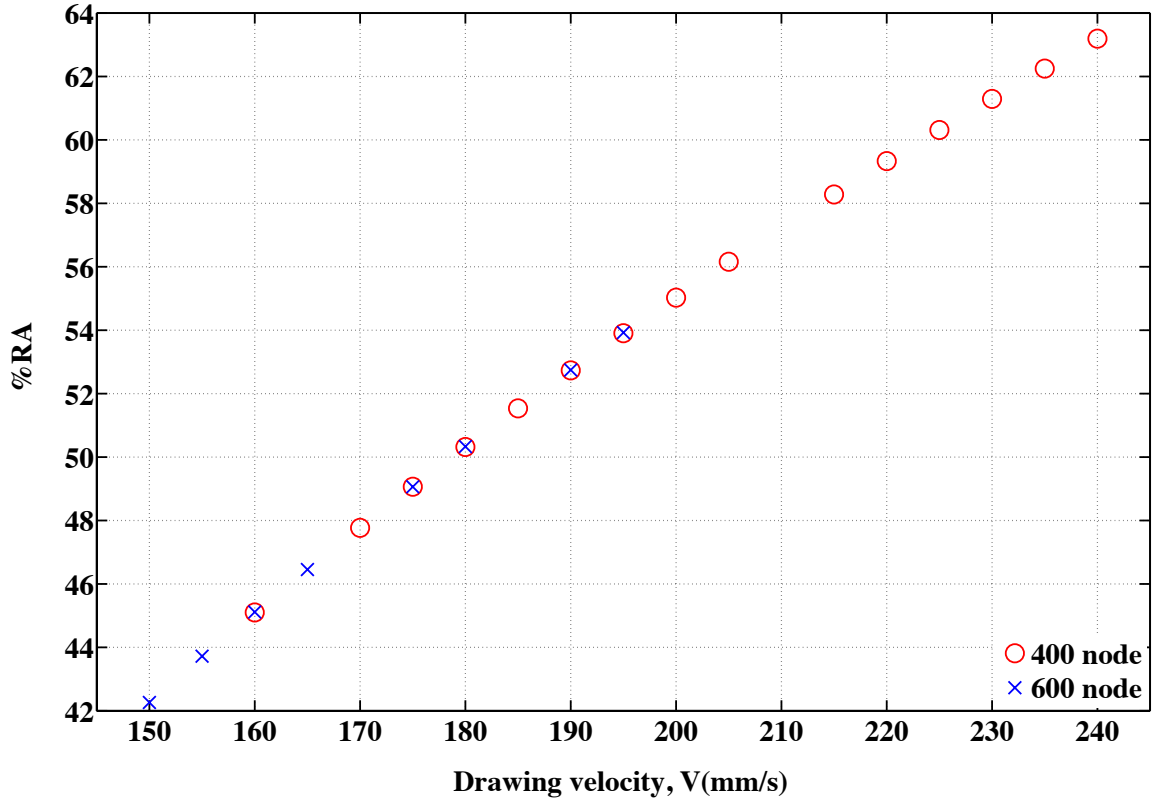
Figure 5.22: %RA vs. drawing velocity for 400 and 600 nodes (L=100 mm, dt=10^{-5}s, t= 0.5s, V_{in}= 40 mm/s)

In addition, the changes of the final CSA against velocity for different number of nodes are gathered in Table 3. The empty cells in the table indicate the failed test trial. According to Table 3, the simulation could be successfully completed at the drawing velocity equal to 195 mm/s regardless of the number of the nodes.

Table 3: Cross-sectional area change with velocity for different number of nodes

L =100mm, dt =10^{-5},Total time= 0.5sec, A1= 4mm^2, V1= 40mm/s				
Velocity (mm/s)	Final CSA (mm^2)			
	#200	#400	#600	#800
150	2.3117	-	2.3095	-
155	2.2547	-	2.2511	-
160	2.1993	2.196	2.1954	-
165	2.1452	-	2.1418	-
170	2.0924	2.0893	-	-
175	2.0409	2.0374	2.0375	-

L =100mm, dt =10^{-5},Total time= 0.5sec, A1= 4mm^2, V1= 40mm/s				
Velocity (mm/s)	Final CSA (mm^2)			
	#200	#400	#600	#800
180	1.991	1.9873	1.9867	-
185	1.9418	1.9386	-	1.9382
190	-	1.8906	1.8902	1.8897
195	1.8411	1.8438	1.843	1.843
200	1.8029	1.7989	-	-
205	1.7596	1.7536	-	1.7532
210	-	-	-	1.7103
215	1.6729	1.6688	-	-
220	-	1.6267	-	1.6267
225	-	1.5875	-	-
230	-	1.5483	-	-
235	-	1.51	-	-
240	-	1.4723	-	-

5.5 Working limits

Working limits of the simulations are defined as the maximum and minimum deformation lengths, at a particular drawing velocity, when the resulting cross-sectional area reduction between 10 and 90 percent is considered stable and acceptable. At each particular drawing velocity under study, the process is simulated for deformation length from as short as 10 mm up to 420 mm, where increasing the deformation length further causes the resulting reduction in cross-sectional area to lay out of the acceptable range. The working limits for drawing velocities ranging from 60 mm/s to 200 mm/s, with 10 mm/s increments, are illustrated in Figure 5.23.
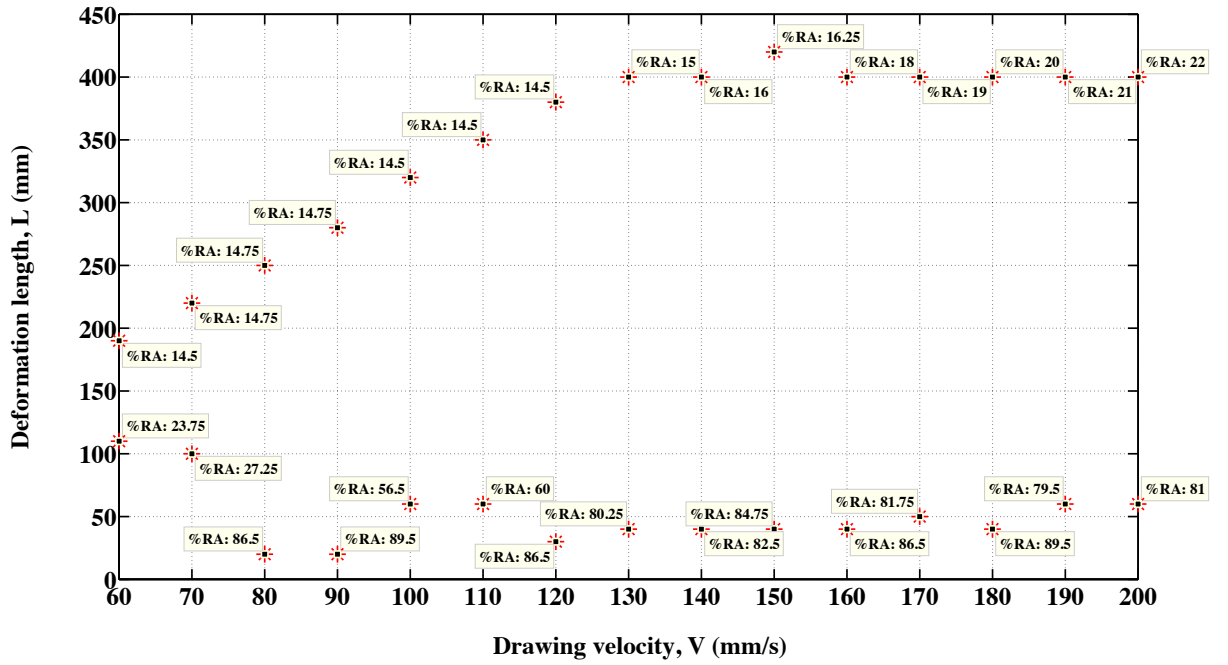
Figure 5.23: Working limits of the die-less drawing process simulations (400 nodes, Total time= 0.5 s, dt =10^6, A_{in}=4mm^2, V_{in}=40mm/s)

Figure 5.23 shows the maximum and minimum deformation lengths and the cross-sectional area reduction achieved at the working limits for the drawing velocities under investigation. As the drawing velocity increases from 60 mm/s to 130 mm/s, the maximum deformation length increases while the cross-sectional area reduction achieved is nearly constant *(%RA ≈ 14.50)*. The maximum deformation length remains almost unchanged *(L_{max}≈ 400 mm)* as the velocity increases, however, the cross-sectional area reduction is increasing gradually to reaches a value of 22% at *V=200* mm/s

On the other hand, as the drawing velocity increases from 60 mm/s, as shown in the Figure 5.23, the minimum deformation length decreases from 110 mm to about 20 mm. As soon as the drawing velocity reaches 100 mm/s, the minimum deformation length increases to 50 mm and remain close to 50 mm for higher velocities. Although the reduction in cross-sectional area is not remarkable (about 25 percent) at lower drawing velocities, but as the drawing velocity passes 80 mm/s the reduction in cross-sectional area rises to about 85 percent and change up to

±5 percent at higher drawing velocities. The maximum acceptable reduction in cross-sectional area reached in the process is 89.5 percent at drawing velocities of 90 mm/s and 180 mm/s.

CHAPTER 6

CONCLUSIONS

6.1 Chapter overview

This research study focused on investigating and characterizing the process of die-less wiredrawing by considering the thermal and mechanical aspects of the process. The mathematical model introduced in Chapter 3 is used to describe the thermo-mechanical behavior of the process parameters. The mathematical model was numerically simulated by utilizing MATLAB® software in Chapter 4. From the results of the numerical model, the behavior of the main state variables, namely the cross-sectional area, velocity and temperature in the deformation zone were investigated. The results of the numerical simulations are gathered in Chapter 5 and are discussed in this chapter.

Dynamic behavior of the die-less wiredrawing process was described by four partial differential equations (Equations 3.9-3.12), i.e. continuity equation, momentum equation, energy equation and a strain hardening equation.

6.2 Process parameter behavior

In the process of analyzing the behavior of the cross-sectional area (See section 5.2.1), it was concluded that 90% of the deformation occurs in less than 1% of the pre-defined deformation zone length. However, since the heated material (wire) is continuously fed into the deformation zone, the necking phenomenon does not occur at a single location, namely at the beginning of the deformation zone. Instead, the cross-sectional area of the total length of wire in the deformation zone will be reduced at a same time, as it can be seen in different time steps of Figure 5.3. This behavior can be related to the fact that the total length of wire in the deformation zone (before deformation starts) has the same temperature, and therefore same strength; thus, as soon as the drawing velocity increases, the material (wire) in the deformation zone will be subjected to the same level of stress. Furthermore, the cross-sectional area fitted curves suggest that smoothing spline fits the CSA data point better than the exponential fits (Figure 5.5), however, since the smoothing spline fitting curves use spline function that is piece-wise defined, i.e. it is not defined outside of the deformation zone under investigation, it is concluded that the cross-sectional area profile is best described by an exponential fit that has the form of Equation 5.1 as:

$$f(x) = a_1 \cdot \exp(b_1 \cdot x) + a_2 \cdot \exp(b_2 \cdot x) \qquad (6.1)$$

where a_1, a_2, b_1 and b_2 are fitting constants.

During the deformation process the temperature of the wire drops from 1195 K to 1154.7 K, which is only about 3% decrease in the temperature. Despite the small temperature drop however, it is one of the main mechanism that helps the heated material (wire) to recover its strength and allows the wire to be further deformed. Hence, it is concluded that the process of die-less drawing is highly temperature sensitive as Eynatten [10] also suggested previously. Similar to CSA, temperature data points can be best fit to an exponential curve (Equation 5.1) as

the smoothing spline fit can not predict the temperature outside the deformation zone. Moreover, it was concluded that the temperature drops faster at the end of the deformation zone (Figure 5.9), which is due to smaller cross-sectional area (less heat carrying mass), and the longer exposure time of the material at the end of the deformation zone to the surroundings.

6.3 Cross-sectional area reduction

One of the main objectives of the die-less wiredrawing process is to achieve greater reductions in cross-sectional area in one pass of operation compared to the conventional wiredrawing process, while reducing the cost of production. Theoretically, the maximum achievable reduction in the cross-sectional area by the conventional wiredrawing process is 63% (See Appendix A), but in practice only about half of this value can be achieved safely in one pass of the operation. Die-less wiredrawing process, on the other hand, has the potential to achieve greater reductions in the cross-sectional area by replacing the expensive tool (die) in the conventional wiredrawing with a contact free Heating-Cooling unit.

In order to investigate the effect of process parameters (section 5.3) and mathematical modeling of the process (section 5.4) on the cross-sectional area in the deformation zone, the reduction in the cross-sectional area of the wire, Equation 1.1, was plotted against the drawing velocity of the wire or the deformation zone length.

It can be concluded from Figure 5.11 part (*a*) that doubling the deformation zone length will reduce the achievable *%RA* up to 55.02% (measured at *V* = 120 mm/s) and 46.36% on average (*V* = 110 to 280 mm/s). Doubling the total time of the process on the other hand, increases the achievable reduction in area by 53.40% on average (Figure 5.13). It should be also noted that increasing the total time of the process would widen the range of velocities where the process is executable (Figure 5.12).

Furthermore, it is concluded that the relation between the *%RA* and the drawing velocity of the wire can be best described by an the exponential function of the form of Equation 6.1 with the constants a_1 and b_1 having positive, and a_2 and b_2 having negative values.

By comparing the curves of Figure 5.16 diagram (*a*), it was concluded that a 10mm/s increase in the drawing velocity would increase the *RA* by about 5%, i.e. increasing the drawing velocity from 150mm/s to 180mm/s would increase the achievable *RA* by 15% (measured at $L = 280$ mm) and 23.77% on average ($L = 50$ to 500 mm). Similarly, increasing the total time of the process from 0.5s to 1s, would increases the *%RA* for a particular deformation length, and also extends the range of deformation lengths that the process is practical by 42.85% (measured at $V=150$mm/s) as it can be seen in the Figure 5.17 diagram (*a*).

Moreover, from the residual plots of Figures 5.16 and 5.17, it is concluded that the exponential fitted curves are "best-fit" to describe the relation between the reduction in area (*RA*) and the deformation length (*L*). The exponential function of Equation 6.1 can also be used to describe the *%RA* vs. *L* relation. However, it should be noted that constants a_1 and a_2 are positive while b_1 and b_2 are negative in Equation 6.1.

From the investigation of the mathematical modeling parameter effects on the die-less wiredrawing (See section 5.4), it was realized that simulations with the 1st order FD could be accomplished upon a wider range of velocities and deformation lengths compared to 2nd order FD, as it can be seen from Figures 5.19 and 5.20. However, both of them could approximate the *%RA* relations alike and their outcomes were very close to each other. In addition, from Figures 5.21 and 5.22, it was concluded that the time and space step sizes do not affect the output of the simulations by more than 0.01%, but increasing the number of the nodes (i.e. smaller space step size) would shrink the range of the velocities with which the process was successfully completed.

At last, the working limits defined as: the maximum and minimum deformation lengths, at a particular drawing velocity, when the resulting cross-sectional area reduction between 10 and 90 percent is considered acceptable, is presented in Figure 5.23. The working limits diagram (Figure 5.23) can be used to identify the deformation zone length needed for a steady state deformation at the desired drawing velocity (production rate). For instance, at $V = 80$ mm/s, steady state deformation results in %66 reduction in area, which can be achieved with $L = 35$ mm. Figure 5.23 can also be used to identify the drawing velocity when there is a limitation on the deformation zone length.

6.4 Discussions and limitations

The process of die-less drawing consists of a mechanical process (plastic deformation) and a thermally activated process (heat transfer), which have to be considered together in the analysis. This study was conducted in order to investigate the thermo-mechanical behavior of the die-less drawing process in its transient (unsteady) state. Although there have been similar investigations reported previously, but they are either decoupled thermo-mechanical investigations [13, 47], or they are couple thermo-mechanical while they were investigated only in their steady state [24, 31, 36].

However, since only the deformation zone (and not the heating and cooling zone) was considered in this study, it is limited to the transient state and cannot be used to describe the process in its steady state. In order to investigate and develop the process into its steady state the heating and cooling zone effects should be added in the calculations of future studies.

6.5 Conclusions

From the results of this study, it is concluded that the most important parameter in controlling the RA in transition from unsteady to steady state is the deformation zone length L, in

that, for a pre-defined drawing velocity, there is a specific deformation zone length by which the process can move to its steady state. Furthermore, as the drawing velocity increases, the deformation zone length for steady state deformation increases.

The initial drawing velocity was pre-defined to be linearly increasing in the deformation zone (section 5.2.3). However, introducing a non-linear initial profile for the drawing velocity of the form of a "Sigmoid"[8] function to the system did not change the final drawing velocity profile. That is the drawing velocity, regardless of its given initial profile, will increase linearly to converge to the final velocity. From Figure 5.10 it is concluded that the drawing velocity maintains its linearity throughout the deformation zone, i.e. it deviates from the initial profile and increases at the very beginning of the deformation zone, but it decays gradually and eventually overlaps the initial velocity profile at the end of the deformation zone.

6.6 Future work

Although the only material used in this study was HY-100 steel, the mathematical model of the die-less drawing process provided in this study has the potential to describe the behavior of any high-strength material undergoing deformation at high temperatures. That can be easily accommodated by changing the process and material parameters in the modeling of the process to suit the material characteristics. Furthermore, the constitutive model (MTS model) employed in the modeling of this research can be replaced with any other temperature and strain-rate dependent constitutive model accompanied by a structure evolution, in order to investigate their effect on the outcomes of the process. In addition, including the heating and cooling zone in the analysis of the process can further develop this study. Finally, a properly designed control

---

[8] The Sigmoid function that was used has the form: $f(x) = \dfrac{x}{1+x}$

system for the process along with the dynamic behavior of the process provided in this study can be utilized to design and fabricate a continuous die-less drawing machine in order to investigate the process further experimentally.

REFERENCES

[1] Backofen, W A, I R Turner, and D H Avery. "Superplasticity in an Al-Zn alloy." *A.S.M. Transaction Quarterly* 57 (1964): 980-990.

[2] Banerjee, Biswajit . "An evaluation of plastic flow stress models for the simulation of high-temperature and high-strain-rate deformation of metals." *ArXiv:cond-mat/0512466*, December 2005.

[3] Banerjee, Biswajit. "The Mechanical Threshold Stress model for various tempers of 4340 steel." *arXiv:cond-mat 0510330*, 2005: 1-39.

[4] Banerjee, Biswajit. "The Mechanical Threshold Stress model for various tempers of AISI 4340 steel." *International Journal of Solids and Structures* 44 (2007): 834-859.

[5] Barnes, A J. "Superplastic Forming 40 Years and Still Growing." *Journal of Materials Engineering and Performance* 16, no. 4 (2007): 440-454.

[6] Bochvar, A A, and Z A Sviderskaia. "Superplasticity phenomena in Zinc-Aluminum alloys." *Izv Aked Nauk SSSR, otdel tekh nauk* 9 (1945): 821.

[7] Carolan, Ronan, and Peter Tiernan. "Computer controlled system for dieless drawing of tool steel bar." *Journal of Materials Processing Technology* 209 (2009): 3335-3342.

[8] Chen, S R, and G T Gray. "Constitutive behavior of tantalum and tantalum-tungsten alloys." *Metallurgical and Materials Transactions A* 27A (1996): 2994–3006.

[9] Estrin, Y, and H Mecking. "A unified phenomenological description of workhardeningand creep based on one-parameter models." *Acta Metallurgica* 32, no. 1 (1984): 57-70.

[10] Eynatten, K von. "Dieless Drawing, Ein Massiveunformverfahren Zur Flexiblen Einstellung Von Form, Gefuge und Mechanischen Eigenschaften Von Langprodukten." *Die Eidgenössische Technische Hochschule Zürich*, 2004.

[11] F, W Clinard, and O D Sherby. "Strength of iron during allotropic transformation." *Acta Metallurgica* 12, no. 8 (1963): 911-919.

[12] Follansbee, P S, and U F Kocks. "A constitutive description of the deformation of copper based on the use of the mechanical threshold stress as an internal state variable." *Acta Metal* 36 (1988): 81-93.

[13] Fortunier, R, H Sassoulas, and F Montheillet. "A Thermomechanical Analysis of Stability in Dieless WireDrawing." *International Journal of Mechanical Sciences*, 1997: 615-627.

[14] Furushima, T, and K Manabe. "Experimental and numerical study on deformation behavior in dieless drawing process of superplastic microtubes." *Journal of Materials Processing Technology* 191 (2007): 59-63.

[15] Furushima, Tsuyoshi, and Ken ichi Manabe. "Experimental study on multi-pass dieless drawing process of superplastic Zn-22%Al alloy microtubes." *Journal of Materials Processing Technology* 187-188 (2007): 59-63.

[16] Furushima, Tsuyoshi, and Ken ichi Manabe. "Finite Element Simulation with Coupled Thermo-Mechanical Analysis of Superplastic Dieless Tube Drawing Considering Strain Rate Sensitivity." *Materials Transactions* 50 (2009): 161-166.

[17] Furushima, Tsuyoshi, Syuhei Hirose, and Ken ichi Manabe. "Effective temperature distribution and drawing speed control for stable dieless drawing process of metal tubes." *Journal of Solid Mechanics and Materials Engineering* 3, no. 2 (2009): 236-246.

[18] Furushima, Tsuyoshi, Takashi Sakai, and Kenichi Manabe. "Finite Element Modeling of Dieless Tube Drawing of Strain Rate Sensitive Material with Coupled ThermoMechanical Analysis." *AIP Conference Proceedings*. Columbus: American Institute of Physics, 2004. 522-527.

[19] Gliga, M, and T Canta. "Theory and application of dieless drawing." *Wire industry*, 1999: 294-297.

[20] Goto, D M, J F Bingert, S R Chen, G T Gary, and R K Garrett. "The mechanical threshold stress constitutive-strength model description of HY-100 steel." *Metallurgical and Materials Transactions A* 31, no. 8 (2000): 1985-1996.

[21] Guo, Z X, and N Ridley. "Modelling of diffusion bonding of metals." *Material Science Technology* 3 (1987): 945-953.

[22] Hashmi, M S J, G R Symmons, and H Parvinmehr. "Anovel technique of wiredrawing." *Journal of Mechanical Engineering Science* 24, no. 1 (1982): 1-4.

[23] He, Yong, Xue-feng Liu, Jian-xin Xie, and Hong-gang Zhang. "Processing limit maps for the stable deformation of dileless drawing." *International Journal of Minerals, Metallurgy and Materials* 18, no. 3 (June 2011): 330-337.

[24] Huh, You, Bo Keun Ha, and Jong Sung Kim. "Dieless drawing steel wires using a dielectric heating method and modeling the." *Journal of Material Processing Technology* 210 (2010): 1702-1708.

[25] Kim, S H, Y N Paik, and Y Huh. "Modeling and characterizing the steady state dynamics of fast heated hot drawing process based on microwave heating method." *Journal of Korean Fiber Society* 43 (2006): 312-320.

[26] Kobatake, K, H Sekiguchi, K Osakada, and K Yoshikawa. "An analysis of temperature distribution in continuous dieless drawing." *Proceedings of international machin tool design and research conference.* London, 1977. 253-258.

[27] Kodur, Venkatesh, Mahmud Dwaikat, and Rustin Fike. "High-Temperature Properties of Steel for Fire Resistance Modeling of Structures." *Journal of Materials in Civil Engineering* 22, no. 5 (May 2010): 423-434.

[28] Lederman, F L, M B Salamon, and L W Shacklette . "Experimental verification of scaling and test of the universality hypothesis from specific heat data." *Physical Rreview B* 9, no. 7 (1974): 2981-2988.

[29] Lewis, K B. "Wiredrawing, ten centuries old, made its real advance in last hundred years." *The Iron age* 130 (July 1932): 58.

[30] Li, Yonggang, Nathaniel R Quick, and Aravinda Kar. "Dieless laser drawing of fine metal wires." *Journal of Materials Processing Technology* 123 (2002): 451-458.

[31] Li, Yonggang, Nathaniel R Quick, and Aravinda Kar. "Thermomechnaical effects in laser micro-processing for dieless metal wiredrawing." *Journal of Laser Apllication* 14, no. 2 (May 2002): 91-99.

[32] Manjoine, M, and A Nadai. "High speed tension tests at elevated temperatures ." *Journal of Applied Mechanics*, 1942: A77-A85.

[33] Naughton, M D, and P Tiernan. "An experimental approach to continuous dieless wiredrawing (Variant A)using ELI Ti–6Al–4V Alloy." *Journal of Engineering Materials and Technology* 131 (April 2009): 0210051-9.

[34] —. "Mechanical behaviour and superplastic forming capabilities of extra-low interstitial grade Ti-6Al-4V wire alloy with numerical verification." *Proceedings of Institution of Mechanical Engineers.* SAGE, 2007. 165-175.

[35] Naughton, M D, and P Tiernan. "Requirements of a dieless wiredrawing system." *Journal of Materials Processing Technology* 191 (2007): 310-313.

[36] Pawelski, O, W Rasp, and W Wengenroth. "investigation into processing of bars with variable cross-sections by dieless drawing." *Proceedings of the 6th ICTP.* Dusseldorf: Advanced technology of plasticity, 1999. 1753-1762.

[37] Pawelski, Oskar, and Altons Kolling. "Calculation of the temperature distribution in dieless drawing." *Steel Research* 66, no. 2 (1995): 50-54.

[38] Persson, Lars, and P Enghag. "Basic principles of wiredrawing." *Wire Industry* 63, no. 754 (October 1996): 727-733.

[39] Sekiguchi, H, and K Kabotake. "Development of dieless wiredrawing." *Proceeding of the second international conference on technology of plasticity.* Stuttgart: Springer-Verlag, 1987. 347-354.

[40] Sekiguchi, H, K Kabotake, and K Osakada. "A fundamental study on dieless drawing." *Proceedings of 15th M.T.D.R.* 1974. 539-544.

[41] Sherby, O D, and A Goldberg. "Comments on lozinsky and simeonova's paper on "superhigh plasticity of commercial iron under cyclic fluctuations of temperature"." *Acta Metallurgica* 9, no. 5 (1961): 510-512.

[42] Steinberg, D J, S G Cochran, and M W Guinan. "A constitutive model for metals applicable at high-strain rate." *Journal of Applied Physics* 51, no. 3 (1980): 1498-1504.

[43] Tiernan, P, and P Comerford. "Determining the suitability of low carbon." *Proceedings of the Institution of Mechanical Engineers.* Ireland, 2006. 267-275.

[44] Tiernan, P, R Carolan, E Twohig, and S.A.M. Tofail. "Design and development of a novel load-control dieless rod drawing system." *Journal of Manufacturing Science and Technology* 4 (2011): 110-117.

[45] Tiernan, Peter, and Michael T Hillery. "An analysis of wire manufacture using the dieless drawing method." *Journal of Manufacturing Processes* 10 (2008): 12-20.

[46] Tiernan, Peter, and Michael T Hillery. "Dieless Wiredrawing- an experimental and numerical analysis." *Journal of Materials Processing Technology*, 2004: 1178-1183.

[47] Tiernan, Peter, and Micheal T Hillery. "Experimental and numerical analysis of the deformation in mild steel wire during dieless drawing." *Journal of Materials Design and Applications*, 2002: 167-178.

[48] Twohig, E, P Tiernan, and S.A.M. Tofail. "Experimental study on dieless drawing of Nickel–Titanium alloy." *Journal of the Mechanical Behaviour of Biomecical Materials* 8 (2012): 8-20.

[49] Underwood, Ervin E. "A review of superplasticity and related phenomena ." *Journal of metals*, December 1962: 914-919.

[50] Varshni, Y P. "Temperature dependence of the elastic constant." *Physical Review B* 2, no. 10 (1970): 3952-3958.

[51]   Wang, Z T, G F Luan, G R Bai, K Kobatake, and H Sekiguchi. "A mathematical model study on the die-less drawing of variable-section tubular parts." *Journal of material processing technology* 59 (1996): 391-393.

[52]   Weiss, Volker, and Richard A Kot. "Dieless wiredrawing with transformation plasticity." *Wire Journal* 9 (1969): 182-189.

[53]   Weiss, Volker, and Richard A Kot. "Survey of deformation processes and deformation characteristics of difficult to form metals." Technical , Battelle Memorial Institute, 1967.

[54]   Wengenroth, Walter, Oskar Pawelski, and Wolfgang Rasp. "Theoretical and experimental investigations into dieless drawing." *Steel Research* 72, no. 10 (2001): 402-405.

[55]   Wright, Roger N, and Evan A Wright. "Basic analysis of dieless drawing." *Wire journal international*, 2000: 13-143.

[56]   Zener, C, and J H Hollomon. "Effect of strain rate upon plastic flow of steel." *Journal of applied physics*, October 1943: 22-32.

APPENDICES

Appendix A: Conventional Wiredrawing Calculations

Referring to Figure A.1, a slice method was proposed to analyze the wiredrawing process.
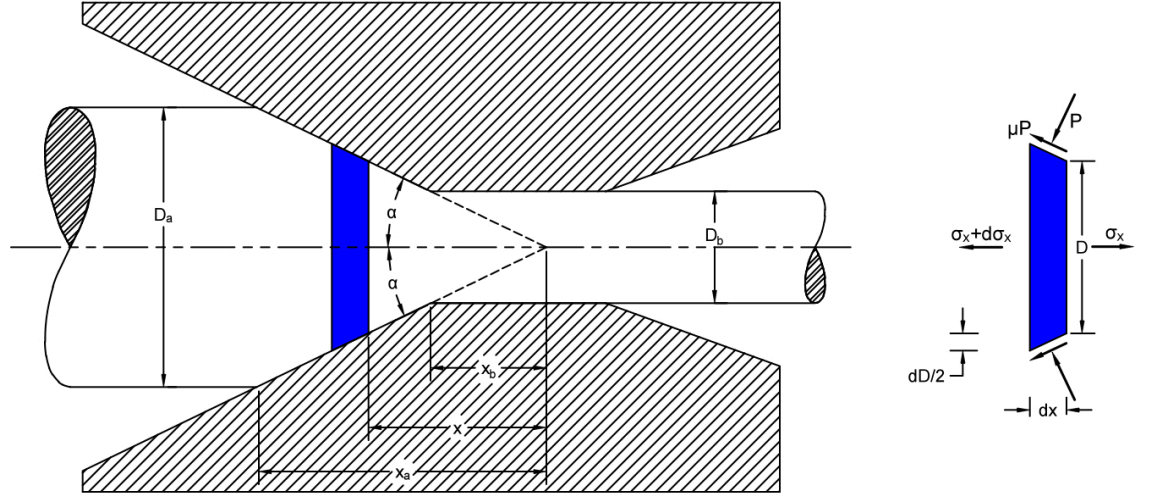
Figure A.1: The schematic model used in the slice method

By considering the equilibrium of a small element in the working zone there are three force components acting in axial direction, namely:

1. $(\sigma_x + d\sigma_x)\dfrac{\pi}{4}(D + dD)^2 - \sigma_x \dfrac{\pi}{4}D^2$ Due to the change in longitudinal stress.

2. $P(\pi D \dfrac{dx}{Cos\alpha})Sin\alpha$ Due to the die pressure on the circumference.

3. $\mu P(\pi D \dfrac{dx}{Cos\alpha})Cos\alpha$ Due to frictional drag at the circumference.

which must be in equilibrium under steady state drawing condition, i.e. $\sum F_x = 0$.

By equating the axial forces and after some manipulation and re-arranging we obtain:

$$D\,d\sigma_x + 2[\sigma_x + P(1 + \mu \cot\alpha)]dD = 0 \qquad\qquad (A.1)$$

This is the closest condition to principal stress state, and using the Tresca criterion the following relations can be assumed:

$$\sigma_r \approx -P$$
$$\sigma_{max} - \sigma_{min} = Y$$
$$\sigma_x - (-P) = Y$$
$$P = Y - \sigma_x$$

(A.2)

Substituting these back into the Equation A.1, and after a little manipulation we arrive at:

$$\frac{\sigma_x}{Y} = \frac{1+B}{B}[1 - (\frac{D}{D_a})^{2B}]$$

(A.3)

Where $B = \mu \cot \alpha$. This equation gives us the value of axial stress at any cross section D. Evaluating the above equation at the exit diameter, D_b, results in the pulling stress needed to draw the wire through the die.

$$\frac{\sigma_{xb}}{Y} = \frac{1+B}{B}[1 - (\frac{D_b}{D_a})^{2B}]$$

(A.4)

Considering an ideal case with no friction by setting $\mu = 0.0$ in our analysis and re-working it we obtain:

$$\frac{\sigma_{xb}}{Y} = 2\ln D_a - 2\ln D_b = \ln\left(\frac{D_a}{D_b}\right)^2$$

(A.5)

By substituting Y for σ_{xb} in the above equation, we find the maximum reduction limit for a frictionless wiredrawing, which is 63%.

Appendix B: Strain-rate Sensitivity Index

Strain-rate sensitivity index is a measure of a material ability to deform in a superplastic manner. A value of 0 indicates that the material exhibits negligible levels of super-plasticity while a value of 1 indicates that the material is fully superplastic. Backofen et al. [1] have obtained a quantitative index of strain-rate sensitivity by evaluating strain-rate sensitivity index m under an assumed stress vs. strain-rate relationship of the form $\sigma = K\dot{\varepsilon}^m$. In effect, the slope of a $\log \sigma$ vs. $\log \dot{\varepsilon}$ was determined for various conditions of strain ε, strain-rate $\dot{\varepsilon}$ and temperature T. The procedure involved making sudden changes in pulling speed and transient hardening was eliminated from load comparisons by straining an additional 2 to 3% at the second speed.
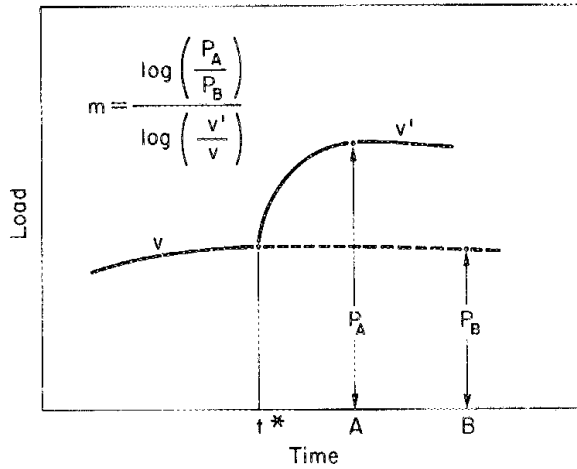
Figure A.2: Schematic of load vs. time diagram representing a velocity change from v to v' at time t^* (Source: Superplacticity in an Al-Zn alloy by Backofen[1])

Times A and B represent the same strain-rate at different pulling speeds. By assuming only slow variation of m with strain rate over the experimental range, an m value could then be calculated from:

$$m = \frac{\log(P_A/P_B)}{\log(v'/v)} \qquad \text{(B.1)}$$

The contribution of high strain rate sensitivity to stable flow can also be demonstrated by a more analytical argument. Restating the stress-strain relation as:

$$\sigma = K\dot{\varepsilon}^m = \frac{F}{A} \tag{B.2}$$

where F if the force being transmitted through a cross-sectional area A, and K is a constant. The strain-rate at any point in the rod of incompressible material is:

$$\dot{\varepsilon} = \frac{1}{l}\frac{dl}{dt} = -\frac{1}{A}\frac{dA}{dt} \tag{B.3}$$

by combining this equation with Equation B.2 we obtain:

$$-\frac{dA}{dt} = \left[\frac{F}{K}\right]^{1/m}\left(\frac{1}{A^{\frac{1-m}{m}}}\right) \tag{B.4}$$

Therefore, as long as m is less than 1, the smaller the cross section the more rapidly it is reduced. As m approaches 1, the reduction rates at all cross sections approaches a common level. When m =1 the flow is Newtonian viscous and dA/dt independent of A so that any cross-sectional irregularities (or incipient neck) are simply preserved upon pulling.

Appendix C: The parameter configurations tables

Table 4: Parameter configurations used in the simulation of %RA vs. Velocity

Trial #	Matlab Solver	FD Order	Time step size, dt (sec)	Total time t (sec)	Number of the nodes	Deformation length L (mm)	Initial velocity, V1 (mm/sec)	Initial CSA (mm^2)	L/(node-1) = dx (mm)
1	ODE15s	1st Order	1.00E-05	1	200	100	20	1.5	0.50
2	ODE15s	2nd order	1.00E-05	1	200	100	20	1.5	0.50
3	ODE15s	1st Order	1.00E-05	1	400	200	20	4	0.50
4	ODE15s	2nd order	1.00E-05	1	400	200	20	4	0.50
5	ODE15s	1st Order	1.00E-05	1	400	200	20	4	0.50
6	ODE15s	2nd order	1.00E-05	1	400	200	20	4	0.50
7	ODE15s	1st Order	1.00E-05	0.5	600	100	40	4	0.17
8	ODE15s	1st Order	1.00E-05	1	600	100	40	4	0.17
9	ODE15s	1st Order	1.00E-05	0.5	400	100	20	4	0.25
10	ODE15s	1st Order	1.00E-05	0.5	400	100	40	4	0.25
11	ODE15s	1st Order	1.00E-05	1	400	100	40	4	0.25
12	ODE15s	1st Order	1.00E-05	0.5	200	100	20	1.5	0.50
13	ODE15s	1st Order	1.00E-05	1	400	200	40	4	0.50

Table 5: Parameter configuration used in the simulation of %RA vs. Deformation length

Trial #	Matlab Solver	Time step size, dt(s)	FD Order	Total time t (s)	Number of the nodes	ΔV (mm/sec)_	Drawing Velocity V (mm/s)	Initial Velocity V1 (mm/sec)
1	ODE15s	1.00E-05	1st order	0.5	400	75	115	40
2	ODE15s	1.00E-05	1st order	0.5	400	80	100	20
3	ODE15s	1.00E-05	1st order	0.5	400	130	150	20
4	ODE15s	1.00E-05	1st order	0.5	400	135	175	40
5	ODE15s	1.00E-05	1st order	0.5	400	155	175	20
6	ODE15s	1.00E-05	1st order	0.5	400	220	240	20
7	ODE15s	1.00E-05	1st order	0.5	400	240	280	40
8	ODE15s	1.00E-05	1st order	0.5	600	110	150	40
9	ODE15s	1.00E-05	1st order	0.5	600	120	160	40
10	ODE15s	1.00E-05	1st order	0.5	600	140	180	40
11	ODE15s	1.00E-05	1st order	0.5	600	150	190	40
12	ODE15s	1.00E-05	1st order	1	200	65	85	20
13	ODE15s	1.00E-05	1st order	1	200	80	100	20
14	ODE15s	1.00E-05	1st order	1	200	130	150	20
15	ODE15s	1.00E-05	1st order	1	400	80	120	40
22	ODE15s	1.00E-05	1st order	1	400	80	100	20
16	ODE15s	1.00E-05	1st order	1	400	135	175	40
17	ODE15s	1.00E-05	1st order	1	400	240	280	40
18	ODE15s	1.00E-05	1st order	1	600	110	150	40
19	ODE15s	1.00E-05	1st order	1	600	120	160	40
20	ODE15s	1.00E-05	1st order	1	600	140	180	40
21	ODE15s	1.00E-05	1st order	1	600	150	190	40

Trial #	Matlab Solver	Time step size, dt(s)	FD Order	Total time t (s)	Number of the nodes	ΔV (mm/sec)_	Drawing Velocity V (mm/s)	Initial Velocity V1 (mm/sec)
23	ODE15s	1.00E-05	2nd order	0.5	200	70	90	20
24	ODE15s	1.00E-05	2nd order	0.5	200	100	120	20
25	ODE15s	1.00E-05	2nd order	0.5	200	155	175	20
26	ODE15s	1.00E-05	2nd order	1	200	65	85	20
27	ODE15s	1.00E-05	2nd order	1	200	70	90	20
28	ODE15s	1.00E-05	2nd order	1	200	85	105	20

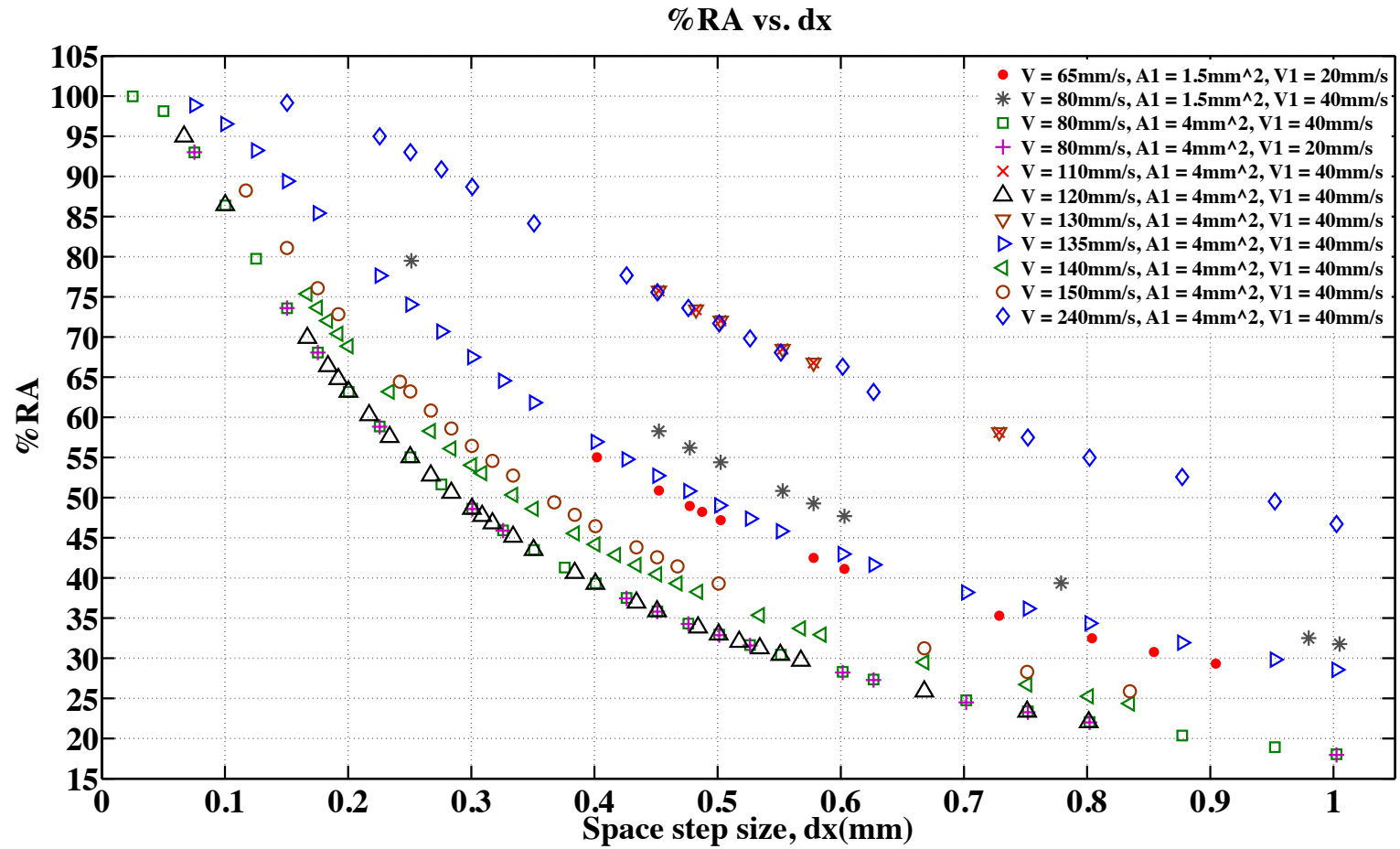## Appendix D: %RA versus space step size

Figure A.3: %RA vs. dx for various velocities and parameter configurations